Optimisation of an Impulse Radiating Antenna Through an Effective Trifilar Coupled–Line Balun

by

Stanley Okoth Kuja

Dissertation presented to the
Faculty of Engineering, Stellenbosch University
in partial fulfilment of the requirements for the degree
of Doctor of Philosophy in Engineering

Department of Electrical and Electronic Engineering,
Stellenbosch University

Supervisor: Dr. Pieter Gideon Wiid

December 2019

Declaration

I have read and understand the Stellenbosch University Policy on Plagiarism and the definitions of plagiarism and self-plagiarism contained in the Policy [Plagiarism: The use of the ideas or material of others without acknowledgement, or the re-use of ones own previously evaluated or published material without acknowledgement or indication thereof (self-plagiarism or textrecycling)].

I understand that direct translations are plagiarism, unless accompanied by an appropriate acknowledgement of the source. I also know that verbatim copy that has not been explicitly indicated as such, is plagiarism.

I know that plagiarism is a punishable offence and may be referred to the University's Central Disciplinary Committee (CDC) who has the authority to expel me for such an offence.

I know that plagiarism is harmful for the academic environment and that it has a negative impact on any profession.

Accordingly all quotations and contributions from any source whatsoever (including the internet) have been cited fully (acknowledged); further, all verbatim copies have been expressly indicated as such (e.g. through quotation marks) and the sources are cited fully.

I declare that, except where a source has been cited, the work contained in this dissertation is my own original work and that I have not previously (in its entirety or in part) submitted it for grading in this module or another module. No part of this research may be reproduced without prior knowledge of the author and Stellenbosch University.

December 2019

Signature
Kuja, S.O.

Date

Abstract

The Square Kilometre Array (SKA) telescope – a mega-science endeavour – is planned to be the largest and most sensitive radio astronomy facility when operational. And the South African SKA (SKA-SA) project is part of the SKA enterprise including its 64-dish precursor telescope; MeerKAT. Research has shown that proper management of radio frequency interference (RFI) is key to the success of astronomy science. Thus, there is need for a hyper-band (HB) antenna metrology system for constant monitoring of RFI at the SKA SA (Karoo) site whose electromagnetic environment changes with the ongoing infrastructure development and other unpredictable RFI sources. This research aims to optimise an impulse radiating antenna (IRA) as an HB directional antenna suitable for the intended RFI time-domain (TD) measurement at the Karoo site.

Based on the review of the original IRA designs including characterisation of the initial Stellenbosch IRA, the balanced feed system (balun) is the most critical part to be considered for optimisation. In this regard, a novel HB trifilar coupled-line balun is designed for the IRA. The prototype trifilar balun is implemented in CST using the Finite Integration Technique (FIT) solver and verified with measurement and AWR simulation data. Building on the corroborated prototype balun, further modelling and optimisation is done in CST leading to the final design of the coupled-line balun. A 200-ohm conical plate-fed dish IRA is then created in FEKO and unioned with the imported CST model of the optimised balun. The method of moments (MoM) code and Genetic Algorithm in FEKO are applied as the solver and optimiser, respectively. The optimised model of the IRA is validated using the measured S_{11}, gain and the far-field radiation pattern of the exact fabricated IRA.

Analysis of the simulation data indicate uniform aperture fields, reduced back lobes and lower side lobe levels (SLLs) of the optimised FEKO model compared to the original model of the IRA. The results show that the optimised IRA has low S_{11} ($<$ -10 dB) over a large-band-ratio (1.9911 fractional bandwidth), which qualifies it as an HB antenna. The HB low S_{11} response of the IRA is a characteristic of the trifilar balun due to the fact that it ensures proper balanced feed for the IRA over HB frequency range. Additional advantage of the balun is its use as a transmission line, hence obviating the need for high impedance radio frequency (RF) coaxial cables which are associated with common-mode (CM) currents influencing balance in cable-fed IRAs. This further prevents the use of RF chokes usually required to minimise the CM currents. The optimised IRA can be integrated with the SKA real-time analyser for on-site RFI and propagation measurement in real time.

Opsomming

Die Vierkante Kilometer Reeks (SKA) teleskoop, 'n mega-wetenskaplike strewe, word beplan om die grootste en sensitiefste radio-astronomiefasiliteit te wees wanneer dit operasioneel is. Die Suid-Afrikaanse SKA (SKA-SA) -projek maak deel uit van die SKA-onderneming, insluitend die 64-skottel voorloperteleskoop; MeerKAT. Navorsing het getoon dat behoorlike bestuur van radiofrekwensie-steurings (RFS) die sleutel tot die sukses van die sterrekunde-wetenskap is. Daar is dus 'n behoefte aan 'n hiperband (HB) antenna-metrologie-stelsel vir die konstante monitering van RFS op die SKA SA (Karoo) terrein, waar die elektromagnetiese omgewing voortdurend verander met die voortgesette infrastruktuurontwikkeling en ander onvoorspelbare RFS bronne. Hierdie navorsing het ten doel om 'n impulsstralende antenna (ISA) te optimiseer as 'n HB-gerigte-antenna wat geskik is vir die beoogde RFS-tyddomein (TD) -metings op die Karoo-terrein.

Gebaseer op die ondersoek van die oorspronklike ISA ontwerpe, insluitende karakterisering van die aanvanklike ISA prototipe, is die gebalanseerde voersisteem (balon) geïdentifiseer as die kritiekste deel wat oorweeg moet word vir optimisering. In hierdie verband is 'n nuwe HB-drielyn-gekoppelde balon ontwerp vir die ISA. Die prototipe drielyn balon word geïmplementeer in CST met behulp van die "Finite Integration Technique (FIT) solver" en geverifieer met meting en AWR simulasiedata. Verdere modellering en optimisering word gedoen in CST wat bou op die bevestigde prototipe balon en lei tot die finale ontwerp van die gekoppelde balon. 'n 200-ohm kegelvormige-plaatvoed skottel-ISA word dan in FEKO geskep en met die ingevoerde CST-model van die geoptimiseerde balon verbind. Die metode van momente (MoM) kode en Genetiese Algoritme in FEKO word onderskeidelik as "solver" en optimiseerder aangewend. Die geoptimiseerde model van die ISA word gevalideer deur gebruik te maak van die gemete S_{11} en ver-veldstralingspatroon van die presiese vervaardigde ISA.

Analise van die simulasiedata dui op uniforme openingvelde, verminderde trulobbe en laer sylobvlakke (SLVe) van die geoptimiseerde FEKO model in vergelyking met die oorspronklike model van die ISA. Die resultate toon dat die geoptimiseerde ISA lae S_{11} ($<$ -10 dB) het oor 'n wyebandverhouding (1.9911 breuk-bandwydte), wat dit as 'n HB-antenna kwalifiseer. Die HB lae S_{11} reaksie van die ISA is 'n kenmerk van die drielyn-balon as gevolg van die feit dat dit 'n goeie gebalanseerde voer vir die ISA oor die HB-frekwensie bereik verseker. 'n Bykomende voordeel van die balon is die gebruik daarvan as 'n transmissielyn, wat die noodsaaklikheid van hoë-impedansie-radiofrekwensie (RF) koaksiale kabels, wat verband hou met gemene-modus (GM) strome wat die balans in kabelvoedende ISA's beïnvloed, vermy. Dit verhoed verder die vereiste van RF-dempers wat gewoonlik benodig word om die GM-strome te verminder. Die geoptimiseerde ISA kan geïntegreer word met die SKA intydse-analiseerder vir intydse op-terrein RFS en voortplantingsmetings.

Acknowledgements

I am indebted to my supervisor, Dr. Gideon Wiid, for the patience and diligence he has undertaken to peruse my drafts. Thank you for your invaluable and constructive suggestions and comments during the forethought and formulation of this research project. Your readiness to offer your time so generously and your words of wisdom and inspirational quotes from the 'PhD comic book' as well as your moral support has been very much appreciated.

I would like to acknowledge the assistance provided by Anneke Bester during measurement and Wessel Croukamp for the fabrication of the antenna. To my former and present colleagues in room E212, I am thankful for your excellent collaboration. My deepest gratitude to the South African Radio Astronomy Observatory (SARAO), through the National Research Foundation (NRF), for the funding of my PhD research. Also, to Prof. Howard Reader and Prof. David Davidson for all the support they have given me throughout my study.

Above all, I am very grateful to my wife, Iris Keya, for being sympathetic and understanding and providing the moral and emotional support that I needed so often. I owe you so much, my love.

A very special thank you to Easter, Mathews, TJ, Allan, Eng. Amollo, Magerenge, Ang'anyo and Joely for their friendship and the positive role they have played in my life. Finally, I appreciate the love and support from my family members and friends in general.

Dedication

A dedication page of a dissertation is titled "Dedication" because the author has to dedicate himself or herself to get the work completed. Research – writing – is a very lonely process that usually compels professional researchers to isolate themselves from social life. If you are married then your spouse must be very understanding and nurturing in order to have a peaceful environment where creativity and imagination can thrive. It is for this reason that I dedicate this dissertation to the love of my life, Iris Keya.

And to my daughter, Marabel, you started crawling a few months ago and now you have begun walking and running. I did not realize how fast you grow, probably because I am far away from you. Nonetheless, my heart is full of joy knowing that each day you are growing older and lovely, and this has given me the strength to compile my chapters. I would have loved to read a few sections with you and to ask what you think, but you are not old enough to do this with me! Maybe someday when you are old enough, you shall bump into this manuscript and be tempted to read, and I shall still want to know your opinion of it.

Last but not least, to my late mother, Mary, whom for her hard work and passion in education, the dream has been fulfilled!

Contents

List of Figures

List of Tables

Nomenclature

Symbols and Units

μ_0	Permeability of free space	$\mathrm{H.m^{-1}}$
ϵ_0	Permittivity of free space	$\mathrm{F.m^{-1}}$
ϵ_r	Relative permittivity	
η	Antenna efficiency	%
η_0	Impedance of free space	Ω
λ	Wavelength	m
ω	Angular frequency	$\mathrm{rad.s^{-1}}$
π	Pi	
σ	Conductivity	$\mathrm{S.m^{-1}}$
c	Speed of light	$\mathrm{m.s^{-1}}$
f	Frequency	Hz
G_{dBi}	Antenna gain relative to an isotropic antenna	dBi
t	Time	s

Abbreviations

BW	Beam-Width
CEM	Computational Electromagnetics
CHPC	Centre for High Performance Computing
COTS	Commercial-Off-The-Shelf
EM	Electromagnetic

EMC	Electromagnetic Compatibility
EMF	Electromotive Force
EMI	Electromagnetic Interference
EMP	Electromagnetic Pulse
FCC	Federal Communications Commission
FD	Frequency Domain
FDTD	Finite Difference Time Domain
FEC	Far-End Coupling
FEM	Finite Element Method
FIT	Finite Integration Technique
GA	Genetic Algorithm
GPR	Ground Penetrating Radar
HB	Hyper-band
HIRA	Half-Impulse Radiating Antenna
HPC	High Performance Computing
HPEM	High-Power Electromagnetic
IEMI	Intentional Electromagnetic Interference
IRA	Impulse Radiating Antenna
ITR	Impedance-Transfer-Ratio
MoM	Method of Moments
NEMP	Nuclear Electromagnetic Pulse
NEXT	Near-End Crosstalk
PCB	Printed Circuit Board
PEC	Perfect Electric Conductor
RAM	Random Access Memory
RATTY	ReAl-Time Transient Analyser
RFI	Radio Frequency Interference
RTA	Real-Time Analyser
SLL	Side Lobe Level
SMA	Sub-Miniature version A
SOLT	Short-Open-Load-Thru
SWR	Standing Wave Ratio
TD	Time Domain
TEM	Transverse Electromagnetic
UWB	Ultra-wideband
VNA	Vector Network Analyser

CHAPTER 1

Introduction

Scientific advancements in radio astronomy have led to the development of new generation radio telescopes such as the MeerKAT [1] and the planned Square Kilometre Array (SKA) telescope [2]. Due to the sensitive nature of the SKA project, the choice of a radio quiet site is an essential factor to be considered [3]. As a result, the South African Radio Astronomy Observatory (SARAO) has declared the telescope site (Karoo) radio quiet and much has been done to preserve its electromagnetic (EM) quietness so far. SARAO coordinates all the radio astronomy facilities in South Africa including its contribution to the infrastructure and engineering planning for the SKA project. Initial investigations using theoretical propagation tools and digital terrain models show the shielding effect provided by the terrain on radio frequency interference (RFI) [4].

However, the ongoing infrastructure development gradually changes the EM environment and there are potential external sources of RFI especially the ones that SARAO does not have control over such as wind turbines from the neighbouring farms. Therefore, it is important to continuously characterize the EM environment surrounding the sensitive equipment and to be aware when changes occur, to make electromagnetic compatibility (EMC) predictions easier [5]. The need for constant monitoring of RFI is mandatory in order to realize the transformational science envisioned for the project. This requires an effective time domain (TD) metrology system suitable for measuring a broader spectrum of RFI within a shorter period of time. The research focusses on the characterization

and optimisation of a unique antenna – impulse radiating antenna (IRA) – which has the characteristics required for the TD system.

1.1 Motivation and Objective

The SKA telescope is an ambitious project which has been initiated to conduct deep space scientific observations and to break new grounds in astronomy science. RFI can be a great threat to the SKA telescope to maximise on the science for which it is being assembled. And the key problem is that RFI cannot be completely eliminated because of its unpredictable nature. However, constant monitoring of RFI provides proper understanding of the site's EM environment for better management of electromagnetic interference (EMI) and propagation issues. Therefore, the need for an effective TD antenna system for RFI measurement and evaluation cannot be overemphasized.

Among the elementary components of the so-called "TD system" is the antenna unit whose impact plays a major role in the implementation and success of the system. Since this is a hyper-band (HB) system the antenna must be non-dispersive and radiating over a broader bandwidth in order to cover the short EM pulse spectrum generated. A suitable antenna that can transmit and receive short pulses is the IRA. A fast pulser together with the IRA can be used to generate a focused EM pulse in free space. Propagation loss and shielding effectiveness, both imperative for RFI qualification and mitigation, can be tested in different test set-ups using the IRA and a transient analyser system like the SKA real time analyser (RTA).

A TD system provides the benefit of radiating and measuring a wide range of frequencies with a single TD pulse. On the other hand, a frequency domain (FD) system requires more time for measurement of such a broader frequency spectrum. Unfortunately, time is not always available during on-site measurement due to the fact that various activities including science observations have to be halted during measurement. It is worth noting that FD technique is important and offers significant contribution to the field of metrology but its TD equivalent can improve on its limitation. A brief overview of the IRA is provided in the following section.

1.2 The Impulse Radiating Antenna (IRA)

IRAs are considered as a special class of aperture antennas which radiate and receive transient pulses. Essentially, the characteristic of the IRA is that, during an excitation of

the antenna with a fast-rising, slowly-decaying source, an impulse-like far field is generated [6]. The bandwidth covered by this type of antenna is very large and can be in the HB category [7]. The required combination for the step-rising plane wave on the aperture of IRA is the transverse electromagnetic (TEM)-fed reflector.

From a historical perspective, the technology that led to the development of the IRA can be traced from the nuclear EM-pulse (EMP) studies, particularly the studies which linked to the pulser systems known as EMP simulators used to test electronic systems [8, 9]. The IRA has found various applications, for example, in transient radar, high-power pulse radiators and in areas which require antennas with the capability to operate on many frequencies simultaneously due to the large bandwidth [10]. In this research, however, due to the HB characteristic of the IRA, it is optimised for low-power EMC studies related to the SARAO-SKA project.

Figure 1.1 is an example of a conically-symmetric TEM-fed reflector IRA following a typical Farr IRA design [11]. It shows different components of the IRA structure which include: the reflector, launcher plates (feed arms), balanced feed system (splitter-balun) and the resistive termination loads which are described in detail in chapter 2, section 2.5. The outer feed cables in Figure 1.1 are usually high impedance RF cables used to match the input impedance of the IRA. However, the cable configuration is associated with common-mode (CM) currents, hence the application of ferrite beads (or RF chokes)

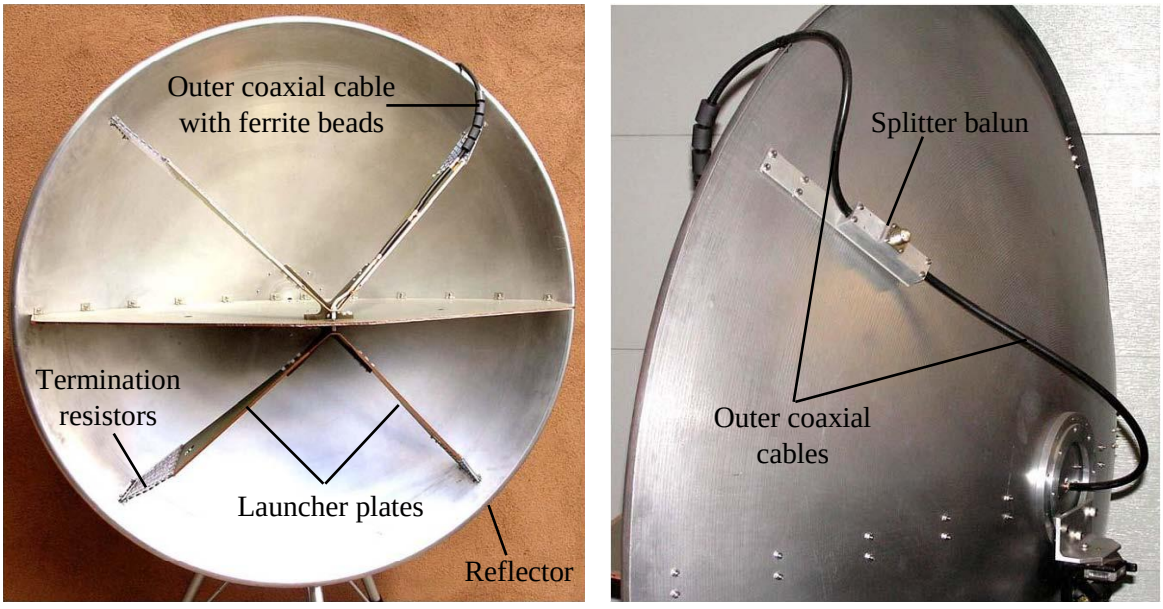

(a) **(b)**

Figure 1.1: (a) A photo showing the front view of the IRA-6 (b) A rear view of the IRA-6 with splitter-balun mounted on the dish [11].

to minimise the imbalance caused by the CM currents. In general, it is no trivial task to match an HB antenna (the IRA) over the large-band-ratio [12]. This forms the main contribution of this dissertation as highlighted in section 1.4.

1.3 Methodology

Starting with the "general to specific or known to unknown" kind of approach, we dig into the existing literature that is inundated with design examples of the IRA, especially the feeding structure. Useful information is extracted regarding the design parameters and operation of the IRAs. In [13] we find the details of the original IRA design that is constructed at Stellenbosch University, Engineering Department, for RFI measurement. Since less reflections are preferred for the on-site TD related measurement, the Stellenbosch IRA is characterised in an anechoic chamber as well as in the method of moments (MoM) code FEKO so as to identify areas that can be optimised for improved performance.

The common problem faced by antenna designers or engineers is how to properly feed an antenna (IRAs included). The use of the splitter balun does not obviate the CM currents which can cause severe unbalance for the IRA. The focus of this research is on a novel design of an HB trifilar coupled-line balun for the IRA. We rely significantly on various simulation tools to achieve the performance goals of the trifilar balun. In fact, modern technological innovations are driven by simulation work which saves time and resources with regards to creating prototype models and rigorous testing before the fabrication process. First, a model of the initial prototype of the trifilar balun is created in CST and the Finite Integration Technique (FIT) is utilised as the solver. The prototype balun is fabricated and measured data compared to simulation results. In addition, microwave office (AWR) is used to further validate the initial CST model. CST is utilised for detailed modelling and optimisation of the final trifilar balun. An exact optimised design of the CST model of the trifilar balun is fabricated on a printed circuit board (PCB) material. The required Gerber files for the fabrication machine are generated using an Altium designer tool.

A new design of the computational electromagnetic (CEM) model of the IRA is created in FEKO and for a full wave analysis, MoM is implemented in all the FEKO simulation set-ups. The optimised CST model of the trifilar balun is imported in FEKO and unioned together with the final design of the CEM model of the IRA before optimisation using Genetic Algorithm technique. Finally, the optimised IRA is fabricated and characterised in the anechoic chamber and the comparison between measurement and simulation results is done to validate the optimised IRA.

1.4 Research Contribution

Accurate detection, characterization and mitigation of RFI signals depend on the antenna system used for identification of the unwanted signals. The IRA antenna is a suitable choice because of its non-dispersive characteristic and the large-band-ratio it offers at short temporal response. The dissertation work centres on the optimisation of the IRA and the following are outlined as the main contributions of this research.

- *Designing an HB balanced feed system – (balun)*
  Designing a balun can be as complicated as designing an antenna itself, particularly for an HB antenna. A novel and HB trifilar coupled-line balun is designed for the IRA. The trifilar balun is easy to fabricate and generates balanced output signals to excite the negative and positive plates of the IRA equally. Also, the balun has a non-uniformly coupled asymmetric configuration which has the benefit of minimising the effect of the pre-pulse which would have otherwise caused imbalance for the IRA.

- *Elimination of the outer RF feed coaxial cables*
  The use of expensive RF coaxial cables as part of the feeding structure for the IRA is characterised with CM currents which can affect the aperture field of the IRA. These are high impedance cables required to match the impedance of the IRA. However, the commonly known commercially available cables are the 50, 70, 75 and 93 ohm impedances [14]. For higher impedance cables (unavailable in the market), it will be costly to manufacture custom designed cables. In an effort to reduce the effects of the CM currents, ferrite beads (chokes) are attached to the cables as shown in Figure 1.1 (a) [11]. The new cable topology implemented with the trifilar balun eliminates the need for such high impedance cables. Only a 50 ohm coaxial cable is used to connect the IRA to an excitation source, e.g., a signal generator.

- *Optimisation of the aperture field of the IRA*
  One outstanding problem is to optimise the aperture field of the IRA to achieve a symmetrical aperture. To the author's knowledge, there are some attempts to calculate the aperture field but no optimization has been attempted to date. The launcher plates form the TEM feeding structure of the IRA, and thus thicker plates can obstruct the aperture. Thinner plates are designed for the IRA (to reduce aperture blockage) and are optimised using a Genetic Algorithm code in FEKO. This together with the implementation of the optimised trifilar balun results in a uniform aperture field of the IRA.

- *Manufacturing an HB Optimised IRA*
  The objective of this research is to construct a ready-to-use HB optimised IRA

for various propagation and shielding effectiveness studies at the Karoo. The requirement for radio quietness extends to the IRA and other measuring equipment which can introduce artefacts, e.g., reflections from the back-lobes that can corrupt the measurement data. However, the original IRA [13] had very large back-lobe, asymmetric aperture and poor reflection coefficient, S_{11}, over the frequency band. Whereas the optimised IRA has reduced back-lobe, symmetric aperture and better S_{11} response across the HB frequency range.

- *Low loss coupled-line balun*
  For even distribution of currents in the antenna structure over the HB frequency, the trifilar balun must effectively provide balanced currents over the large bandwidth. But the higher frequency components can largely influence the dielectric loss properties of a material. In this regard, the new Rogers 4003C (refer to appendix B) material is used because of its better frequency properties (low loss at high frequencies). In addition, the normal losses of the EM energy within the material is compensated by increasing the length of the balun (as a transmission line) for increased coupling.

1.5 Dissertation Layout

The basics of electrodynamics and the IRA antenna are presented in chapter 2 where we discuss the generation and detection of EM waves, the interaction of EM waves through superposition principle, the ultra-wideband technology and its relevance in antenna engineering, an analogy for the antenna, the background of IRA and its component parts, the two domains (TD and FD) used in the results analysis throughout dissertation and the potential effect of the terrain on the IRA radiation during on-site measurement.

Chapter 3 describes various designs of the IRA with regards to the IRA's feeding structure, polarization geometries and cable feed topologies. The original IRA design at our engineering department is presented in this chapter and it is characterised using measurement and simulation to identify areas of optimisation. We conclude chapter 3 by highlighting the requirements for the new HB trifilar balun for the IRA. A brief review on baluns is introduced in the first section of chapter 4. Thereafter the concept of coupled transmission lines is explained and how we utilise it in the design of the trifilar coupled-line balun. We describe the design and verification of the initial prototype of the trifilar balun, further modelling and optimisation of the balun and fabrication of the optimised trifilar balun for the IRA.

The optimisation of the final IRA design through computational modelling is detailed in

chapter 5. The implementation of the optimised trifilar balun and the final IRA model is achieved in FEKO as well as the design of the new feeding structure. The optimised IRA model is compared to the original IRA. The fabrication and characterization of the final optimised IRA is also presented in this chapter. Finally, chapter 6 of this dissertation concludes with an assessment of the contributions of this work to IRA and recommendations for further research of this work. Other information regarding the optimisation methods, graphs and specification sheet are included in the appendices.

—To raise new questions, new possibilities, to regard old problems from a new angle, requires creative imagination and marks real advance in science —

—Albert Einstein —

CHAPTER 2

Fundamentals of Electrodynamics and Reflector Antennas

Electromagnetic (EM) waves are all around us from different sources such as celestial bodies, radio stations, computers, mobile phones among others; but how and why do we want to control them? In electric power transmission lines engineers use metals in order to transfer these waves while in optical communication light is placed inside a dielectric material to guide it from one end to another. The use of EM waves has generally improved the quality of life and human interaction. On the other hand, their existence can create a complex EM environment and sometimes detrimental to mankind.

However, with different materials and technological advancements in engineering, there are exciting possibilities to control these waves for various applications. For instance, in radio astronomy, scientists who seek to give insight into the existence of the universe and to predict its destiny must have access to astronomical signals. Antenna technology has made it possible for the current and future advanced astronomy science and radio frequency interference (RFI) monitoring and mitigation.

The basics of EM waves, how they are generated, propagate in space and detected is important in antenna engineering where this research is relevant. Therefore, this chapter reviews the theoretical framework of EM waves where Maxwell's and Jefimenko's equations are briefly discussed, the ultra-wideband (UWB) technology and applications, antenna properties with specific interest on impulse radiating antenna (IRA), frequency and time

domain concepts and finally effects of the earth on the IRA radiation.

2.1 The Theory of Electromagnetism

In the early days until 1820, electricity and magnetism were considered as completely separate topics. In that year Oersted realized that a magnetic compass needle could be deflected by an electric current [15]. Thereafter, it did not take long before a new postulate was correctly formulated by Ampere that electric charges in motion cause all magnetic phenomena. Faraday then followed with another discovery in 1831 that a magnet in motion leads to electric current [15]. As Maxwell and Lorentz perfected this theory, electricity and magnetism were inextricably linked and became a single topic of interest: *electromagnetism*.

In the theory of electromagnetism the basic problem to be solved is what happens to electric charges when they interact with each other, say, in a bunch of charges. A field theory through the classical approach explains that the EM fields permeate the surrounding of an electric charge [15]. A neighbouring charge that is within the fields will experience a force; thus, the fields are responsible for the interaction of these charges. When a charge accelerates, part of the field split off and travel at the speed of light, possessing some energy, momentum, and angular momentum [15]. This is known as *EM radiation* which in antenna theory is either transmitted into or received from space. The study of field theory is as important as the study of electric charges because charges generate and detect EM fields. When an antenna is operational, certain physical processes occur within the antenna and the space around it which can be described by Maxwell's and Faraday's theories. The physical phenomena of EM wave propagation through a transmission line of an antenna can be explained by the wave model while Faraday's thesis governs the EM radiation into the immediate environment of the antenna.

2.1.1 Maxwell's Equations

Maxwell's equations refer to the quartet of equations which Maxwell used to unify the theories of optics and classical wave in 1864 [16]. They are the backbone of modern EM modelling which has allowed accurate design and analysis of formally intractable intricate antenna system configurations [16, 8]. Today, a good case in point is the equivalence principle (theorem) that is widely used in the field of antennas and computational electromagnetics (CEM) for various formulations. The physical radiating element is replaced by

equivalent sources which are external to a closed surface enclosing the physical element, and generate the exact fields as those of the physical radiating element (antenna) [17].

It is possible to mathematically manipulate Maxwell's general differential equations (2.1)–(2.4) to obtain their equivalent integral form for the computation of the actual current or field distribution [16]. For point sources, *Green's function* is utilised to simplify the calculations. In modern CEM the Method of Moments (MoM) is applied to solve these integral equations [18]. However, for electrically large materials the capabilities of MoM is limited by large computer memory and long simulation time required.

$$\nabla.\vec{E} = \frac{1}{\epsilon_0}\rho \tag{2.1}$$

$$\nabla \times \vec{E} = -\frac{\partial \vec{B}}{\partial t} \tag{2.2}$$

$$\nabla.\vec{B} = 0 \tag{2.3}$$

$$\nabla \times \vec{B} = \mu_0 \vec{J} + \mu_0 \epsilon_0 \frac{\partial \vec{E}}{\partial t} \tag{2.4}$$

where $\vec{E}$ is the electric field vector, $\vec{B}$ is the magnetic flux vector, ρ is the volume charge density, $\vec{J}$ is the surface density of electric current, μ_0 and ϵ_0 are the permeability and permittivity of free space, respectively.

It should be noted that CEM techniques can as well be applied directly on the differential equations above to obtain the solution for $\vec{E}$ and $\vec{B}$. Contrary to the integral equations that use unknown surface currents, the differential equations use the volume of unknown EM fields [16]. This particular approach results into finite difference and finite element solution schemes. The former scheme gives approximation of partial derivatives in both time and space, giving rise to Finite Difference Time Domain (FDTD) technique.

The implementation of FDTD in time implies that a wider frequency spectrum can be covered within a single simulation run when a broadband time-pulse is chosen [16]. The other scheme is the Finite Element Method (FEM) where the volumetric continuous domain is replaced with sub-domains known as finite elements. For a complex EM problem, Maxwell's equations are cumbersome to deal with since simultaneous solutions are required for both the time-varying electric and magnetic fields. An alternative approach is provided by Jefimenko.

2.1.2 Jefimenko's Equations

Jefimenko's Equations (2.5) and (2.6) give the solution to Maxwell's equations and also show the *causality principle* [8]. That is to say, the terms on the left side of the equal sign in both equations are entirely dependent on the right hand side terms; unlike in Maxwell's differential equations (2.2) and (2.4) where the operations take place on both sides of the equal sign simultaneously. Generally, equations (2.5) and (2.6) are the time-dependent Coulomb's law and the Biot-Savart law to electrodynamics, respectively [8]. Considering a static case, the first term of equation (2.5) becomes independent of retarded time, t_r, and the second and the third terms are dropped out to simplify the equation. Similarly, equation (2.6) is reduced for a static case. It can also be seen that the expression for $\vec{B}$ is independent of $\vec{E}$ and vice versa. Therefore, the electric field is due to ρ, and the magnetic field is due to $\vec{J}$. The electric and magnetic fields are interrelated except at DC where they separate. Thus, charge and current are related by the continuity equation (2.7) [19].

$$\vec{E}(r,t) = \frac{1}{4\pi\epsilon_0}\int\left[\frac{\rho(r',t_r)}{r^2}\hat{r} + \frac{\dot{\rho}(r',t_r)}{cr}\hat{r} - \frac{\dot{J}(r',t_r)}{c^2 r}\right]d\tau' \tag{2.5}$$

$$\vec{B}(r,t) = \frac{\mu_0}{4\pi}\int\left[\frac{J(r',t_r)}{r^2}\hat{r} - \frac{\dot{J}(r',t_r)}{cr}\right]\times\hat{r}d\tau' \tag{2.6}$$

$$\nabla.\vec{J} + \frac{\partial\rho}{\partial t} = 0 \tag{2.7}$$

where c is the speed of light, r' is a point in the charge distribution, r is a point in space and $t_r = t - |r - r'|/2$. The use of retarded potentials to obtain Jefimenko's equations allows a two-step process (integration then differentiation) which simplifies the calculations, rather than directly going to the fields [17]. The application of Maxwell's and Jefimenko's equations has the advantage that they provide qualitative understanding of the problem whereas computational tools give the quantitative description. The other important aspect of electromagnetism is the conservation law which has been presented in the next subsection through the Poynting's theorem.

2.1.3 Poynting's Theorem and Radiation

Poynting's theorem exhibits the classical energy conservation law which states that the total energy density, $\vec{U}$, of EM fields is a combination of energy stored in the fields and

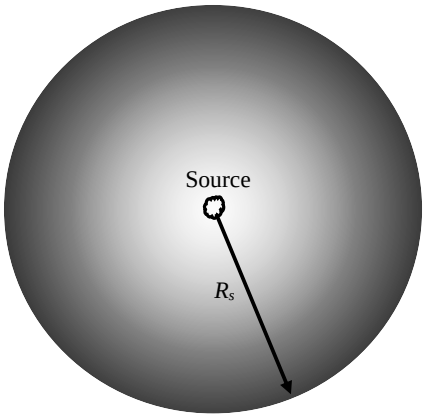

Figure 2.1: Spherical shell of radius, R_s, with a localised source near the origin.

the mechanical (kinetic) energy given as:

$$\vec{U} = \frac{1}{2}\left(\epsilon_0 \vec{E}^2 + \frac{1}{\mu_0}\vec{B}^2\right) \tag{2.8}$$

As briefly mentioned earlier on in this section, a charge that undergoes acceleration radiates and carries with it energy, momentum and angular momentum. The rate of flow of this energy per unit area transported by the fields is known as the *Poynting vector*, $\vec{S}$, and it is along the direction of propagation of the EM waves. Thus, it is easily deduced from the Poynting theorem (vector) that a charge at rest does not produce any radiation; neither does a steady current [15, 17]. In addition, the flow of energy is irreversible as the EM waves propagate into space (to infinity) away from the source.

$$\vec{S} \equiv \frac{1}{\mu_0}\left(\vec{E} \times \vec{B}\right) \tag{2.9}$$

Assuming a large spherical shell of radius, R_s, as presented in Figure 2.1, the total power, $\vec{P}(r)$, ejected through the shell is the surface integral of the Poynting vector:

$$\vec{P}(r) = \oint \vec{S} \,.\, d\vec{\mathrm{a}} = \frac{1}{\mu_0}\oint \left(\vec{E} \times \vec{B}\right) \,.\, d\vec{\mathrm{a}} \tag{2.10}$$

where $d\vec{\mathrm{a}}$ is an infinitesimally defined patch area whose direction is normal to the sphere surface. The radiated power is given by the following equation, taking the limit of $\vec{P}(r)$ as r tends to infinity.

$$\vec{P}_{rad} \equiv \lim_{r\to\infty} \vec{P}(r) \tag{2.11}$$

The expression for the area of the sphere is $4\pi r^2$, thus the condition for radiation to prevail the Poynting vector must decrease (for larger r) slower than $1/r^2$. For instance, if it decreases at $1/r^3$, then obviously $\vec{P}(r)$ would be vanishing at a rate of $1/r$, which implies that P_{rad} would be zero. For a static case, the Coulomb's law and Bio-Savart law from equations (2.5) and (2.6) predict that the magneto-electrostatic fields fall off as $1/r^2$ (or rapidly), thereby making $\vec{S} \sim 1/r^4$: hence no radiation from static sources. However, from Jefimenko's equations the time-dependent fields constitute the terms ($\dot{\rho}$ and $\dot{J}$) which diminish at $1/r$; these are the terms responsible for EM emissions. The energy balance of the radiated EM wave can be disrupted when two or more of such waves interact with each other through the principle of superposition [20].

2.1.4 Superposition Principle

Assuming there is a collection of source currents or charges scattered about at the origin, the superposition principle states that the net field is the (vector) sum of all the individual fields [15]. The application of this principle on EM waves or fields defines what is known as destructive or constructive interference. For destructive interference, the amplitude of the combined fields is smaller than the amplitude of each of the fields taken separately, whereas for constructive interference, the amplitude of the net field is larger than the amplitude of each of the separate components. For example, two identical EM signals propagating in opposite directions can interfere constructively such that the net E-field, E_T, is twice that of the original signals (equation (2.12)) or destructively where the net E-field is zero (equation (2.13)).

$$\left|\vec{E_T}\right| = \left|\vec{E_1}\right| + \left|\vec{E_2}\right| = \vec{E} + \vec{E} = 2\vec{E} \tag{2.12}$$

$$\left|\vec{E_T}\right| = \left|\vec{E_1}\right| - \left|\vec{E_2}\right| = \vec{E} - \vec{E} = 0 \tag{2.13}$$

Using equation (2.8), the electric energy density before the waves interfere constructively is given by:

$$\vec{U} = \frac{1}{2}\epsilon_0 \left|\vec{E_1}\right|^2 + \frac{1}{2}\epsilon_0 \left|\vec{E_2}\right|^2 = \epsilon_0 \vec{E^2} \tag{2.14}$$

However, due to the fact that energy is expressed as the square of the E-field, the net electric energy after superposition is four times that of the individual waves and is mathematically presented in equation (2.15).

$$\vec{U} = \frac{1}{2}\epsilon_0 \left|\vec{E_1} + \vec{E_2}\right|^2 = \frac{1}{2}\epsilon_0 \left(\left|\vec{E_1}\right|^2 + 2\left|\vec{E_1}.\vec{E_2}\right| + \left|\vec{E_2}\right|^2\right) = \frac{1}{2}\epsilon_0 \left(\vec{E^2} + 2\vec{E^2} + \vec{E^2}\right) \quad (2.15)$$

This tends to disregard the energy conservation law and can be understood by considering the behaviour of the H-field. When the E-fields of the two waves interfere constructively, their H-fields undergo destructive interference. Therefore, the magnetic energy density linked to the superposition is zero. This implies that the magnetic energy has been totally converted into electric energy which is seen as the excess energy in equation (2.15). Similarly, for a destructive interference of the E-fields the H-fields interfere constructively, hence the superposition has zero electric energy and four times the magnetic energy of the separate waves. The example given demonstrates that the two waves travelling in the opposite directions exchange energy through superposition. The coupling of EM energy between waves can either be desirable or undesirable depending on the application.

In the field of intentional electromagnetic interference (IEMI), the concept of energy superposition has been exploited, where a target with electronic components is exposed to radiated EM field. In electronic warfare, for example, the use of drones to spy, drop nukes or poisonous chemicals to an enemy country can be impeded by exposing the drones to EM field from an antenna. The radiation from the antenna either causes constructive interference or strong EM field which leads to voltage surges and breakdown to the electronics of the targeted device (drone). This requires the use of a special antenna which will be described later in sections 2.4 and 2.5. The antenna has been developed in the era of ultra-wideband (UWB) technology and because of its hyper-band (HB) characteristics it has wider applications besides the generation of strong EM pulse (EMP) for IEMI.

2.2 Ultra-wideband Technology and Applications

The classification of the EM environment is relevant in defining various technologies applied in the contemporary society. Though different schemes have been used to classify the EM environment, the bandwidth classification scheme is favoured as it quantitatively describes the environment [7]. Thus, from the name UWB, it is obvious that UWB antennas are distinguished from other antennas by bandwidth. There are two guidelines that can be used to identify whether an antenna is UWB or not. The first guideline was issued in DARPA report in 1990, where a radar which had a fractional bandwidth, B_{frac}, greater than 25 % would be considered UWB [20, 12]. However, a more recent restriction imposed by Federal Communications Commission (FCC), reduced the limit of B_{frac} to a minimum of

20 % [20, 12]. Thus, the B_{frac} can generally be represented by the following mathematical expression:

$$B_{frac} = 2\frac{f_H - f_L}{f_H + f_L} \geq \begin{cases} 0.25 & \text{DARPA} \\ 0.2 & \text{FCC} \end{cases} \tag{2.16}$$

where within the operational band of the antenna, f_H and f_L are the upper and the lower frequencies, respectively. The other criteria provided by the FCC to qualify an antenna as UWB is when the bandwidth of the antenna exceeds 500 MHz.

$$500 \text{ MHz} < |f_H - f_L| \tag{2.17}$$

Strictly speaking, the DARPA and FCC definitions in equation (2.16) for B_{frac} are merely for regulating the available frequency bands. In addition, it assumes that the centre frequency is the mean value of the upper and lower operating frequencies but for many reasons, the geometric mean is preferred [20]. A case for a 500 MHz bandwidth at 5 GHz would give a B_{frac} of 10 %, yet for the purposes of regulation it is considered UWB.

In [7, 21] four types of bands have been defined based on bandwidth classification scheme. The four-band categories include [7]: (a) narrow or hypo-band (B_{frac} <0.01), (b) moderate or meso-band (0.01 < B_{frac} ≤1), (c) ultra-moderate or sub-hyper-band (1< B_{frac} <1.634) and (d) hyper-band (1.634< B_{frac} <2). Considering the nature of modern technologies, the definition in [7] covers more ground, and hence will be the favoured criteria in this dissertation.

Typically, there are three categories of UWB antennas based on their applications, namely the DC–to–daylight, multi–narrowband and the modern class [20]. Of great interest in this particular research is the DC–to–daylight category where the antenna is designed to offer the largest possible bandwidth. Some of the well known applications of this class of UWB antennas include ground penetrating radar (GPR), electromagnetic compatibility (EMC), communication systems, time domain, TD, IEMI, impulse radar and electromagnetic weapons. The greatest challenge in designing UWB antennas is matching the antenna over such a large bandwidth of operation [12]. The key contributions of this research is to properly match the HB antenna under study; an impulse radiating antenna (IRA).

Section 2.4 introduces an IRA antenna through a brief historical overview and then in the subsequent section various components of IRA are discussed in detail. Before the introduction of the IRA, we describe what an antenna is through the following analogy.

2.3 Antenna and Elephant Analogy

In the ancient India subcontinent, a parable is told of six blind men who wanted to inspect and understand a peculiar animal (elephant) by touch [22]. One touches the tail and claims that the elephant is a rope. The second finds the side and says that the animal is a wall. The third feels the trunk and is convinced that it is a thick snake. Another declares that it is a tree by touching a leg. The fifth reaches the ear and believes that the animal is a fan. The sixth grabs a tusk and tells others that it is a spear. These blind men were correct in their separate experiences because each had part of the truth. However, they fully understand the nature of the animal in Figure 2.2 by putting together their various perspectives. An antenna can be considered as an "elephant". For example:

- An antenna designer who desires a specific pattern describes an antenna as a radiator. Thus the designer would be interested in the geometrical structure of the antenna that would allow the coupled fields to be configured in a particular fashion.
- An antenna engineer who considers optimization of an antenna through matching, conceives an antenna as an extension of a transmission line. Therefore, an antenna engineer would focus on improving the quality of the match by controlling the impedance of the transmission line such that there is a smooth transition of the guided waves from the structure into free space.
- An engineering scientist who desires to understand antennas considers them as energy converters. Astrophysicist, for instance, may see them as structures that convert EM energy from deep space into another form of energy that they can attach some scientific meaning. Such appreciation of how antennas operate give insights that lead to advanced and better performing antennas.

Therefore, in order to truly understand the elephant in question (IRA) one needs to assimilate all the various components thereof. These components are discussed in section 2.5.

2.4 Background of Impulse Radiating Antenna

Impulse radiating antennas (IRAs) are considered to be in the class of focused aperture antennas [23]. They have been widely used to generate and radiate HB EM impulses in a very short period of time [24, 25, 26, 27]. The initial concept that led to the development of IRA came from Carl Baum in 1989 [6]. This type of antenna has found various applications in remote sensing, non-destructive testing, transient radars to detect mines or buried

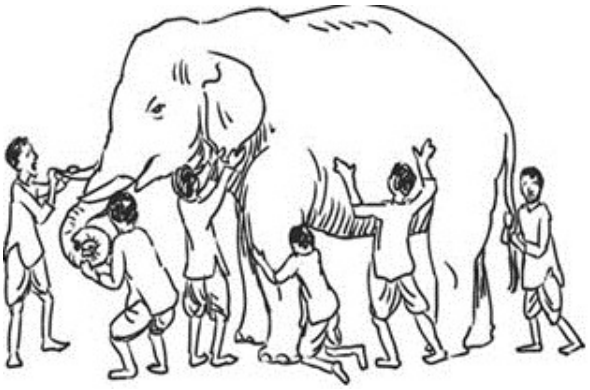

Figure 2.2: The six blind men and the elephant [22].

bodies underground, generation of nuclear electromagnetic pulse (NEMP) simulators for EMC and vulnerability tests on electronic and IT devices, UWB communication systems and electromagnetic jamming – the concept involves focusing high-power electromagnetic (HPEM) waves on a particular target to compromise the target's mission by interfering with or destroying its electronic components [28, 29]. In the proposed study we want to design it for low-power EMC and RFI related measurements because of its hyper-band nature while using just a single TD pulse.

2.5 Design Components of an IRA

IRAs are composed of self-reciprocal transverse electromagnetic (TEM) conical transmission lines which feed a focusing optics. Usually, the focusing optics is either a lens or a reflector (or sometimes a timed array). However, in most practical applications reflectors are the preferred choice because of their low volume and light weight [30]. The principal of operation of the antenna is that a spherical wave is launched at the feed point (source) and propagates through the non-dispersive TEM transmission line feed structure of characteristic impedance, Z_{line}. By geometric optics approximation, the parabolic reflector converts the spherical mode on the feed structure into a plane wave in the near-field. The boresight radiated far-field, E_{rad}, can be approximated using aperture theory (physical optics) and is given as:

$$E_{rad}(r,t) = \frac{\iint_{S_a} E(x,y)dxdy}{V_0 2\pi r c} \frac{dV(t)}{dt} \tag{2.18}$$

where $V(t)$ is the applied voltage waveform, V_0 is the peak of the applied voltage under step function excitation, c is the speed of light, r is the distance to the observation point

and $E(x, y)$ is the electric field in the TD on the surface integral defined by aperture S_a. Equation (2.18) indicates that the E-field in the far zone at boresight is proportional to the time derivative of the applied voltage. Therefore, when a fast rising step, a short duration pulse, is launched at the antenna's feed point, it produces a high amplitude impulse-like waveform. For the early time, t, the E_{rad} can as well be approximated by the following equation [23].

$$E_{rad}(r, t) = -\frac{h_a}{2\pi r c f_g}\frac{dV(t)}{dt} \tag{2.19}$$

where h_a is the aperture height expressed as [31].

$$h_a = -\frac{f_g}{V_0}\iint_{S_a} E(x, y)dxdy \tag{2.20}$$

and $f_g = Z_{line}/\eta_0$ is the normalized feed impedance of the TEM transmission line feed, Z_{line} is the characteristic impedance of the feed arms and η_0 is the impedance of free space. The quantity, h_a can also be used to determine the received peak waveform given in equation (2.21).

$$V_{rec}(t) = -h_a E_{inc}(t) \tag{2.21}$$

where E_{inc} is the magnitude of the main component of the incident field. Generally, in pulsed antennas such as an IRA, the far-field is the time derivative of the applied voltage, whereas, the received voltage is a replica of the incident field [32]. On the other hand, in CW antennas, the transmitting and receiving patterns are identical [32]. It should be noted that equations (2.19) and (2.20) are exact within a time window known as the *clear time of the antenna* and time domain physical optics is not an approximation [33]. During this time, secondary interactions occur such as diffraction effects or scattering from the feed point or reflector edges towards the observer. The fields are referred to as "prompt" and the observer sees the antenna as infinite. However, beyond the clear time, focused aperture fields can be different due to diffraction effects which interfere with ideal early time-fields [34].

In most cases the clear time is linked to the size of the aperture and on the order of L/c, where L is any linear dimension that dominates the response, depending on a particular IRA configuration [30]. Commonly known physical dimensions are radius of the reflector and length of the feed-arm. The following subsections discuss various components of IRA in detail, starting with the focusing optics, then conically-symmetric TEM structure,

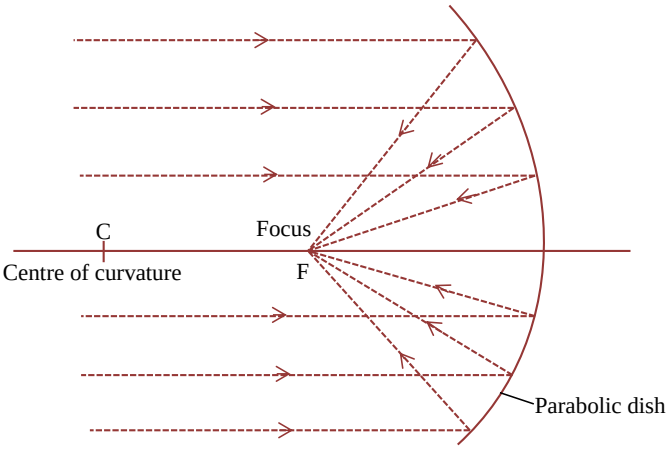

Figure 2.3: Electromagnetic (EM) waves incident on a parabolic dish.

followed by the balanced feed system and lastly the resistive termination load and the feed impedance in subsection 2.5.4.

2.5.1 Focusing Optics

As mentioned earlier in this section most of the commonly used focusing optics is the parabolic reflector or dish. It is formed by a parabolic curve rotated about an axis which passes through the principal focus and the centre of the curve (see Figure 2.3). They have been utilized worldwide in telescopes, radar and satellite communication. An IRA dish works the same way as a concave mirror in a reflecting optical telescope. When EM waves from a distant source (parallel to the principal axis) are incident on the dish, they are reflected to a common point (the focus) as shown in Figure 2.3. Since the antenna is self–reciprocal, the path is reversed in a transmitting antenna: the EM waves originating from a point source at the focus are now reflected as a beam of rays parallel to the principal axis of the dish, and into infinity.

IRAs are robust antennas which can yield greater directivity. According to equation (2.22), the total gain it can achieve depends on the size of the aperture as well as the input impedance of the antenna. The gain, G_{dBi}, of a dish antenna is expressed as:

$$G_{dBi} = 10 \log_{10} \left(\eta \frac{4\pi}{\lambda^2} S_a \right) \tag{2.22}$$

where η is the efficiency of the antenna with reference to an isotropic radiator and S_a is the aperture area. The size of the dish is the designer's preference and usually depends on the project environment, cost and the type of reflector available. For the early design in

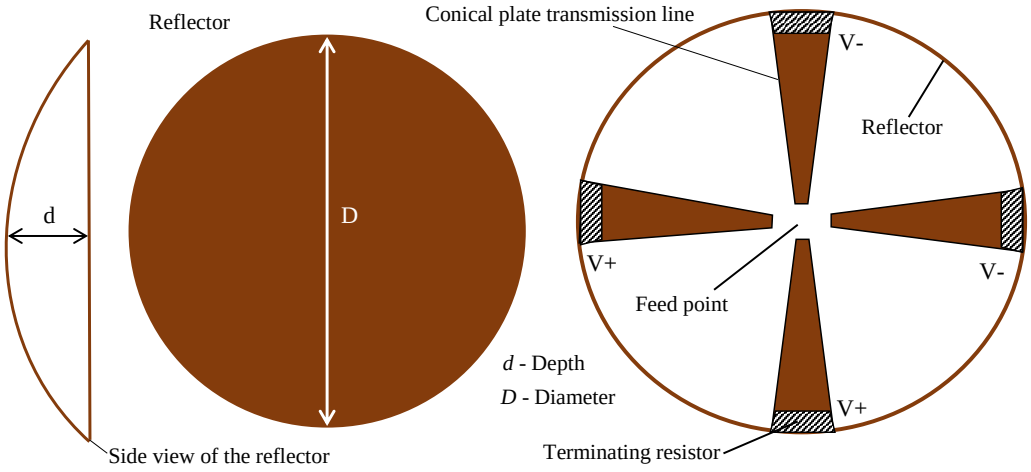

Figure 2.4: The basic components of an IRA.

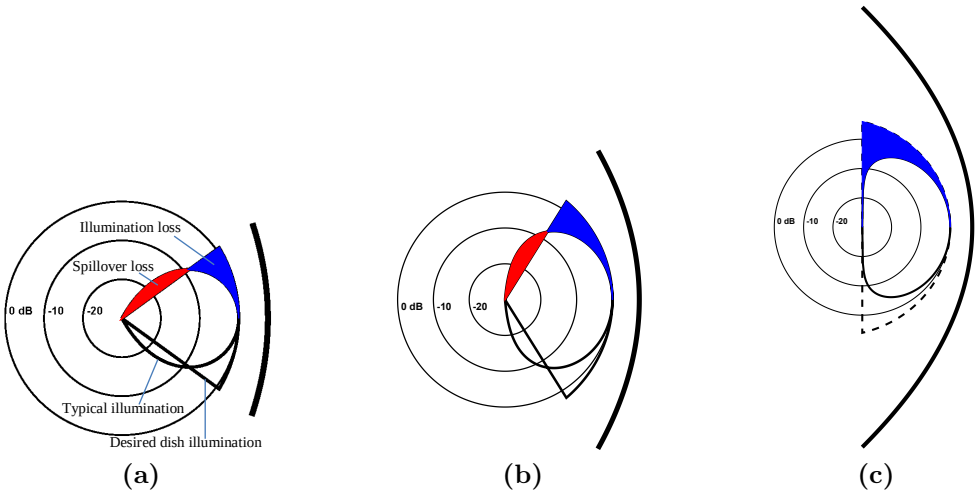

Figure 2.5: Dish illumination for various F/D ratios (a) $F/D = 0.75$ (b) $F/D = 0.45$ (c) $F/D = 0.25$ [35].

[13], the reflector was selected based on two main factors: the availability of the reflector material and a reflector that is easily transported (to the Karoo) over long distance through rough terrain during measurement campaigns. In order to describe a simpler way of how much a parabola is used, an F/D ratio is determined. It is the ratio of the focal length, F, to the reflector diameter, D. Once the aperture diameter, D, and the depth, d (Figure 2.4) have been measured, the focal length is calculated using the following equation.

$$F = \frac{D^2}{16d} \tag{2.23}$$

Figure 2.5 shows relative geometries for various F/D ratios, each with the desired and idealized feed patterns. It can be noticed that as the F/D reduces a typical feed-horn

pattern broadens. Therefore, different feeds are required to optimally illuminate reflectors with different F/D ratios: the feed-horn pattern must be properly matched to the reflector F/D. A dish with large F/D requires a feed with moderate beam width (Figure 2.5 (a)) while a dish with $F/D = 0.25$ (Figure 2.5 (c)) has the focus level with the edge of the dish, such that there is 180 degrees angle of illumination. In this case, the edge of the dish is twice as far from the principal focus as the centre of the dish. Thus, the desired pattern must be 6 dB stronger (inverse-square law) at the edge as in the centre. This will be an intricate pattern to generate, and as a result, not possible to properly illuminate a dish that deep.

Also, from Figure 2.5 we see that the idealized pattern has been superimposed on the desired pattern; the energy is concentrated more at the centre than at the edges and some entirely miss the dish. The energy that misses at the edges (given in blue) is known as *illumination loss* while the energy that misses the reflector (given in red) is known as *spillover loss*. An attempt to have more energy at the edge of the reflector will lead to more spillover. On the other hand, reducing the spillover implies that the outer part of the dish is not efficiently illuminated and does not contribute to the gain. Hence, to effectively illuminate the dish one needs to increase energy near the edge of the dish and have the energy drop off very quickly beyond the edge.

Most of the IRA designs have F/D ratios within the range of 0.3–0.4 with 0.4 being the most preferred ratio [36, 37, 38, 39, 40]. The diameter of the available reflector for the initial IRA [13], is 850 mm and the focal length is 320.26 mm giving an $F/D = 0.38$. Attached to the reflector from the feed point are the conical TEM lines which are part of the feeding structure, see Figure 2.4.

2.5.2 Conically-symmetric TEM Structure

In designing the IRA antenna the most interesting components are the launcher plates which are used as a pair of crossed conical coplanar TEM transmission lines. Thus, the feeding structure has four arms originating at the focal point and are terminated at the rim of the parabolic reflector through the termination loads [41]. A schematic of a traditional reflector IRA is shown in Figure 2.6. It is useful in understanding the design equations for the feeding lines. The conically symmetric TEM structure parameters $(\beta_0, \beta_1, \beta_2)$ can be linked to the equivalent longitudinally symmetric structure parameters (a, b_1, b_2, D, F) through stereographic projection and conformal mapping [42] as:

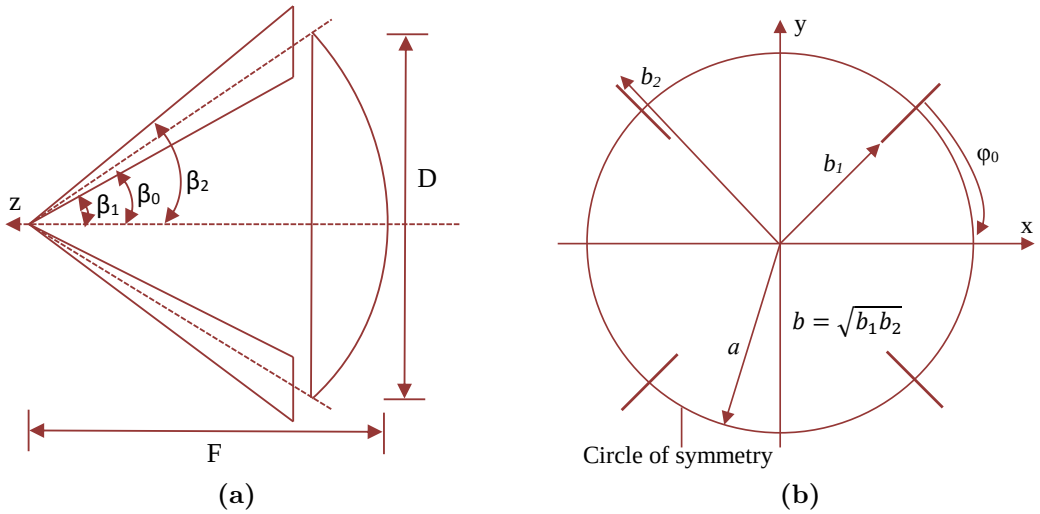

Figure 2.6: Schematic diagram of a typical reflector IRA (a) Side view with conically symmetric structure parameters $(\beta_0, \beta_1, \beta_2)$ (b) Aperture plane after stereographic projection.

$$\beta_0 = \arctan\left(\frac{1}{2\left(\frac{F}{D}\right) - \left(\frac{D}{8F}\right)}\right) \tag{2.24}$$

$$\beta_1 = 2\arctan\left(\sqrt{\frac{b_1}{b_2}}\tan\left(\frac{\beta_0}{2}\right)\right) \tag{2.25}$$

$$\beta_2 = 2\arctan\left(\frac{b_2}{b_1}\tan\left(\frac{\beta_1}{2}\right)\right) \tag{2.26}$$

$$\frac{b_1}{a} = \frac{\tan\left(\frac{\beta_1}{2}\right)}{\tan\left(\frac{\beta_0}{2}\right)};\quad \frac{b_2}{a} = \frac{\tan\left(\frac{\beta_2}{2}\right)}{\tan\left(\frac{\beta_0}{2}\right)};\quad a = \sqrt{b_1 b_2} \tag{2.27}$$

where a describes the radius of the circle of symmetry and φ_0 is the angle between the launcher plates and the horizontal axis as depicted in Figure 2.6 (b). Once the focal length F, diameter D, and φ_0 have been chosen and the values of b_1/b_2 specified (same as specifying input impedance), β_0, β_1 and β_2 can be calculated using equations (2.24), (2.25) and (2.26), respectively.

From [43] an optimum aperture efficiency has been obtained by properly specifying a set of β_1, β_2 and φ_0. The values of φ_0 and b_1/a that give the maximum aperture efficiency are 70° and 0.84, respectively [43]. These values have been obtained through simulation methods which have not included diffraction effects and aperture blockage. At $\varphi_0 = 70°$ the antenna achieves more uniform aperture field distribution that leads to more gain and

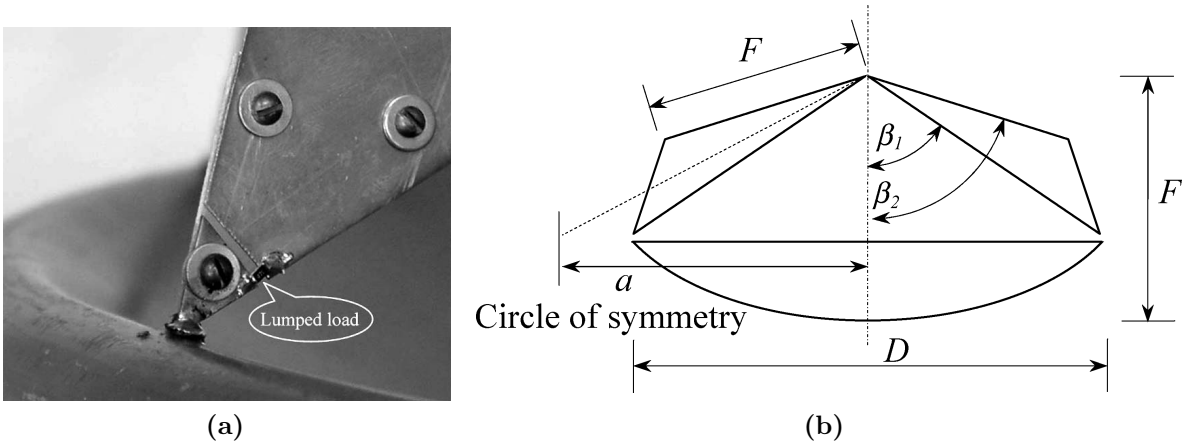

Figure 2.7: (a) Arm–reflector junction of the reflector IRA with single tapered feeding arm and the termination load (b) Diagram of the reflector IRA with single tapered feeding structure [45].

efficiency. The $\varphi_0 = 45°$ for the original IRA designs (and mainly chosen because it has a closed form of analytic solution [25]) is not the best design for the feeding structure. However, it should be noted that increasing φ_0 at constant β_1 and β_2 will result into higher feed impedances as described in subsection 2.5.4 and in chapter 3 subsection 3.2.2. As an example, if a 200 Ω feed impedance is required, β_1 and β_2 must be changed to obtain fatter arms which will increase blockage, therefore $\varphi_0 = 60°$ has been proposed in [44].

At the arm-reflector junction there is some stored energy due to the standing wave effects at the end of the feeding arm. The standing waves on the typical feeding arms cannot be removed by any combination of termination lumped loads [41]. A practical way to reduce the stored energy around the junction (in order to increase the gain) is to taper the end parts of the feeding arms (see Figure 2.7). A lower coupling is attained with the tapered junction in comparison to the traditional feeding arm and consequently the stored energy is reduced. Further standing wave effects can be reduced if sharp variation in the arm width at the tapering point is avoided [45]. In general, the feeding structure can be changed to reduce end effects, aperture blockage at lower input impedances and to achieve low reflection coefficient over a wider frequency spectrum. This will enhance optimization of the aperture field.

2.5.3 Balanced Feed System – Balun

In most radiation structures balanced antennas limit the design to using balanced transmission lines especially at high frequencies [46]. Such a design considers interference and shielding effects. However, to feed a balanced antenna with an unbalanced transmission

line has always been a great challenge to antenna designers [47, 48]. It is even more challenging for a balanced HB IRA, due to its phase linearity and multi-octave frequency bandwidth. As an example, tapered baluns have been used where a Vivaldi and TEM horn antennas were installed as feeding structures [49]. The tapered-balun size should be at least of the order of the wavelength of the lowest frequency. At higher frequencies, it is long enough to generate some radiation losses. To avoid such losses, one should consider (during the design stages) the characteristics mentioned in chapter 1.

In most cases a balanced antenna has at least one potential symmetry plane which makes it possible for grounding because of the symmetric structure. For instance, in a dipole antenna the symmetry plane crosses the antenna axis at the feeding point thereby dividing it into two poles. If the objective is to achieve an exact distribution of currents on the two poles (even symmetry), then the antenna must be fed in a particular fashion.

Firstly, one can feed a balanced antenna with a balanced source placed at the feeding point as shown in Figure 2.8 (a). Since the structure is symmetric the current will have distributed evenly on the poles, hence the antenna is said to have been fed properly. Nonetheless, this direct way of feeding is not usually possible. Therefore, transmission lines are always used to deliver the power to the antenna.

Secondly, there is the option of using a balanced source and a balanced transmission line to feed the antenna. Since all components are balanced the input current must have even symmetry so that there is equal distribution of currents on both sides (see Figure 2.8 (b)). Unfortunately, balanced sources and transmission lines can leak at higher frequencies which prompts the use of shielded sources and unbalanced coaxial cables as a feeding network [46]. Using Figure 2.8 (c), let us assume that the power produced by an unbalanced source is delivered to the antenna by a coaxial cable. The inner conductor of the coaxial cable is connected to the upper pole of the balanced antenna and the cladding is joined to the other pole. We can now express Kirchhoff's current law as:

$$I_1 = I^+ e^{-j\beta l} - I^- e^{+j\beta l} \tag{2.28}$$

$$I_2 = I^+ e^{-j\beta l} - I^- e^{+j\beta l} + I_{out} \tag{2.29}$$

where I^+ is the forward current, I^- is the reflected current, I_{out} is the outer layer current of the coaxial cable, l is the length of the coaxial cable and β is the propagation constant of the coaxial cable. The reference plane is at the junction of the source and the coaxial cable. This descriptive model shows that if $I_{out} \neq 0$, then $I_1 \neq I_2$, which implies that the

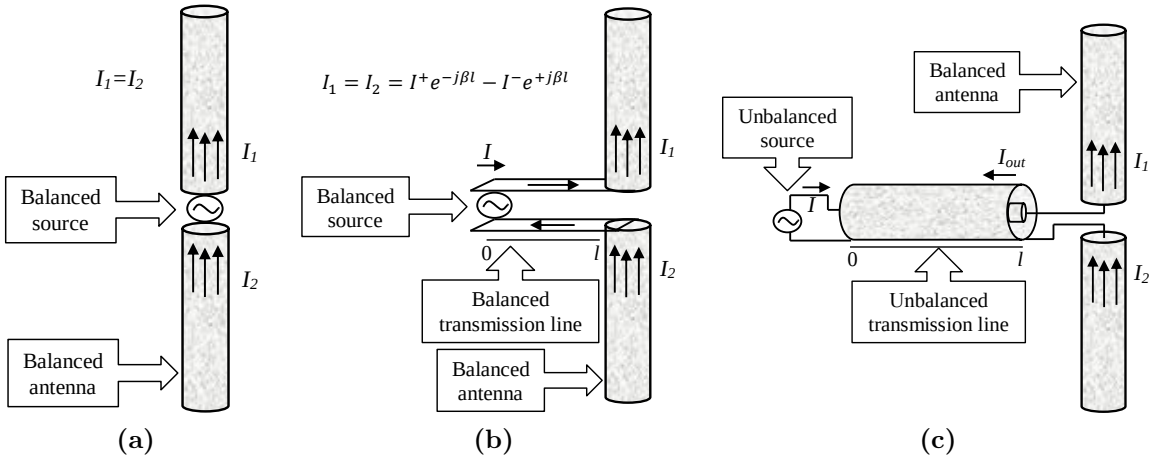

Figure 2.8: (a) Feeding a balanced antenna with a balanced source at the feed point (b) Feeding a balanced antenna with a balanced source through a balanced transmission Line (c) Feeding a balanced antenna with a unbalanced source through a unbalanced transmission Line.

antenna is not fed in a symmetric way. The existence of unbalanced current on the body of the antenna will produce an asymmetric E-plane far-field pattern. In addition, the current on the outer layer of the coaxial cable normally radiates in an improper direction and polarization. To deal with this problem, I_{out} in equation (2.29) has to be forced to zero. Conventionally, a balun is utilized to force I_1 to be equal to I_2 for various antennas. A similar concept can be applied in the IRA but with an HB balun.

Most of the pulse generators have an unbalanced coaxial output with a 50 ohm source resistance. Therefore, to connect a 50 ohm voltage source to a 200 ohm input of IRA, a 50 to 200 ohm transformer is required. In the conventional transmission line balun, a single-ended voltage is converted into a differential voltage with a voltage gain of 2 [50, 51, 52]. A factor of 4 in impedance implies a factor of 2 increase in voltage, given that the power is constant. This is an important characteristic considering that many baluns have losses. The initial IRA (Figure 2.9 (b)) at our Engineering Department used a balun which had a resistive divider with a one–to–two splitter configuration (the T– or Y–layout), Figure 2.10.

An external pulse-generator, through a coaxial cable, is connected to one of the tail ends of the balun with characteristic impedance of 50 ohms. The other two tail ends (each designed as 75 ohms) are separately connected to 75 ohm cables that run to the focal point of the reflector (refer to Figure 2.9 (a)). One of the cables pass through the centre of the dish while the other along the side of the conically symmetric transmission line structure. The cables are connected in parallel at the balun and in series at the principal focus. Positive excitation is achieved with parallel combination of the two of the launcher plates while the other parallel combination of the plates is negatively excited. Thus, each

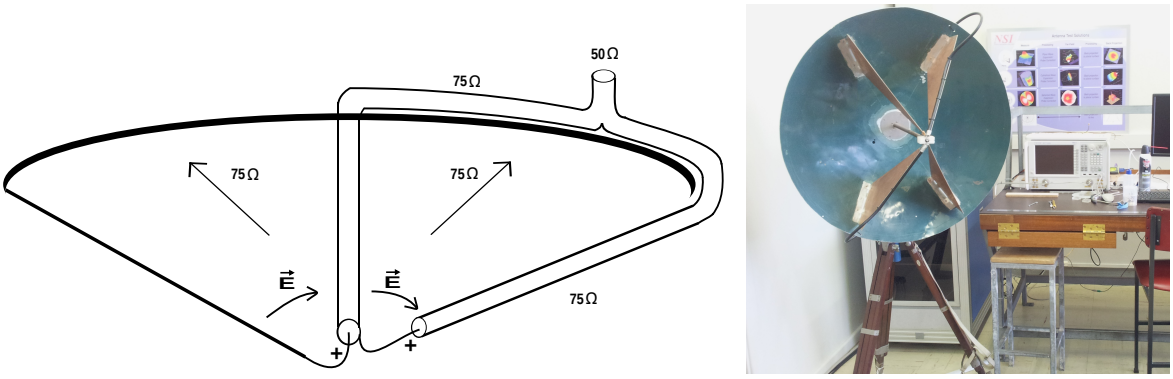

(a) (b)

Figure 2.9: (a) Cable layout of a single fed IRA with feed impedance of 150 Ω (b) Front view of early design of IRA at Stellenbosch University, engineering department.

(a) (b)

Figure 2.10: (a) A picture of a T–layout splitter and (b) A Y–junction splitter used on the initial IRA (Figure 2.9 (b)) [13].

of the feed arms terminate as 150 ohms at the reflector so as to achieve a feed impedance of 150 ohms between the two pairs of the feed arms. Most of Farr's designs have used this balun technique. Although, a 50–150 Ω balun configuration has been used, the choice of a particular configuration depends on the feed impedance.

2.5.4 Resistive Termination Load and the Feed Impedance

The conical plate feed lines and the reflector (already discussed in the previous subsections) are electrically connected by terminating the plates with resistors onto the parabolic reflector. The most important aspect to consider is the matching of the resistor values to the combined feed impedance of the plates. Usually when resistors are connected they are spread across the plates to ensure equal current flow from the plates to the dish [13].

In the design aspect, feed impedance is the parameter to be evaluated. Figure 2.11 gives a family of curves of η (aperture efficiency) against Z_{line} (input impedance) for distinct

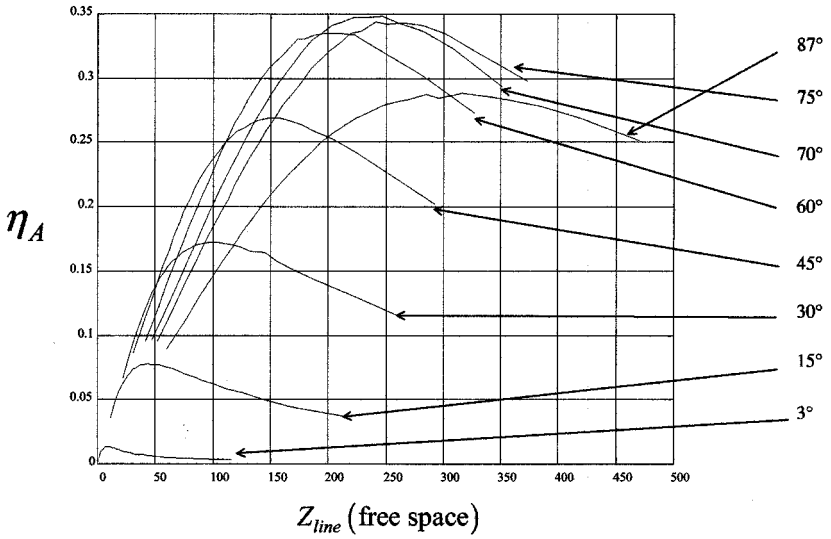

Figure 2.11: Plots of aperture efficiency versus feed impedance (in free space). The curves shift to the right as φ_0 increases. There is monotonic increase of optimum feed impedance with φ_0 [43].

values of φ_0. The plots show that for any given value of feed impedance, there is a unique geometry that gives the maximum aperture efficiency. These curves can be used to design a given feed geometry that would match the impedance of an individual source [43]. Secondly, as φ_0 increases the feed impedance at optimum aperture efficiency also increases. From the graphs, the optimum angle for impedances 100, 150, 200 and 250 Ω can be approximated as 30°, 45°, 60°, and 75°, respectively. An absolute optimum configuration is achieved when $\varphi_0 = 70°$ and $f_g = 0.65$ (247 Ω in free space).

According to these results the combination of $\varphi_0 = 60°$ and $Z_{line} = 150\ \Omega$ as in (the initial IRA design) [13], gives $\eta = 31\,\%$ whereas the combination of $\varphi_0 = 60°$ and $Z_{line} = 200\ \Omega$ gives an optimum value of η as 34 %. But the optimum configuration achieved with the latter combination of φ_0 and Z_{line} requires higher impedance coaxial cables. A 150-Ω IRA will have more aperture blockage than a 200-Ω IRA. The Stellenbosch IRA was built as a 150-Ω because 75 Ω cables are easier to find than 100 Ω cables. Smaller the impedance, wider will be the plates contributing to aperture blockage. The next section presents the only two domains that are used in this dissertation in the analysis of results.

2.6 The Time and Frequency Domains

It is desirable that the fundamental properties of EM waves (signals) and how they interact with various interconnects are considered in different *domains*. Each domain provides a different perspective of how the signal is seen and characterised. The fastest route

to an acceptable solution may not be the most obvious one! To be specific, only time and frequency domains are used throughout this dissertation. Since the two domains are intimately linked, it is possible to translate between them using special algorithms known as the Fourier Transform and Inverse Fourier Transform.

However, the choice of a particular domain depends on the speed of obtaining the answer or the nature of the problem such that the problem can easily be understood and described in a specific domain. For instance, the concepts of rise-time and bandwidth are intrinsically related to time and frequency domains, respectively. Therefore, if the issue is well defined by bandwidth then frequency domain (FD) would be the favoured choice.

2.6.1 Time Domain

The term *time domain* (TD) – is commonly used in engineering and science but what does it really imply? What are the unique characteristics of TD which make it effective? These are not difficult questions to answer but since we rarely think about them, they can be very challenging. Essentially, TD defines the real world as it is the only domain that actually exists [53]. From the time of birth, people's experiences are nurtured and calibrated in TD and it is for this reason that it is sometimes taken for granted. Different events are seen to occur with a time stamp and in sequential order. The modern world is controlled by high-speed digital electronics which heavily depend on TD.

In order to assess the behaviour of a digital device, a typical analysis is done in the TD because that is where optimum performance is measured [53]. As a case in point two important properties of a clock waveform can be considered: period and rise-time (see Figure 2.12). The clock period, T_{clock}, is the time taken for a complete clock cycle and is normally measured in nanoseconds (ns). The clock frequency, F_{clock}, refers to the number of complete cycles per unit time made by the clock and is inversely related to the clock period as defined:

$$F_{clock} = \frac{1}{T_{clock}} \tag{2.30}$$

The rise time is linked to the transition time of the signal from low to high value. The two commonly known definitions of rise time are; the 10–90 and the 20–80 rise times. The 10–90 rise time is normally the default and it shows the time taken for the signal to transition from 10 % of its maximum value to 90 % of its maximum value. The values can be obtained directly from a TD plot. The relationship between the frequency and the period in equation (2.30) gives a rough idea of how bandwidth (range of frequencies) is

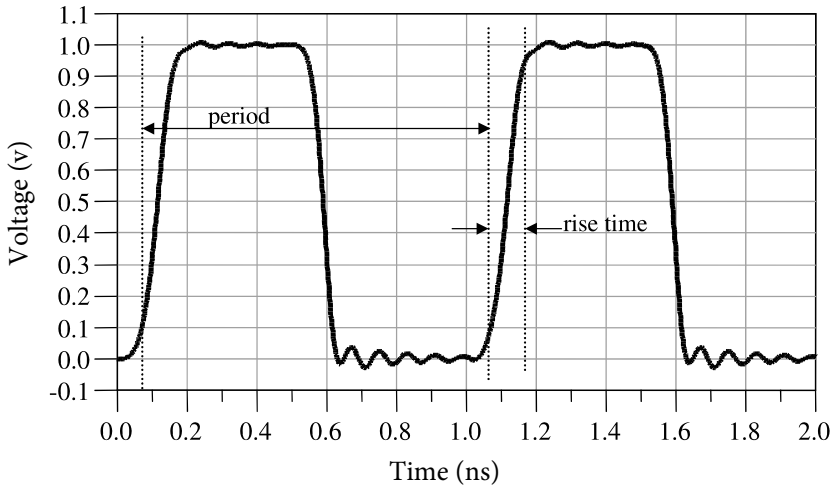

Figure 2.12: A typical clock waveform illustrating the clock period and the 10–90 rise time [53]. The clock frequency is 1 GHz. Usually the fall time is a bit shorter than the rise time and may generate more noise to the system.

dependent on the rise time. This explains how the use of short pulses in IRA qualifies them as HB antennas and why their use in TD is very relevant. Having distinctively reviewed TD as a way of analysing the world, we can now shift to the other domain, FD, and briefly discuss how to consider events.

2.6.2 Frequency Domain

Besides TD, FD is the other preferred domain that is widely used in many applications such as radio frequency (RF) and high-speed digital systems [53]. The key aspect of the FD is that it is not real. It is a mathematical tool which is governed by very specific rules. And one of the rules is that it uses sine waves as the only waveform [53]. However, there exists other domains which operate with other special functions. The algorithm used to compress a JPEG file, for example, takes advantage of very unique waveforms – *called wavelets* – that can convert the space domain into another mathematical language which requires less memory to interpret the same piece of information [53]. Another possible assumption could be that FD utilises sine waves because they can be superposed to create any TD waveform. While this is a very important characteristic of sine waves, it is not unique. The following properties of sine waves are used to define any other waveform [53].

- Superposition of sine waves can lead to any waveform in the TD that is perfectly and distinctively defined.
- Any two sine waves with different frequencies are orthogonal to each other. The

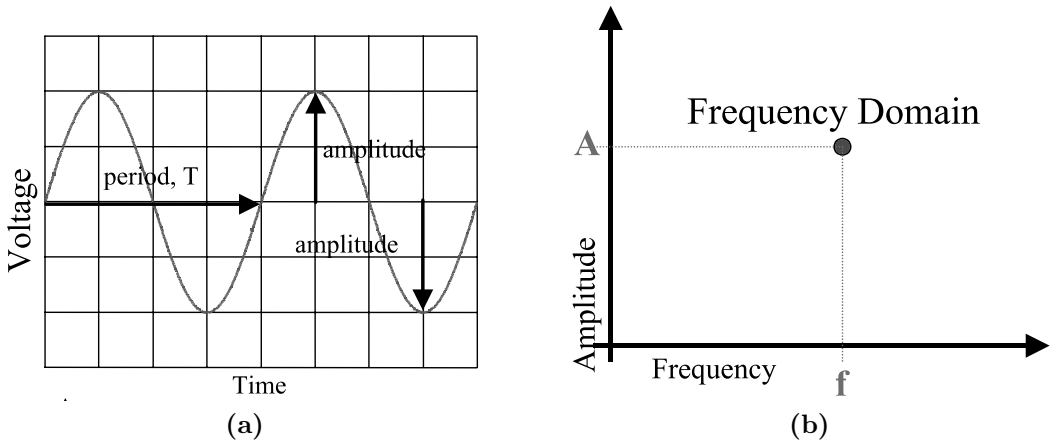

Figure 2.13: (a) Voltage-time graph describing a sine wave in the TD and it comprises many data points (b) Illustration of a sine wave in the FD and is composed of a single data point [53].

integral of the product of the two waves over all time, equals to zero. This implies that each component can be delinked from each other.

- Sine waves are well described mathematically.
- They have a value everywhere with no infinities and their derivatives have no infinities anywhere. This implies that they can be used in describing real-world waveforms because there are no infinities in the real world.

These four properties are very useful but are not exclusive to sine waves. Orthonormal or basis functions such as Legendre Polynomials, Laguerre Polynomials, Bessel Functions can as well define a TD waveform [53]. Electrical problems are sometimes easily understood and solved using sine waves and this is the main reason they are the only functions employed in FD.

Figure 2.13 shows a simple sine wave plot both in TD and FD. The curve can completely be described by three terms, namely: amplitude, phase and frequency. It is a similar curve that would be traced by a rope when one end of the rope is tied on a wall and the other end is perturbed through a vertical displacement. Using this analogy, the amplitude can be defined as the maximum position attained by the vibrating particle of the rope from its mean position. Frequency is the number of complete revolutions per unit time made by the vibrating particle (sine wave) and the phase is a more intricate parameter which locates the wave in its cycle at the start of the time axis. A voltage-time plot in TD for a full sine wave curve requires more data points whereas a corresponding plot in FD is a single data point (Figure 2.13). The question now is:

In designing HB antennas, which domain should an antenna design engineer rely on?

TD and FD complement each other when analysing physical signals. FD has been typically favoured in many electromagnetic applications because of the attractive harmonic functions that generally take the form e^{jwt} [53]. The superposition of sine waves generate these harmonic functions which offer perfect approximations for periodic systems that exhibit steady-state behaviour. However, in many cases, especially when dealing with physically real signals (with definite limits) then harmonic functions do not offer accurate descriptions.

The limitations of harmonic systems become evident when one shifts to transient (non-steady-state) systems. As an example, equation (2.31) has been modelled in MATLAB to superpose harmonic functions in order to create a step function (square wave) shown in Figure 2.14. Much as the modelled signal becomes better as the value of K increases (refer to Figure 2.14), there are overshoots and ringing termed as the *Gibbs Phenomenon* [54, 55, 56, 57]. This effect confirms the convergence of Fourier series [58]. Also, the over-dependence on harmonic signals has been heavily critiqued in [58], where it is referred to as the *Dogma of the Circle*.

$$S_K(x) = \sum_{k=0}^{K} \frac{sin[(2k+1)x]}{2n+1} = sin(x) + \frac{sin(3x)}{3} + \frac{sin(5x)}{5} + ... \tag{2.31}$$

In a nutshell, TD offers access to other functions which model fast rising transient (HB) signals more accurately than the harmonic ones. Therefore, it is good practice for an HB design engineer to be bilingually well versed in TD and FD.

2.6.3 Time Domain Metrology

The term metrology refers to the science of measurement. Thus, *time domain (TD) metrology* means scientific study of measurement in TD. In chapter 1 we mentioned that a TD system has the advantage of transmitting and measuring a broader spectrum of frequencies with a single TD pulse. This single pulse with a sub-nanosecond rise time produces instantaneous energy from DC to microwave frequencies. A large bandwidth sampling oscilloscope can be used to measure and characterise these fast-rising transients. The sampling oscilloscope acts as an analogue sample-and-hold device with an extremely narrow sample time to allow analysis of transient responses with microwave frequency components [59]. This differs from the modern digital scopes where real-time transient signals are directly sampled for data processing or on-screen display. The signals are sampled as 1:1 and are limited by the Nyquist criterion [60]. Figure 2.15 (a) shows an illustration of real-time sampling.

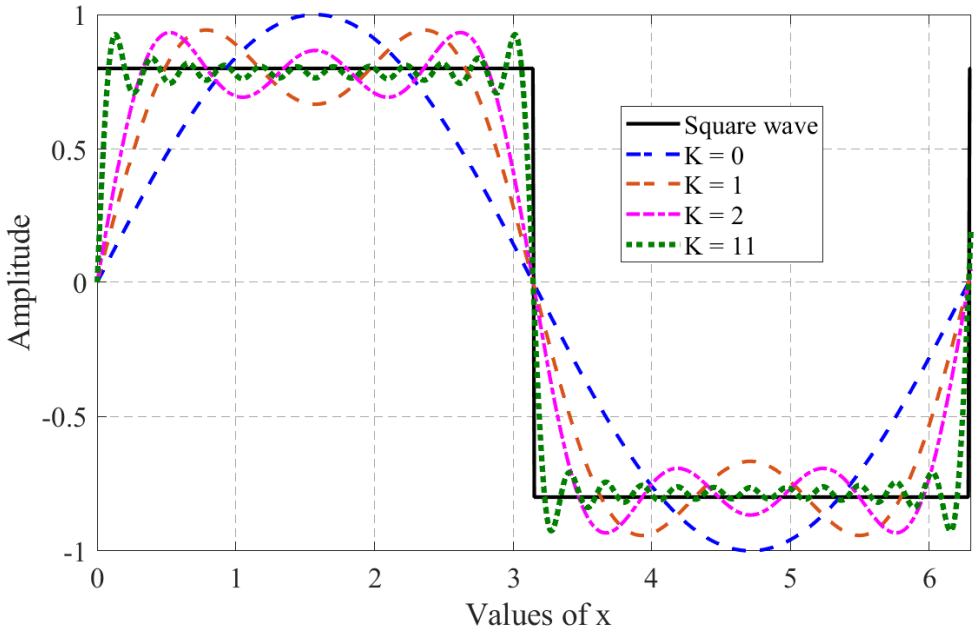

Figure 2.14: Superposition of harmonic functions to demonstrate Gibb's effect through modelling of equation (2.31) in MATLAB for K=1,2,11.

For a fast-rising transient with high frequency content, a larger bandwidth oscilloscope is necessary. The electronics within a real-time scope are not capable of sampling a fast-rising impulse 1:1, hence the need for an alternative sampling technique. Sampling oscilloscope introduces an improved method known as sequential sampling. The oscilloscope is synced with a synchronising pulse which informs it that a signal is inbound. When the oscilloscope has been triggered a sample is taken. After the nth sample, the signal is reconstructed and displayed on a new time-scale. The benefit of this method is that it is not bound to the Nyquist criterion and permits accurate reconstruction of fast-rising impulse-like transients. A description of sequential sampling is given in Figure 2.15 (b).

Some of the sampling devices used in [13] include: The HP Agilent 54750A, Yokogawa DLM2052, ReAl-Time Transient Analyser (RATTY) and Real-Time Analyser (RTA). RATTY and RTA are direct sampling equipment designed for RFI measurements. RATTY has two operating bands: the first band operates up to 800 MHz and the other from 800 MHz to 1.4 GHz. The RTA has four operating bands within DC to 2.7 GHz. The currently proposed RTA3 for SKA covers a huge frequency spectrum and can operate beyond 2.7 GHz. This RTA3 can be used with the optimized IRA as well as the commercial 2.5 kV fast pulser for TD measurements.

For actual measurement in an open area such as the Karoo, the terrain can affect the measured data. This is a propagation related problem and it is important that we briefly highlight its effects on the radiation of the IRA. It is presented as the last section of this

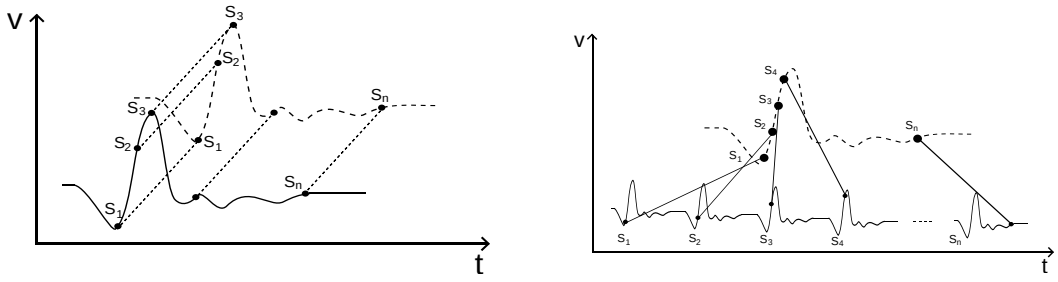

Figure 2.15: (a) Illustration of real-time sampling with the reconstructed signal (b) Sequential sampling of a sampling oscilloscope with the reconstructed signal [60].

chapter.

2.7 Effects of the Terrain on IRA Radiation

In most field measurements there will be an imperfectly conducting earth (soil) in the vicinity of the antenna which will modify the EM field at a distant observation point (see Figure 2.16). Therefore, the effects of the soil on the IRA's radiated field cannot be neglected. Through path R_1 (Figure 2.16) there is a direct wave travelling from the antenna to the distant observer. Also, through path R_2 there is a wave that leaves the antenna at a different angle and is reflected off the ground to the observation point. Besides these *space waves*, there is a *surface wave* on the earth which also contributes to the total field at the observer's location. Thus, the modified field becomes a complicated function of the antenna and observer heights h_1 and h_2, the distance d, the soil parameters σ and ε_r, and the directional radiation characteristics of the IRA. Using the geometry of Figure 2.16 and applying Snell's law – angle of incidence equals angle of reflection, we have:

$$\psi = \tan\left(\frac{h_1 + h_2}{d}\right) \tag{2.32}$$

where the two distances R_1 and R_2 are expressed as

$$R_1 = d\left[\left(\frac{h_1 - h_2}{d}\right)^2 + 1\right]^{1/2} \text{ and } R_2 = d\left[\left(\frac{h_1 + h_2}{d}\right)^2 + 1\right]^{1/2} \tag{2.33}$$

The total E-field of the IRA in the presence of the lossy earth is given by equation (2.34) which is extracted from [61]. The first, second and third term in this equation represents the direct, reflected and surface wave components, respectively.

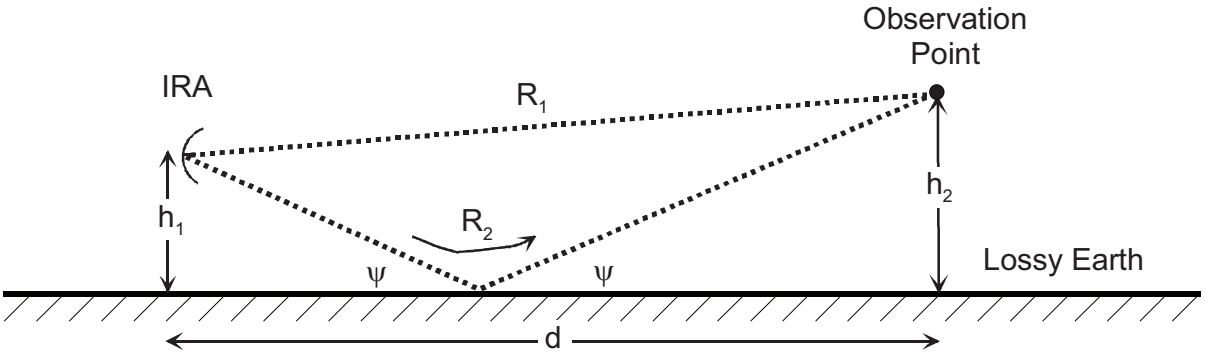

Figure 2.16: Schematic diagram of the IRA located over lossy earth.

$$\frac{E}{E_0} \cong 1 + Re^{-j\Delta\phi} + (1-R)Ae^{-j\Delta\phi} \tag{2.34}$$

where R is the Fresnel reflection coefficient for vertical or horizontal polarization and given by the following equations:

$$R_v(\psi, f) = \frac{\varepsilon_r\left(1+\frac{\sigma}{j\omega\varepsilon}\right)\sin\psi - \left[\varepsilon_r\left(1+\frac{\sigma}{j\omega\varepsilon}\right) - \cos^2\psi\right]^{1/2}}{\varepsilon_r\left(1+\frac{\sigma}{j\omega\varepsilon}\right)\sin\psi + \left[\varepsilon_r\left(1+\frac{\sigma}{j\omega\varepsilon}\right) - \cos^2\psi\right]^{1/2}} \tag{2.35}$$

for the case of vertically polarised E-field, and

$$R_h(\psi, f) = \frac{\sin\psi_2 - \sqrt{\varepsilon_r\left(1+\frac{\sigma}{j\omega\varepsilon_r\varepsilon_0}\right) - \cos^2\psi_2}}{\sin\psi_2 + \sqrt{\varepsilon_r\left(1+\frac{\sigma}{j\omega\varepsilon_r\varepsilon_0}\right) - \cos^2\psi_2}} \tag{2.36}$$

for horizontal polarization, where $\omega = 2\pi f$ is the angular frequency, σ and ε_r are the soil's electrical parameters, conductivity and permittivity, respectively. The surface wave contribution for vertical and horizontal polarizations slightly differ, such that there are different attenuation functions A for vertically and horizontally polarized fields. This attenuation function has the general form

$$A(v) = \left[1 - j\sqrt{v\pi}e^{-v}erfc(j\sqrt{v})\right] \tag{2.37}$$

where the quantity v is expressed as:

$$v = -j\frac{\omega}{c}zu^2\frac{1-u^2\cos^2(\psi)}{2}\left[1+\frac{\sin(\psi)}{u\sqrt{1-u^2\cos^2(\psi)}}\right]^2 \text{ vertical pol.} \tag{2.38}$$

$$v = -j\frac{\omega}{c}zu^2\frac{1-u^2\cos^2(\psi)}{2}\left[1+\frac{u\sin(\psi)}{\sqrt{1-u^2\cos^2(\psi)}}\right]^2 \text{ horizontal pol.} \tag{2.39}$$

where c is the speed of light and z is the range of the observation point from the IRA. The term u contains useful information about the lossy earth and is given by the following equation.

$$u = \sqrt{\frac{1}{\varepsilon_r - j(\sigma/(\omega\varepsilon_0))}} \tag{2.40}$$

Lastly, the phase factor $\Delta\phi$ is a function of the path differences, given by the expression

$$\Delta\phi = \frac{\omega}{c}(R_2 - R_1) = \frac{\omega d}{c}\left\{\left[\left(\frac{h_1+h_2}{d}\right)^2+1\right]^{1/2} - \left[\left(\frac{h_1-h_2}{d}\right)^2+1\right]^{1/2}\right\} \tag{2.41}$$

During on-site propagation measurements the radiated field from the IRA can be influenced by the terrain or Karoo soil. Hence, these equations provide very useful information that can be used during measurement and data analysis for accurate evaluation of results.

2.8 Summary

This chapter has laid the groundwork upon which the specific details of this research can be fully established and discussed in the subsequent chapters. The field of electromagnetic waves has been reviewed so as to understand antennas, especially hyper-band (HB) antennas, as advanced technology and not *mysterious and darkest of black magic* as perceived by some engineers. Impulse radiating antenna (IRA) is introduced as an HB antenna with its main components that can be considered for optimization. The parameters used to develop the geometrical structure of IRA have been described and will be frequently referenced later in chapters 3 and 5. Two commonly known domains (time and frequency domains) in which the trifilar coupled-line balun and the IRA are characterised have been

presented. A review on the original design (s) of IRA with particular interest on the feed is important for better comparison with the new and optimised feed for IRA. The following chapter is replete of early design concepts of IRA and extended antenna (IRA) properties that have not been described in the concluded chapter.

—The energy in electro-magnetic phenomena is mechanical energy. The only question is, Where does it reside? On the old theories it resides in.....On our theory it resides in the electromagnetic field, in the space surrounding the electrified and magnetic bodies, as well as in those bodies themselves..... —

—James Clerk Maxwell, 1865 —

CHAPTER 3

The Original IRA Designs

The geometrical structure of an IRA makes it a very special antenna that radiates impulse-like fields as an aperture and hyper-band (HB) directional antenna. The electric field distribution over the aperture determines the nature of radiation in the far-field. In many cases the need to maximise the radiated fields has been of primary concern. Various studies have been done on the conical TEM feed structure to improve the performance of IRA in this regard. However, since IRA is an HB antenna the key challenge is to have a balanced feed system (*balun*) so as to properly match the feed impedance of IRA to a source impedance. Therefore, the design and availability of such a system influences the geometry of the conical plates (characteristic impedance) and current distribution on the antenna structure.

Detailed discussions on impedance matching of the feed through a novel balun design are entailed in chapters 4 and 5. Chapter 4 specifically describes the new design of the balun and how it is optimised for the IRA. In chapter 5, the designed balun is used to improve the aperture far-field uniformity.

However, in this chapter the early design configurations of the TEM feed, their polarization geometries, cable feed topologies and characterization of the original IRA, which was built at our engineering department, are discussed. The chapter explains how these aspects have been (and can be) considered in improving the feed of the original IRA.

3.1 The TEM Feed Structure of IRA

The TEM feed lines transmit spherical waves from the feed point to the reflector where they are converted to radiation fields 'visualised' as propagating plane waves in the far-field of IRA. Thus, it is natural to assume or regard such fields as plane waves in the near-field of a receiving antenna. Polarization of these waves depend on the configuration of the conical transmission lines. So before different options of the feed-networks are considered, polarization of the radiated fields are described. Also, it simplifies the discussions on polarization of the field in a single or dual pair feed arm geometries in subsection 3.1.1.

Polarization of Plane Waves

From equation (2.18) in section 2.5, the radiated field has both x– and y– components. This implies that the two E-field components, E_x and E_y, are polarized in the x and y directions, respectively. Assuming a positive z–direction of propagation, the x–y plane with E-field polarization vectors is orthogonal to this direction [16]. Polarization makes it possible to perform simultaneous modulation on both x– and y– polarized signals at a particular frequency. In general, any pair of signals which are orthogonally polarized can be modulated as stated above.

In a transmitting–receiving antenna set-up, the signals in both polarizations can be radiated and received without mutual interference if one of the fields (say E_x) is treated as the desired (co-polarized) field whereas the other orthogonal field (E_y) as the unwanted (cross-polarized) field. This is achieved by exciting only the desired (E_x) field in a transmitting antenna. However, when E_y field is driven, it is referred to as the co-polarized and the E_x field as the cross-polarized field. The isolation (ratio of co-polarized to cross-polarized) is the same in both cases for a similar dual-polarized antenna (reciprocity principle) [16].

The (E_x) and (E_y) are said to be linearly polarized because their direction in their respective axes are constant with respect to the direction of propagation in the z–axis. Usually, linear polarizations are either *horizontal* or *vertical* [62]. A horizontal polarization is described by the orientation of its E-field being parallel relative to the ground [16]. The mathematical expression of this description is given as:

$$\hat{co} \perp \hat{n} \perp \hat{z} \tag{3.1}$$

where $\hat{co}$ is a co-polar unit vector parallel to the E-field of horizontal polarization, $\hat{n}$ is a normal unit vector to the ground and $\hat{z}$ is a unit vector in the z–direction. On the

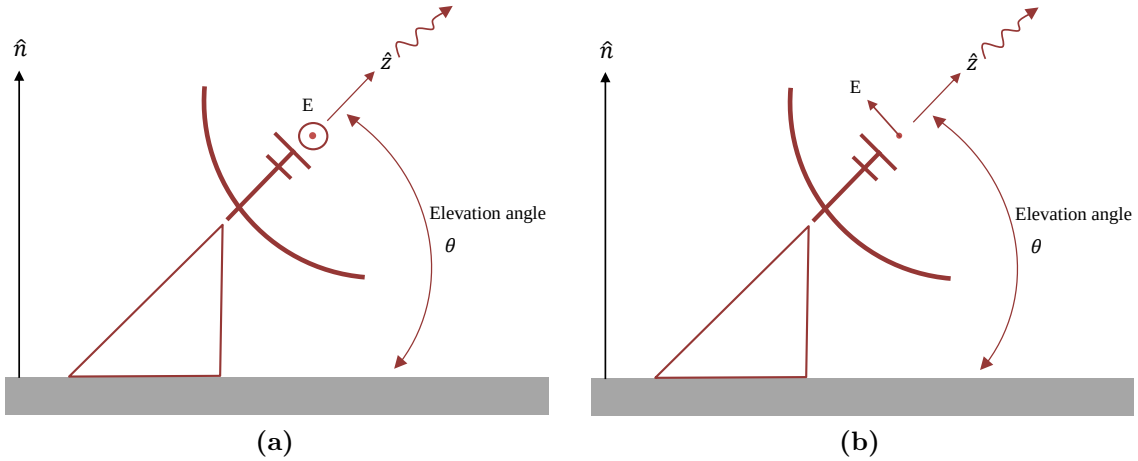

Figure 3.1: (a) E-field into paper showing horizontal polarization with the antenna elevated at an angle θ from the horizon (b) Vertically polarized E-field of an antenna whose elevation angle θ is relative to the horizon.

other hand, it is not necessary for a vertical polarization to have its E-field orientation perpendicular to the ground. In other words, it is not a requirement that $\hat{co}$ is parallel to $\hat{n}$ ($\hat{co} = \hat{n}$), but instead, it lies in the $\hat{z}$–$\hat{n}$ plane. This allows the liberty to also describe waves whose z–direction (refer to Figure 3.1) is not parallel to ground, as horizontally or vertically polarized. While most engineers put more effort to design antennas that operate at particular polarizations, the cross-polar effects are inherent due to changes in the antenna symmetry as a result of movements or some mechanical strain. Consequently, it is desirable to describe the radiation pattern of an antenna in terms of the co– and cross–polar radiation patterns to give a complete picture of the performance of a particular antenna. A proper isolation is required, i.e., co-polar is much greater than the cross-polar components, for optimal radiation.

3.1.1 Dual–Polarization Geometry

We apply the concept of symmetry in the geometry of the feed structure with the aim of describing the feed impedances and polarization in a single and dual pair of feed arms of the IRA. The idea of symmetry is deeply rooted in the human culture since antiquity. It has been applied in electromagnetics where the duality and reciprocity theorems are used to break down complex electromagnetic problems (Maxwell's equations) [63]. In addition, its use extends to geometric symmetries where rotation, similarity, translation and reflection become important mathematical tools in simplifying the geometry. It suffices to say that the combination of the two concepts (symmetry/geometry) with engineering has over the years been beneficial and is the backbone of contemporary antenna engineering [63].

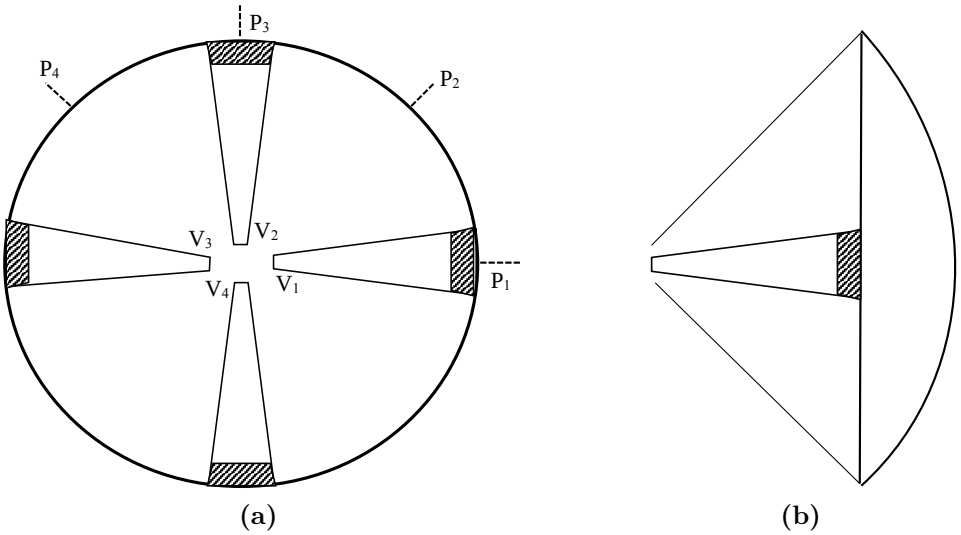

Figure 3.2: A sketch of dual polarized IRA antenna with face-on conical plates (a) Front view (b) Side view.

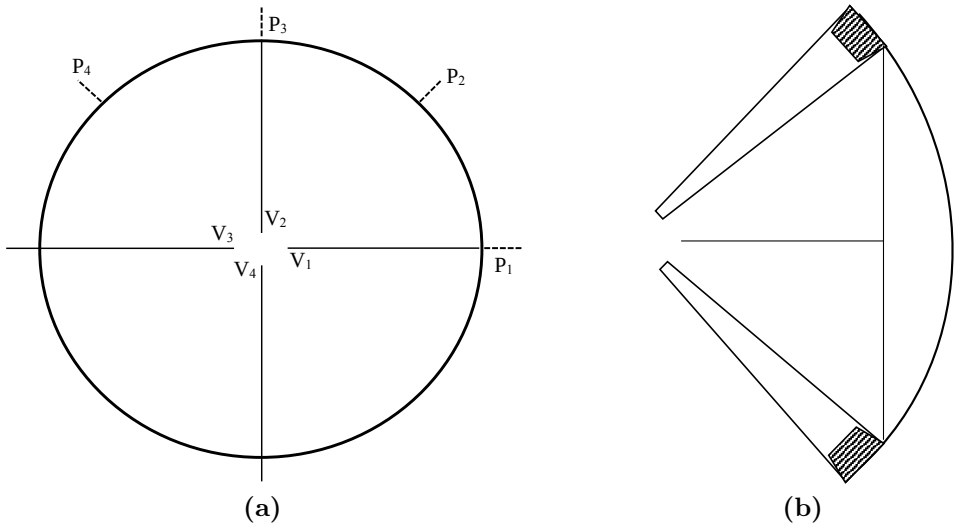

Figure 3.3: A sketch of dual polarized IRA antenna with edge-on conical plates (a) Front view (b) Side view.

Figures 3.2 and 3.3, respectively, show a four arm IRA with face-on and edge-on conical plates. A four-fold rotation axis is considered with each axis of the symmetry plane marked as P_1 through to P_4, in an anticlockwise direction. The conical plates have been labelled as V_1 through to V_4, also in an anticlockwise direction. It is possible to launch TEM waves on each pair of arms independently and simultaneously. For instance, assuming one is interested in launching a horizontally polarized E-field (perpendicular to P_3), then one can consider the axis of plates 1 and 3 in alignment with P_1 and set V_1 = -V_3 with $V_2 = V_4 =$ 0. Similarly, exciting arms 2 and 4 generates a vertically polarized E-field (perpendicular to P_1).

The orientation of the feed arms in Figure 3.2 is such that the base of the conical plate is aligned with the edge of the reflector. This type of configuration increases aperture blockage and scattering as the EM waves travel away from the reflector [64]. For higher frequencies, however, optical approximations can be made to remove the rays blocked by the feed structure. A rotation of the launcher plates such that their longer edges are in parallel to (align with) P_1 and P_3 (refer to Figure 3.3) usually eradicate aperture blockage under similar optics. However, for lower frequency components, depending on the size of the plates, reorienting the feed arms as in Figure 3.3 may be inconsequential [64].

A calculation of the impedances can be performed by letting Z_1 be the characteristic impedance linked to each feed for either P_1 or P_3 polarization. The impedances are expected to be approximately the same for both configurations in Figures 3.2 and 3.3. Due to the orthogonality relationship of the electric fields, impedance calculation of the plates on P_1 is not affected by that of the P_3 plates. Considering an E-field launched parallel to P_1, with the current treated as positive into the conical plates, this gives:

$$\begin{aligned} V_1 = -V_3 = V \quad &, \quad I_1 = -I_3 = I \\ V_2 = -V_4 = 0 \quad &, \quad I_2 = I_4 = 0 \\ Z_1 \equiv \frac{V_1 - V_3}{I_1} &= \frac{2V}{I} \end{aligned} \tag{3.2}$$

Assuming $Z_1 = 300\ \Omega$ and the E-field is now driven parallel to P_3, the same value of impedance is obtained (300 Ω). As stated earlier, the symmetry and hence orthogonal polarizations grant us the flexibility to initiate independent excitations on both pairs of feed arms without mutual interference. The following mathematical formulation presents a scenario where both pairs are driven equally (electrically in parallel):

$$\begin{aligned} V_1 = V_2 = -V_3 = -V_4 = V \quad &, \quad I_1 = I_2 = -I_3 = -I_4 = I \\ Z_2 \equiv \frac{V_1 - V_3}{I_1 + I_3} = \frac{V_2 - V_4}{I_1 + I_3} &= \frac{2V}{2I} = \frac{V}{I} \\ Z_2 &= \frac{Z_1}{2} \end{aligned} \tag{3.3}$$

From equation (3.3), it is easily noted that the impedance, Z_2, is half the impedance Z_1,

i.e., Z_2 is 150 Ω if Z_1 is 300 Ω. This relationship is very important in determining the feed impedance of a four-arm IRA once the characteristic impedance of the conical plates has been calculated through stereographic projection and conformal mapping [42, 65], (revert to subsection 2.5.2). The contribution of the fields in this dual polarized IRA is equal (and perpendicular) on the symmetry axis yielding a polarized E-field that is aligned to P_2. Therefore, a pair combination of 1/2 and 3/4 plates yield P_2 polarization whereas a combination of 2/3 and 1/4 plates yield the orthogonal polarization, aligned to P_4.

After the geometrical illustrations given in this subsection, the cardinal question is whether or not a four-arm IRA is a better configuration over a two-arm IRA in terms of feed impedances, polarization and radiated fields. First off, there is a great advantage with a four-arm IRA where the input impedance is reduced by a factor of 2. This is an important point to consider for proper matching of an antenna impedance to a source impedance, bearing in mind that a typical source impedance is lower than that of an antenna. Secondly, there is dual polarization associated with a four-arm IRA. On the other hand, lowering feed impedance contributes to feed blockage (wider plates) hence reduced radiation. Thus, a good trade-off is required between low input impedance and least possible feed blockage. It was previously presumed but later confirmed that an input impedance of 400 Ω for a single pair of feed arms (essentially 200 Ω for dual pair of feed arms) represents a good compromise [66]. Further studies through numerical calculations and geometrical optics analysis show that a 200–Ω case for a four-arm IRA has better aperture efficiency with φ_0 set to 60° [43, 44].

3.1.2 Cable Feed Topologies

There are different types of cables available in various sizes and mechanical design and can be found in most places around the world. As might be expected, a cable network is commonly used in IRA antennas. They provide the flexibility required in making electrical connections between the feed of the IRA and the excitation source. In the previous subsection we discussed how to drive single and dual TEM feeds for different polarizations. In this subsection, Figures 3.4 and 3.5 are used as illustrative examples where cable configurations have been added to achieve a specific feed impedance and polarization.

In Figure 3.4, a feed characteristic impedance of 400 ohm is considered, suitable for horizontal (P_1) and vertical (P_3) polarizations in Figures 3.2 or 3.3. Assuming a P_1 polarization, then 100 ohm coaxial cables are fixed as part of the conical plates 1 and 3 with two similar cables routed through the axial symmetry. A pair of these cables

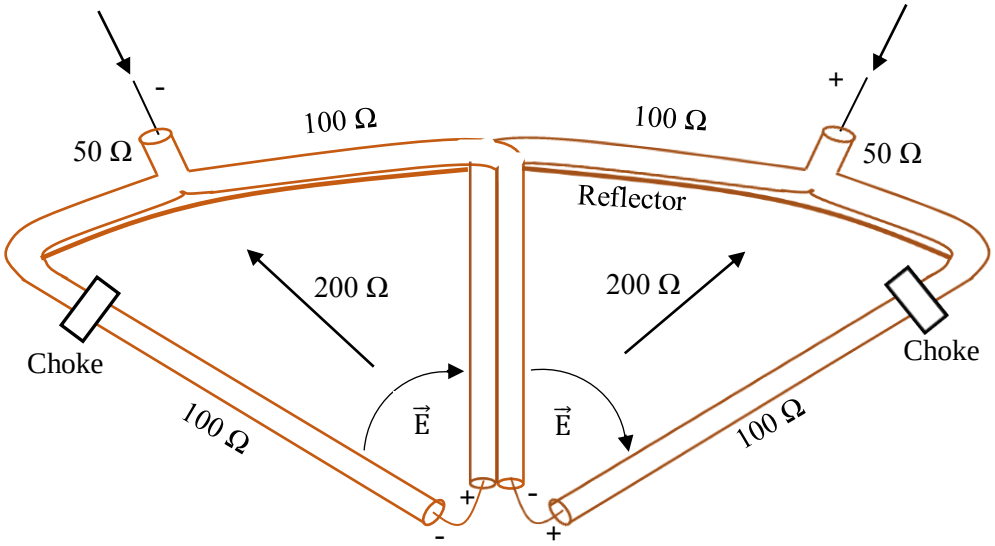

Figure 3.4: Cable configuration for a differential feed impedance of 400 Ω with cables connected to a differential source of 100 Ω, following [64].

are connected at the feed gap around the apex, resulting in a differential impedance of 200 ohm on each half of the dish. The addition of the impedances from the two halves of the reflector gives the required 400 ohm differential impedance. At the back of the dish the (-) cables are connected in parallel (with the same electrical length to the feed gap) into a 50 ohm cable. Similar connections and electrical lengths are made for the (+) cables. Both the (-) and (+) 50 ohm cables create a 100 ohm differential source. A P_3 polarization can be achieved by using the same 100 ohm differential drive. The disadvantage of this type of configuration is that the cables run along the conical plates and hence affect the impedances at the plate-reflector terminations [64]. This obviously leads to common-mode currents and the use of expensive chokes to minimise the EM interference effects. Furthermore, it is not possible to use it together with a single-ended pulser.

Figure 3.5, however, presents a cable feed option which can be used with a single-ended system but still does not eliminate the problem of common-mode currents and the requirement of high-quality chokes. The IRA-6 presented in Figure 3.7 (a) shows this type of cable feed configuration with a single-ended splitter and ferrite beads (chokes) around the feeding cables [11]. This particular cable feed topology is suitable for P_2 and P_4 polarizations as described in subsection 3.1.1. For a 200 ohm feed impedance, a 100 ohm coaxial cable is made part of, e.g., plate 4 and a similar cable is run through the axial symmetry. Having 100 ohm for each half of the dish, leads to two single-ended gaps around the apex region. At the back of the dish the two cables are connected (with the same electrical length to the apex) in parallel to a (+) 50 ohm cable, single-source excitation.

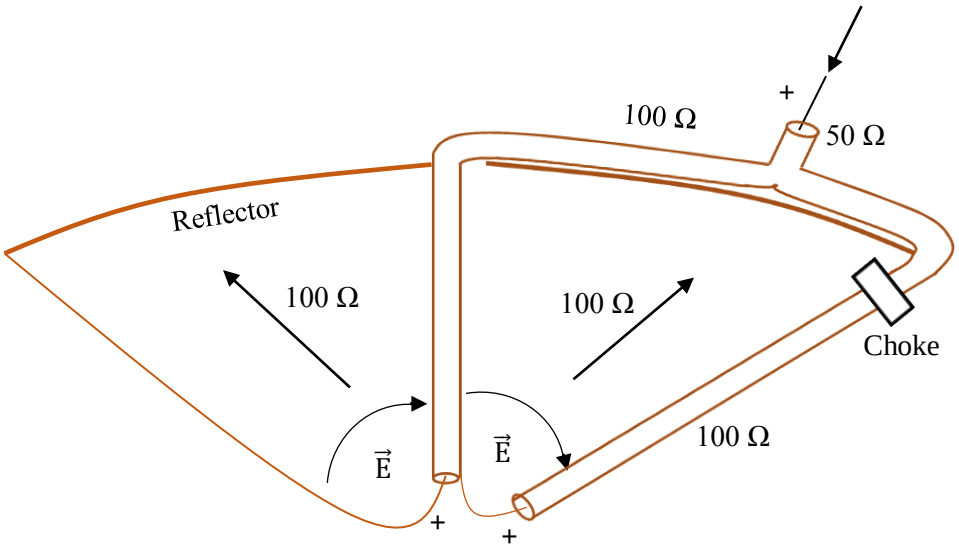

Figure 3.5: Cable topology for a 200 Ω feed impedance operated by a single source of 50 Ω impedance, following [64].

When the plates are joined in pairs at the feed gap, dual polarizations for P_2 and P_4 can be produced independently. However, it is possible to design a cable feed configuration which can be used with special transformers placed at the feed point to generate both P_2 and P_4 polarizations concurrently [64]. This section has explored a typical TEM feed structure with regards to symmetry, geometry, impedances, polarization and cable feed networks. There are other possibilities discussed in [64, 43, 67], for the IRA feeds including the half-impulse radiating antenna (HIRA) which also requires an impedance transformer for impedance matching [68]. The original IRA with the single-ended cable feed topology is characterised in the following section 3.2.

3.2 Characterization of the Original IRA Design

Table 3.1 shows both the conical TEM and the equivalent longitudinal structure parameters (computed as in subsection 2.5.2) for the first Stellenbosch IRA in Figure 3.8. Cable

Table 3.1: Design parameters for the original IRA in Figure 3.8. The other parameters include F/D ratio of 0.38 and Z_{line} of 150 Ω.

Parameter	Value (mm)	Parameter	Value (°)
Diameter, D	850	β_0	52.77
a	340	β_1	39.42
b_1	245.50	β_2	68.98
b_2	470.80	φ_0	60

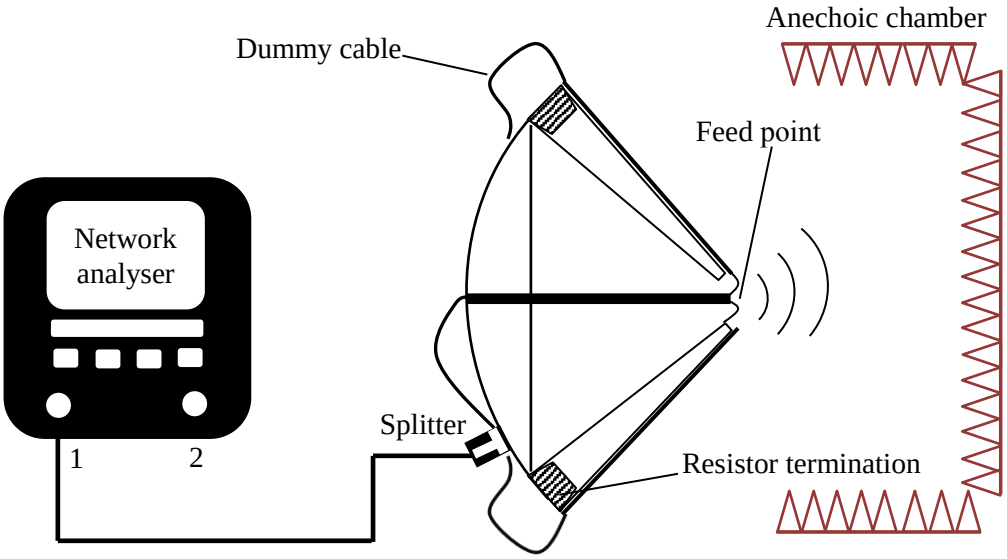

Figure 3.6: Experimental set-up for time and frequency domain characterization of the original design of the IRA in [13].

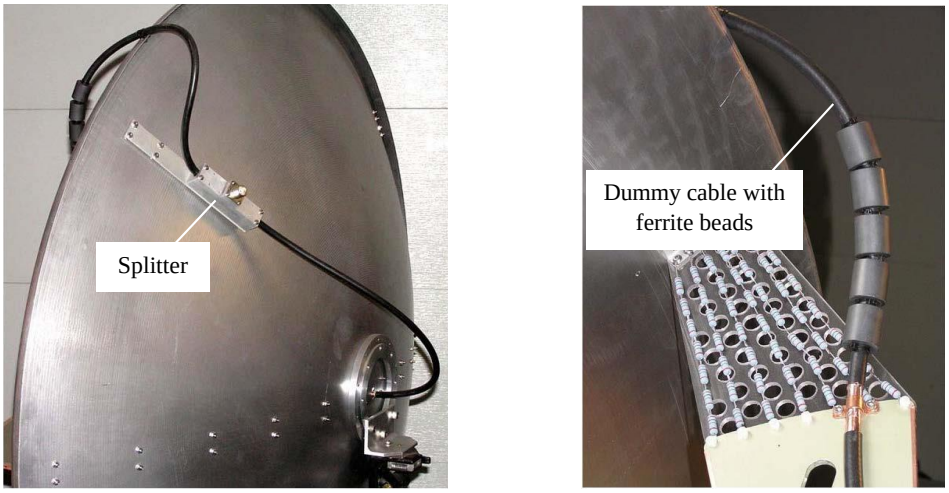

(a) **(b)**

Figure 3.7: IRA-6 with (a) A splitter fixed at the back side of the reflector and (b) Dummy cable with five ferrite beads [11].

topology for this 150 Ω conical plate-fed IRA follows the design in Figure 3.5 or the IRA-6 in Figure 3.7 (a). The connection of the cables at the back of the reflector form a T–junction and quintessentially three-port network resistive divider (Figure 3.6). Although the divider (splitter) is chosen because of its easy design and large bandwidth, it is normally lossy due to lumped-element resistors [19], and therefore, a critical area to be considered during IRA optimization. Two 75 Ω (LMR400-75) cables of 818 mm in length are used to make electrical connections between the splitter (behind the reflector) and the plates at the feed-point. The feed-arms are made out of double sided FR4–PCB boards each

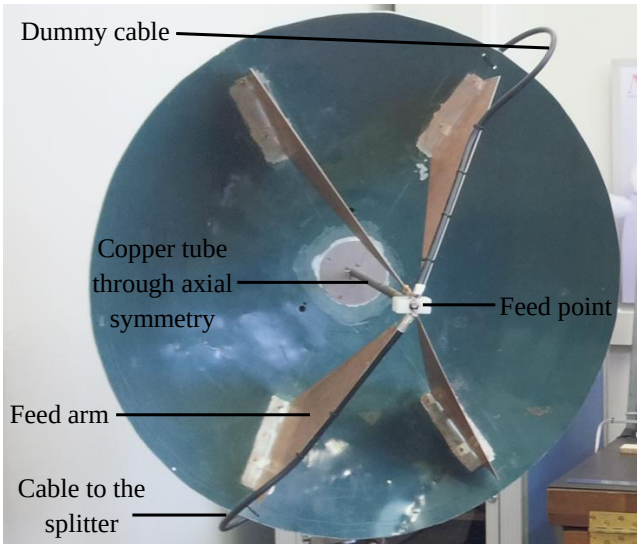

Figure 3.8: The original IRA design [13], at our department in Stellenbosch University.

terminated with eight 1.2 kΩ surface-mount resistors in parallel (effectively 150 Ω) on the reflector.

A copper tube of diameter 15 mm is fixed at the centre of the dish through to the focal point of the dish for mechanical support of the plates (Figure 3.8). The cable through the symmetry axis passes through the tube and at the feed gap its centre conductor is soldered to the top two plates while its sheath is attached to the metallic tube (ground). The second cable is routed along one of the bottom feed arms where its sheath is connected to the two joined bottom plates while its centre conductor is soldered on the tube (ground) at the feed point. A dummy cable is attached to the opposite plate as shown in Figures 3.6 and 3.8, aiming for a balanced feed system. The use of a dummy cable is also shown in Figure 3.7) (b) [11]. The original IRA in Figure 3.8 is measured in an anechoic chamber as follows.

3.2.1 Anechoic Chamber Measurement

With port 1 of a two-port PNA-X vector network analyser (VNA), frequency domain reflection coefficient measurement is carried out in an anechoic chamber and time domain response determined. A simple diagram showing the experimental set-up is given in Figure 3.6. An electronic calibration is performed in port 1 and thereafter connected to the antenna for reflection co-efficient, S_{11}, and time low-pass analysis. A full TD response of IRA is plotted in Figure 3.9 over a time frame of -1 to 12 nanosecond (ns). The three regions with dominant spikes are associated with reflections from the splitter, the feed point and the reflector. With TD analysis it is easier to identify areas of discontinuities along the

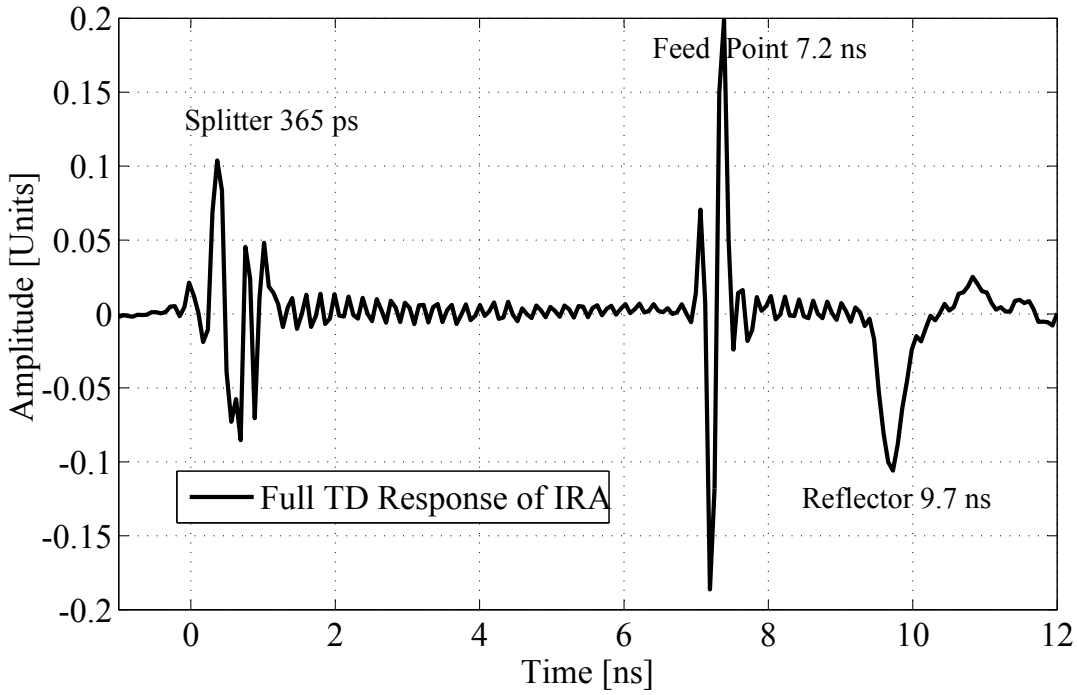

Figure 3.9: Measured full TD response of the first Stellenbosch IRA with sharp spikes at the splitter (365 ps), feed point (7.2 ns) and the reflector (9.7 ns).

signal path and effectively implement time gating on specific area(s) for various analysis in FD. The PNA-X VNA display window can be split/ tiled into two separate windows to operate both TD and FD plots simultaneously. If time gating (notch filter) is applied on, e.g., the splitter region, one is able to view the effect on the FD plot immediately.

Mathematical evaluation of different time reflections of the signal along its path is a vital process towards the verification of the experimental data. Various mathematical formulations provide rough estimates of the time the signal takes to travel from one electrical component to another depending on the characteristics of the material. It is generally accepted that the distance travelled by EM wave in free space is 0.3 metres per nanosecond or equivalently 3.3333 ns.m^{-1}. For the LMR400 cable with velocity of propagation, V_p, of 0.85 the time taken per unit length by the signal through the cable is given as:

$$t_c = \frac{3.3333}{V_p} \approx 3.9215 \quad ns.m^{-1} \tag{3.4}$$

Since the cable length used is 818 mm, the full time travelled by the pulse from the splitter–LMR400 connection point to the feed point is approximately:

$$t_{sc} = 3.9215\ ns.m^{-1} \times 0.818\ m \approx 3.2078 \quad ns \tag{3.5}$$

The splitter is composed of microstrip lines and a substrate of dielectric constant, ϵ_r, of 3.55. Thus, equation (3.6) can be applied to calculate the time it takes the signal to propagate in a unit length of the material.

$$t_s = 3.3333\sqrt{\epsilon_r} \approx 6.2804 \quad ns.m^{-1} \tag{3.6}$$

The length of the 50 Ω line, l_{50}, is 13.6 mm while that of the 75 Ω line, l_{75}, is 14.2 mm. Therefore, the time taken through the resistive divider is:

$$t_{splitter} = [(l_{50} + l_{75})\ 6.2804\ ns.m^{-1}] + t_x \approx 174.6\ ps + t_x \tag{3.7}$$

where t_x accounts for mismatches within the connectors and resistors. The time travelled by the signal through the splitter to the feed point is obtained by the addition of equations (3.5) and (3.7).

$$t_{feed} = 3.2078\ ns + 174.6\ ps + t_x \approx 3.3824\ ns + t_x \tag{3.8}$$

Finally, the time of the signal from the focal point to the reflector is computed as 3.3333 ns.m^{-1} multiplied by the distance covered, 416 mm, to have 1.3867 ns. Hence, the total time it takes the signal to travel from the splitter to the dish is calculated as:

$$t_{reflector} = 1.3867 + 3.3824 + t_x \approx 4.7691\ ns + t_x \tag{3.9}$$

Equations (3.7)–(3.9) are used to estimate reflections from the splitter, feed point and the reflector. The value for t_x can be omitted if it is very small. In each of the reflections a return path must be included, hence the values are doubled to obtain reflections at 349 ps (splitter), 6.8 ns (feed point) and 9.5 ns (dish). Table 3.2 shows that the calculated values

Table 3.2: Comparison between the measured and calculated values for the reflections from the splitter, feed point and the reflector of the original IRA.

	Splitter (ps)	Feed point (ns)	Reflector (ns)
Measured value	365	7.2	9.7
Calculated value	349	6.8	9.5

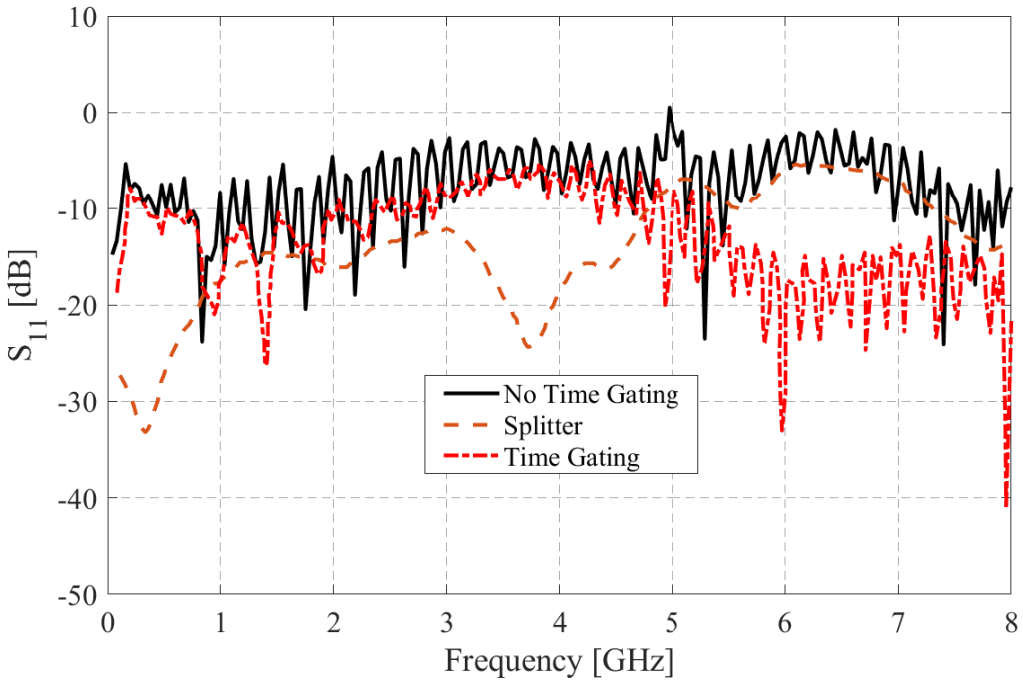

Figure 3.10: Measured S_{11} of the first Stellenbosch IRA in FD with and without the splitter time gated or filtered out.

are comparable to the measured values in Figure 3.9. The marginal difference between the measured and calculated values is on account of the fact that the actual value of t_x has been ignored in the estimation of the computed values.

Figure 3.10 shows the comparison between the measured S_{11} of IRA with all the components intact and when the splitter is time gated. The S_{11} of the Stellenbosch IRA (no time gating) is above the standard value of -10 dB across the entire frequency range; for improved performance the S_{11} need to be minimised below the typical value -10 dB. When the splitter is time-gated, there is an improvement on the measured values of S_{11} especially on the higher frequencies above 5 GHz. The splitter's optimal performance is up to 5 GHz and the poor S_{11} within this frequency range is primarily attributed to the antenna itself (field blockage due to launcher plates).

However, for frequencies greater than 5 GHz there are two inferences made: (i) The splitter worsens the performance of IRA and (ii) Optical effects dominate (minimised feed blockage) hence better S_{11}. There is need to solve these two issues and our approach is to design a new hyper-band (HB) balun and improve on the design of the plates to reduce potential feed blockages. The new HB balun and the improved launcher plates are described in detail in chapters 4 and 5, respectively. In subsection 3.2.2, further analysis of the original IRA design is performed using simulation work. It is easier to vary a parameter in the simulation model than changing it in the actual original IRA, hence the advantage of

using simulation. The relationship between φ_0 and Z_{line} is discussed including the ratio b_1/a.

3.2.2 Simulation: CEM Model of the Original IRA

An exact computational electromagnetic (CEM) model of the original IRA is constructed in FEKO with the same parameters in Table 3.1. Figures 3.11 (a) and (b) show the FEKO model when φ_0 is set to 60° and 45°, respectively. The purpose of this simulation is to determine whether a combination of $\varphi_0 = 60°$ and $Z_{line} = 150\ \Omega$ as chosen for the original IRA is a better impedance match to the source impedance. Numerical predictions in [43], show that the above combination requires the ratio $b_1/a \approx 0.59$ for a better match (or right size of plate width). However, the calculated value of b_1/a from Table 3.1 is 0.72 (> 0.59). There is an inverse relationship between b_1/a and the feed-arm angle, φ_0, for a constant Z_{line} [43]. Consequently, for $b_1/a = 0.72$ the new value of φ_0 must be less than 60° and from the numerical analysis in [43], it is 45°.

The comparison of the S_{11} simulated results for different feed-arm angles is shown in Figure 3.12 with Z_{line} set to 150 Ω. As expected there is better response of the antenna (S_{11}) when $\varphi_0 = 45°$ in comparison to $\varphi_0 = 60°$, for constant $Z_{line} = 150\ \Omega$. Following the computational analysis of a four-arm IRA [43], varying the plate size (b_1/a) directly changes the feed impedance, Z_{line}. This provides an alternative approach of tackling the problem. Since $\varphi_0 = 60°$ is preferred for low cross-polarized fields, it can be kept constant and only adjust Z_{line} ($> 150\ \Omega$) for increased values of b_1/a. In fact, this value is proposed as 200 Ω when $\varphi_0 = 60°$ for a properly matched and better performance of IRA (refer to subsections 2.5.2 and 3.1.1). This means that with appropriate values of φ_0, b_1/a and Z_{line}, it is possible to design thinner plates for the IRA which can minimise potential feed blockage. However, to obtain uniform aperture fields (even current distribution) with the IRA, a balun is required. Thus, the main objective is to design one for the IRA and through this chapter we have identified the requirements for the new balun as highlighted in the subsequent subsection.

3.2.3 Requirement for the Trifilar Coupled-line Balun

Through the analysis and synthesis of various subsections of this chapter, the following requirements are identified for the new and optimised trifilar balun in chapter 4:

- Due to the hyper-band (HB) nature of the IRA, the balun must have HB characteristics, where the fractional bandwidth is greater than 1.634.

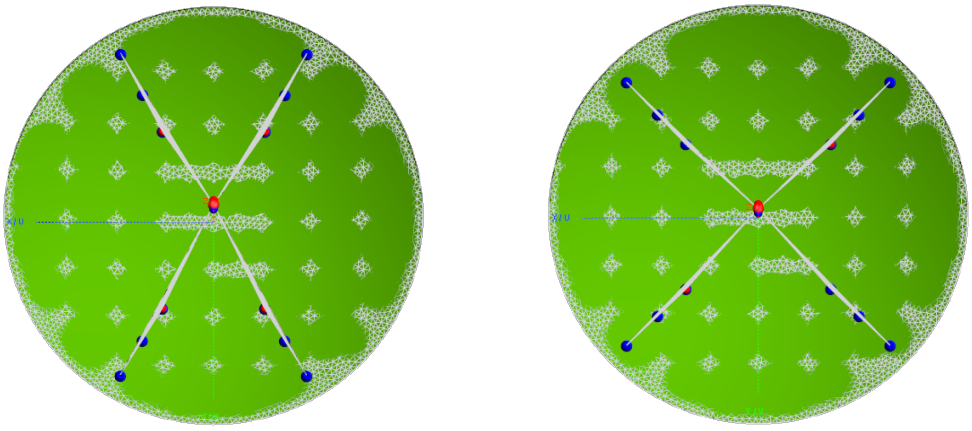

(a) (b)

Figure 3.11: Computational electromagnetic (CEM) model of the original IRA design with (a) $\varphi_0 = 60°$ and (b) $\varphi_0 = 45°$.

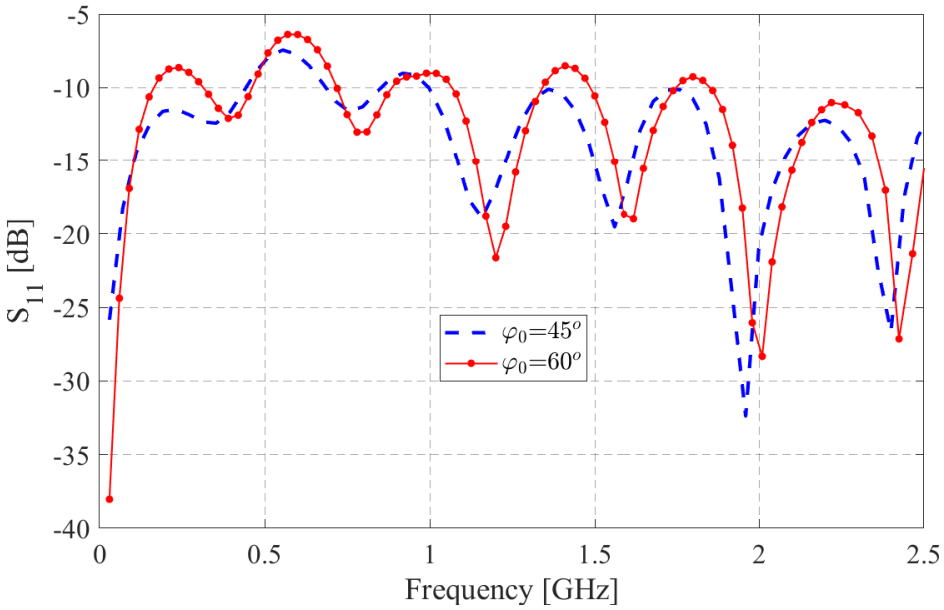

Figure 3.12: Comparison of the S_{11} simulated results for different feed-arm angles: $\varphi_0 = 45°$ and $\varphi_0 = 60°$.

- Symmetric aperture: a balun that ensures balanced currents on the IRA structure for uniform aperture fields and better response of S_{11} of the IRA over the ultra-wideband frequency.
- A cost effective balun which allows a simple cable topology that eliminates the need of expensive and high impedance feeding cables including the dummy cable and high-quality chokes.
- Made from a material with better frequency properties, e.g., low loss at high frequencies.

3.3 Summary

The original IRA design has been successfully characterized in both time and frequency domain and areas of optimization have been identified. The geometrical symmetry of IRA requires even distribution of currents over the antenna structure for optimal radiation. Discussions on the TEM feed structure, polarization geometry and cable feed topologies allude to the fact that feeding IRA is a critical part in the design phase. The question of *why* this is important has already been addressed in this chapter, but the *what* and *how* will follow in the subsequent chapters.

—Do what you can, with what you have, where you are —

—Theodore Roosevelt —

CHAPTER 4

Trifilar Coupled-line Balun for IRA

This chapter focusses on the design aspect of a new balanced feed for the IRA; to explain the procedures and concepts that are involved and how the final and optimised balun is achieved. Designing a balun for an antenna can be more intricate when compared to designing the antenna itself. There are cases where direct connections have been made between coaxial feed lines and balanced antennas, thereby ignoring some aspect of the connection (a balun). Hitherto we still ponder about the function of baluns, hence the question of whether to include them as part of an antenna system or not. The misconstruction of the relevance of baluns extends to engineers who design them as well. Thus, a brief review on baluns with respect to a dipole antenna has been elaborated in section 4.1.

Microstrip line technology is a well-known transmission-line configuration which has evolved over the years and is widely used in the printed circuit board (PCB) design processes. The layout of a microstrip structure and the existing printed circuit techniques allow an easy fabrication process. In addition, microstrip technology offers an attractive range of impedances and couplings for various applications in PCBs [69].

We discuss the theory of coupled lines and then centre on an edge-coupled structure with three printed conductors for a hyper-band (HB) coupled-line balun for the IRA. The initial model of the trifilar balun is developed in CST and validated using measurement results from a designed prototype as well as simulation results from AWR. Both TD and FD are

used in the analysis of electromagnetic coupling on the coupled lines.

The last section of this chapter presents the final model and the fabricated trifilar coupled-line balun used on the IRA. Various microstrip line parameters and configurations have been considered in an attempt to optimize the balun.

4.1 Review of Baluns

Several commercial-off-the-shelf (COTS) baluns exhibit some form of impedance transformers, perpetuating the misconception that they are just matching devices. The underlying objective of using a balun is to create proper current paths from unbalanced to balanced configurations or vice versa [70, 14]. There are unwanted effects when a balun is not included as part of an antenna system and when a balun using a coupling transformer is connected to an antenna. Usually, this leads to significant errors in measuring antenna's terminal impedance and Standing Wave Ratio (SWR). There are two subsections in this section, with the first subsection describing the unreliability of a transformer-type balun, and the second subsection describing the dependence of SWR on cable length in a direct connection between a coaxial cable and a dipole antenna. Thus, emphasising the need to use a balun in an antenna, particularly a balun which can properly match an antenna.

4.1.1 Reliability of a Transformer-type Balun

Analysis of a transformer-type balun shows that it does not provide true impedance-transfer-ratio (ITR) of the input and output terminals [70]. This is due to losses, leakage reactance and couplings that are below an optimal value. The ITR of this type of a balun becomes worse when connected to an antenna that is reactive when operating in frequencies further away from its frequency of resonance. Such a degraded ITR does not pose significant operational complications. However, measured SWR plots of an antenna with a transformer-type balun show a considerable difference with those of an antenna connected to a choke-type balun or transmission line transformer [71, 52, 72], which are free from ITR error. Therefore, measured antenna impedances will contain undesirable effects (skewed data) when a balun is not connected to an antenna or a transformer-type balun is used [70].

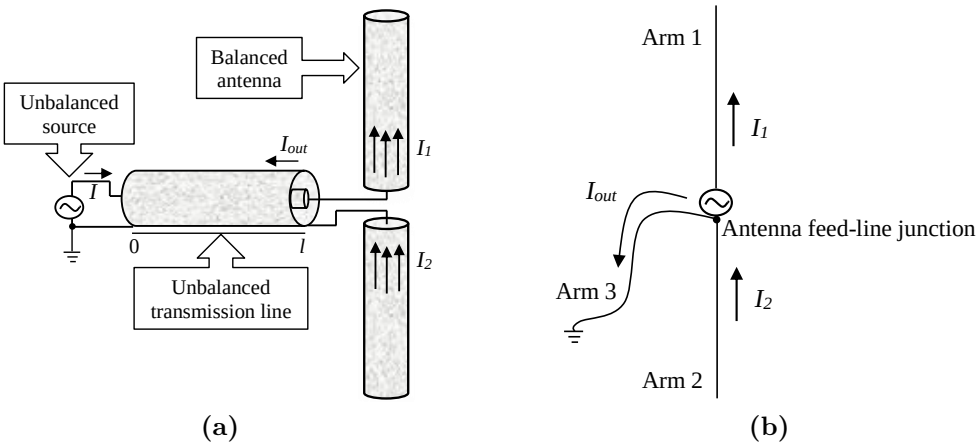

Figure 4.1: (a) Demonstration of current paths in a dipole antenna connected to a source via a coaxial cable (b) A representative sketch of the electrical connection in part (a).

4.1.2 Dependence of SWR on the Line Length

The feed input impedance varies with the cable length when there is a mismatch between the antenna (load) and the cable line. Truncating a section of the feed-line length can yield the required load impedance to match the antenna but this limits the antenna's frequency range of operation. In theory, the SWR does not vary with cable length, besides hardly noticeable changes due to variations in cable attenuation [70]. Thus, a significant change in SWR as the cable length changes is caused by the variation of the load impedance at the end of the line, which is dependent on the cable length. The omission of a balun in a symmetrical antenna that is fed through a coaxial line means that whenever the length of a coaxial line is altered, the load impedance will change, and consequently a change in the SWR. Figure 2.8 (c) is used to analyse this common phenomenon by tracing the current paths at the feed point of the antenna. For convenience, it is reloaded into this section as Figure 4.1 (a) and its corresponding electrical representation is given in Figure 4.1 (b).

The symmetry of the dipole allows equal coupled energy of opposite phase into the cable line, thus nullifying induced charge flow on the outer sheath of the coaxial cable. What is surprising is that there are three routes for the current flow in a coaxial cable feed, bearing in mind that the coaxial line has only two conductors. At RF, both the inner and outer currents flowing on the surface of the coaxial sheath are isolated by the transfer impedance [70]. As a result, there is no interaction between the currents which flow on the inner surface of the conductor and those on the peripheral surface, and vice versa.

The transmission line current, I, refers to both currents flowing on the centre conductor and the inner braid surface. They are of equal magnitude and opposite phase and do not

radiate since their fields reside within the shield of the coaxial cable. Applying Kirchhoff's current law at the dipole feed-line junction, the current flowing on the arm 2 is given as, $I_2 = I + I_{out}$. A large I_{out} results in uneven distribution of currents on both dipole arms and radiated fields from the coaxial line. The outer surface of the sheath essentially becomes a radiating arm 3 in parallel with arm 2. Therefore, the desired radiation pattern from the dipole antenna can severely be distorted by emissions from arm 3; directive antennas are particularly more vulnerable [70, 14]. An equivalent electrical circuit showing the three radiators is shown in Figure 4.1 (b). It should be noted that the magnitude of I_{out} is a function of the impedance to the ground which is linked to the peripheral surface of the cable braid [70]. Consequently, a change in the cable length alters the magnitude of I_{out} since the impedance between arm 2 and the ground varies as well.

In general, with no balun present, varying the cable length varies the length of the antenna (arm 3), thereby affecting the input impedance at the terminal of the cable feed. Thus, the measured SWR at the input of the feed-line changes with the transmission line length when there is no balun to remove I_{out}. For baluns designed with coupling transformers, RF chokes have been used on the coaxial cable feeds to mitigate I_{out}; similar discussion has been presented in the previous chapter. Attaining the balun design requirements highlighted in the previous chapter, subsection 3.2.3, will obviously obviate the above mentioned complications, once the balun is implemented with the IRA. Our trifilar balun is conceived from coupled transmission line theory which offers wider bandwidths and greater efficiencies [14].

4.2 Coupled Transmission Lines

A transmission line is composed of two or more conductors which carry EM wave along the length of the conductors from one place to another and examples include; parallel-wire/plate lines, coaxial lines and microstrip lines [73]. There exists a magnetic field around a current-carrying conductor. Thus, when two transmission lines are in close proximity, the magnetic flux of one line couples into a second line such that a fraction of its electromagnetic (EM) energy can be traced on the second line . The sharing of fields in transmission lines in such a fashion can either be desirable as in the case of directional couplers [74], or undesirable as in the case of a multi-channel conductor line. This phenomenon is referred to as *coupling* in the former case and *crosstalk* in the latter case. This section highlights various coupled transmission lines in microstrip structures.

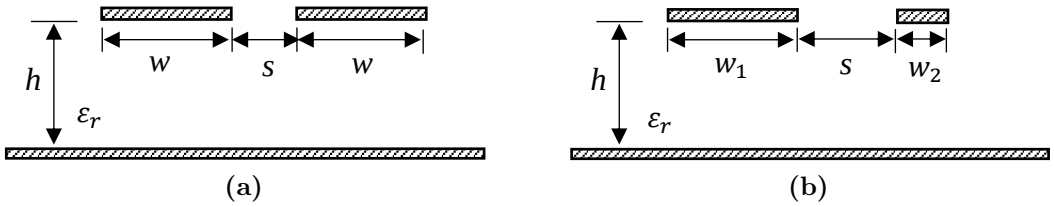

Figure 4.2: (a) Cross-section of a symmetric coupled microstrip line (b) Cross-section of asymmetric coupled microstrip line.

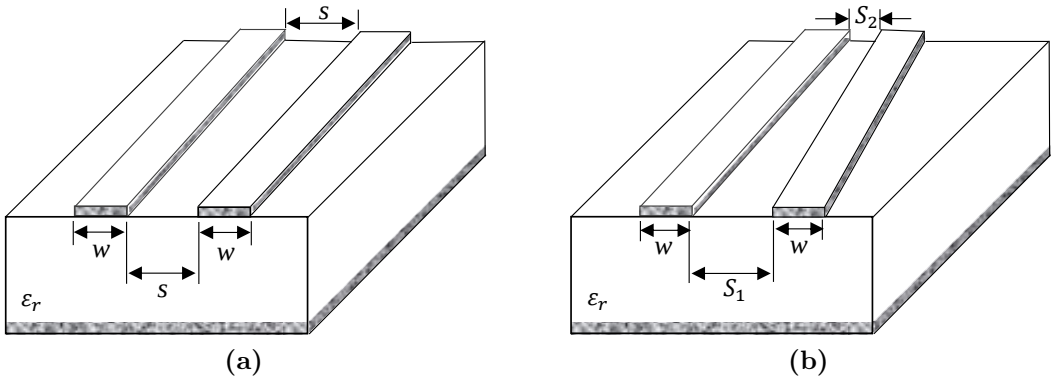

Figure 4.3: (a) Uniformly coupled symmetric microstrip line structure (b) Non-uniformly coupled symmetric microstrip line structure.

4.2.1 Types of Coupled Microstrip Transmission Lines

A typical microstrip transmission line has metal conductors (copper) on both sides of an insulating substrate with erased copper on the top-side of the substrate to create conductive tracks and the bottom-side forms the ground plane (Figure 4.3). The EM fields around the tracks are exposed to a non-homogeneous media (dielectric material and air) and hence propagate through both media. This type of configuration does not fully support pure transverse electromagnetic (TEM) modes because of a small portion of the field which is contained in the air, hence supports only quasi-TEM (partially TEM) modes. However, since most of the EM energy is confined within the substrate (due to high dielectric constant) TEM approximations are used to determine the electrical characteristics of the coupled lines [75].

When the traces have equal widths, w, as shown in Figure 4.2 (a), the layout is referred to as *symmetric coupled-line structure*. On the other hand, unequal line widths, $w_1 \neq w_2$, such as in Figure 4.2 (b) leads to an *asymmetrically coupled-line configuration*. A constant edge-to-edge spacing between the conductor traces allows uniform coupling between the traces. Therefore, Figure 4.3 (a) is an excellent example of a *uniformly coupled symmetric line structure*. However, if the spacing is not the same, $s_1 \neq s_2$, then the structure is called

a *non-uniformly coupled symmetric line* (see Figure 4.3 (b)). Most of the couplers are designed based on symmetric configurations [69], but a combination of different layouts provide more degree of freedom in designing coupled structures. For instance, in an asymmetric coupler, there is the coupling of EM energy as well as changes in impedance. This can be advantageous depending on the application of the coupled structure as we shall demonstrate in our final balun design.

There are other types of coupled-line configurations such as the *broadside-coupled structure*, where the conductor strips are sandwiched between two ground planes [69, 75]. Transmission lines of this form (with traces within the substrate) are known as stripline and allow tight coupling and TEM mode propagation due to homogeneous dielectric medium [75], but are difficult to fabricate. We have only illustrated some of the edge-coupled structures which are relevant for our balun design: symmetric coupled-line structure, asymmetrically coupled-line configuration and non-uniformly coupled symmetric line, but more layouts can be found in [69, 75, 19, 76]. Having discussed different coupling topologies in microstrip PCBs, it is natural to look at various factors that influence the coupling process itself. This is done in the following subsection.

4.2.2 Coupling Mechanisms

Figure 4.4 shows the distribution of EM fields for the even- and odd-mode excitations on coupled microstrip structures. For the even-mode excitation (Figure 4.4 (a)), the currents in both traces have equal amplitude and flow in the same direction or the trace potentials are the same, i.e., $+V_1 = +V_2$. Whereas in the odd-mode excitation (Figure 4.4 (b)), the currents in the traces have equal amplitude but flow in the opposite directions or the trace potentials are equal but of opposite polarities, i.e., $+V_1 = -V_2$ [19]. The fields from one trace couple and induce electromagnetic force (EMF) on the other trace. The induced EMF (coupled energy) depend on the even- and odd-mode characteristic impedances (Z_{0e}

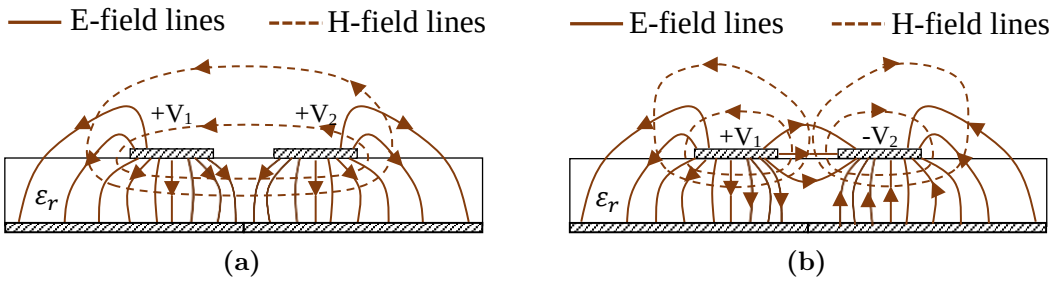

Figure 4.4: (a) Even-mode in a uniformly coupled symmetric line (b) Odd-mode in a uniformly coupled symmetric line.

and Z_{0o}), dielectric properties of the substrate and the coupling length [75, 77].

For a uniformly coupled symmetric structure in Figure 4.4, assuming the traces have zero thickness and are perfect conductors, the coupled differential equations for the two conductor lines are given as follows [77].

$$\frac{d\mathrm{V}_1}{dx} + j\omega L_{11} I_1 = -j\omega L_{12} I_2, \tag{4.1a}$$

$$\frac{d\mathrm{I}_1}{dx} + j\omega C_{11} V_1 = -j\omega C_{12} V_2, \tag{4.1b}$$

$$\frac{d\mathrm{V}_2}{dx} + j\omega L_{22} I_2 = -j\omega L_{21} I_1, \tag{4.1c}$$

$$\frac{d\mathrm{I}_2}{dx} + j\omega C_{22} V_2 = -j\omega C_{21} V_1, \tag{4.1d}$$

where I_1 and I_2 are the trace currents, C_{12} and C_{21} (Figure 4.5) are the capacitances between the strip lines without the ground plane, C_{11} and C_{22} are the capacitances between one trace and the ground without the other trace, L_{12} and L_{21} are mutual inductances, L_{11} and L_{22} are self-inductances of the strip lines, x is the longitudinal coordinate and the time-dependent exponential term ($j\omega t$) is restrained. Due to structural symmetry of Figure 4.4, the matrices derived from equations (4.1a)–(4.1d) for the capacitance and inductances are also symmetric, i.e., $C_{11} = C_{22}$, $C_{12} = C_{21}$, $L_{11} = L_{22}$ and $L_{12} = L_{21}$. The propagation constant for even- and odd-mode are provided by equations (4.2a) and (4.2b), respectively.

$$\gamma_{0e} = j\omega[(L_{11} + L_{12})(C_{11} + C_{12})]^{1/2}, \tag{4.2a}$$

$$\gamma_{0o} = j\omega[(L_{11} - L_{12})(C_{11} - C_{12})]^{1/2}, \tag{4.2b}$$

The equations for Z_{0e} and Z_{0o} are presented as:

$$Z_{0e} = \left[\frac{L_{11} + L_{12}}{C_{11} + C_{12}}\right]^{1/2}, \tag{4.3a}$$

$$Z_{0o} = \left[\frac{L_{11} - L_{12}}{C_{11} - C_{12}}\right]^{1/2}, \tag{4.3b}$$

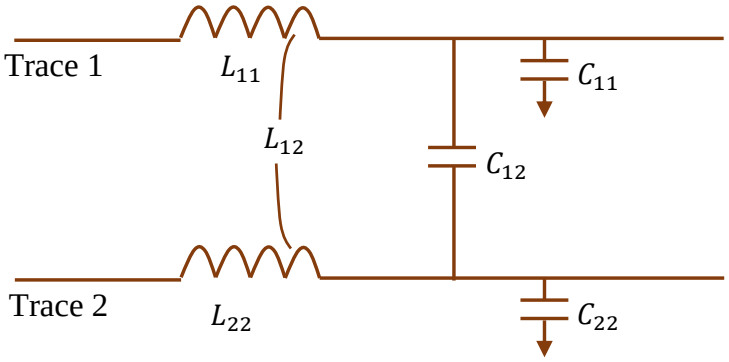

Figure 4.5: Equivalent capacitance and inductance network of the coupled transmission line in Figure 4.4.

Numerical techniques, like the method of moments (MoM), for example, make the computation of the matrix elements C_{ij} and L_{ij} from equations (4.2) and (4.3) fairly simple [77]. For large trace-spacing ($s/w \gg 1$), the effect of coupling elements C_{12} and L_{12} is minimised and equation (4.2) nears the propagation constant of an isolated trace, γ_0.

$$\gamma_0 = j\omega(L_{11}C_{11})^{1/2} \tag{4.4}$$

Similarly, the characteristic impedances in equation (4.3) simplifies to equation (4.5) which estimates Z_0 for an isolated trace.

$$Z_0 = (L_{11}/C_{11})^{1/2} \tag{4.5}$$

Furthermore, Z_0 is dependent on the dimensions of a PCB structure as described in section 4.4. Therefore, the estimation of Z_0 is a simple calculator problem because the dimensions of the structure are easily known or assigned. The following section introduces the design work-flow of the trifilar coupled-line balun, verification of the initial prototype through simulation and measurement and factors to consider for the final balun design.

4.3 Trifilar Coupled-line Balun

In coupled transmission lines the terms trifilar and bifilar are used to mean a three-wire or two-wire line, respectively. Trifilar wound transformer balun (Ruthroff) and bifilar transmission line transformer (Guenella) are discussed in [14]. The requirements for our trifilar balun are mentioned in the previous chapter subsection 3.2.3. The flowchart in

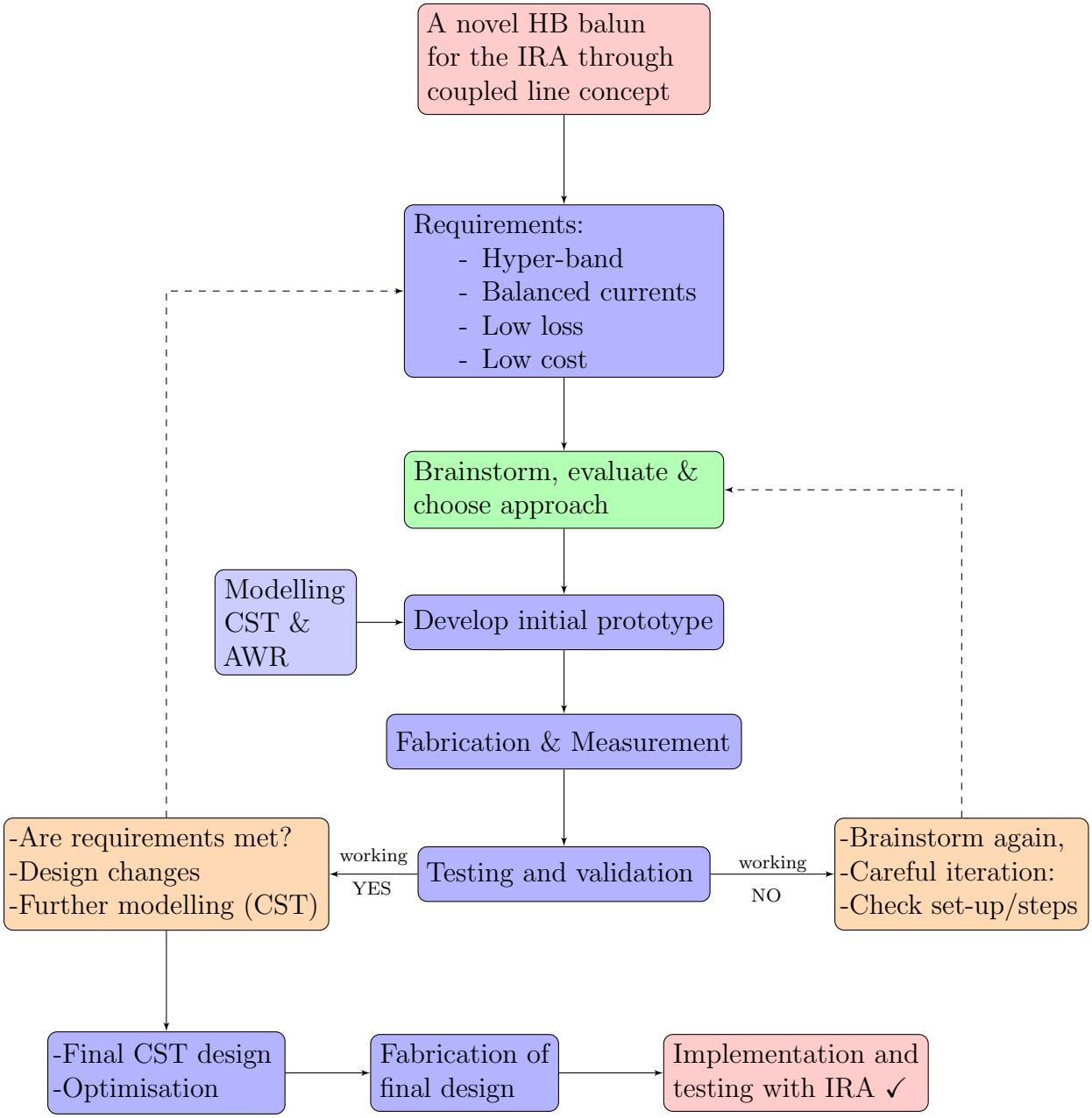

Figure 4.6: Flowchart illustrating the design process of the trifilar balun.

Figure 4.6 is used as a guide to successfully meet these requirements.

4.3.1 Design Concept

The concept of the trifilar balun is based on coupled line theory. Following the design requirements for the balun, a prototype is developed, tested and validated using simulation and measurement. Using the design work-flow in Figure 4.6, the prototype balun passes the testing and validation phase as, – working 'YES'–, hence we move to the appropriate box(es) and proceed as follows:

(i) Check whether the prototype fully or partially meet the design requirements, brainstorm on the possible design changes, carry out further CST modelling and reiterations. It is a repeat process (loop) as shown in the flowchart until a desired performance is achieved.

(ii) Optimise the computational model and obtain the final design for fabrication.

(iii) Incorporate the fabricated balun together with the IRA for further testing and analysis. This is done in chapter 5.

If, however, the prototype fails to work, – working 'NO'–, the right hand-side loop in Figure 4.6 can be applied iteratively until the balun starts to work, then follow the procedure highlighted in steps (i)–(iii).

4.3.2 Initial Prototype of the Trifilar Balun

The initial design of the balun is an edge-coupled structure composed of a single-grounded substrate of dielectric constant, $\varepsilon_r = 3.55$, and three conductor lines as presented in Figure 4.7. The central conductor strip forms the primary line while the other two conductor strips are the secondary lines. All the traces have equal width, w, and constant spacing, s, between them, hence the structure has a uniform and symmetrically coupled microstrip line configuration. The primary line has two ports; the active port 1 and the termination port 4. The output ports are created on the secondary lines on one end, and the opposite ends are terminated as short and open as shown in Figure 4.7 (a).

It is common knowledge that the reflection coefficient of a shorted line is -1, while that of an open transmission line is +1. Thus, it is expected that the coupled and reflected signals on the secondary lines have equal amplitudes of opposite sign at the output ports 2 and 3. The intention is to create balanced and opposite polarity signals to drive the positive and negative feed-arms of the IRA, simultaneously. Parameters used for prototyping the balun model are given in Table 4.1. The value of trace width is chosen such that the characteristic impedance of each trace is approximately 50 ohm. A trade-off between tight coupling and the fabrication constraint of the etching machine influences the choice of the value for the trace spacing.

A sketch of the fabricated prototype is given in Figure 4.8 (a) followed by the prototype itself in Figure 4.8 (b). Similarly, the parameters in Table 4.1 are used to design the fabricated trifilar balun. The balun is etched from a small piece of double-sided Rogers RO4003C PCB material available from our mechanical engineering workshop. The size of the Rogers material is the contributing factor in determining the length, l_{sub}, of the

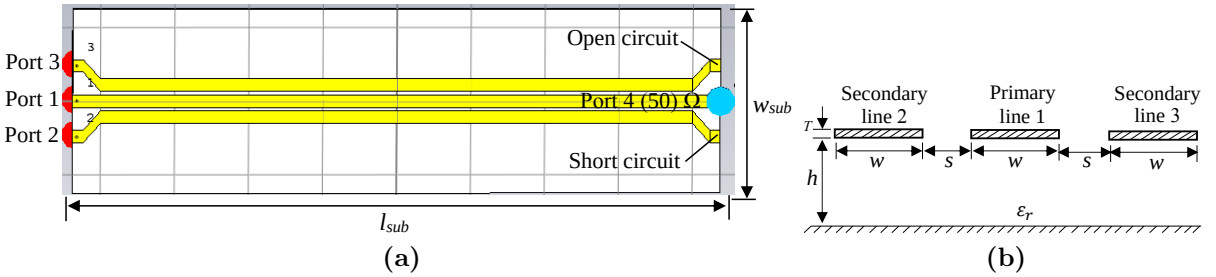

(a) (b)

Figure 4.7: (a) Top view of the CST computational model of the trifilar coupled-line structure (b) Cross-sectional view of the uniformly coupled symmetric trifilar line structure.

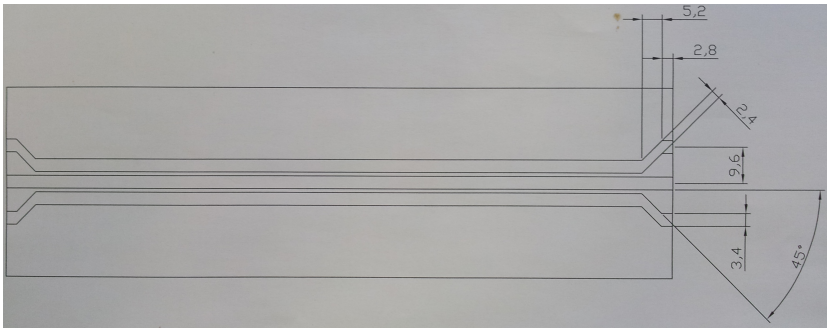

(a)

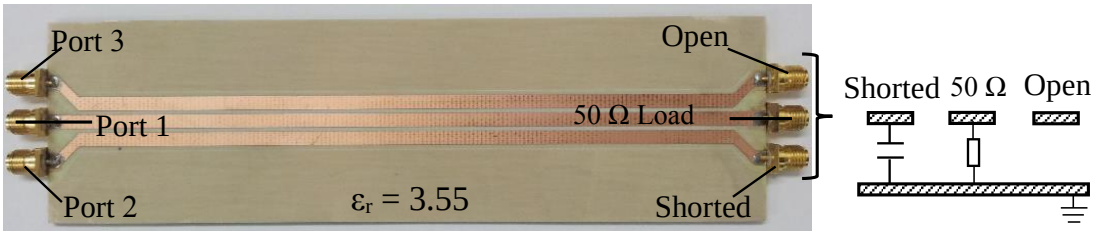

(b)

Figure 4.8: (a) A sketch of the fabricated prototype with the linear dimensions of its flared section in mm (b) A fabricated prototype of the trifilar edge-coupled-line balun with the terminations shown on the right-hand side.

prototype balun. Usually, the FR4 PCBs are ordered at the workshop because they are affordable compared to Rogers PCBs. However, we prefer to use the only available Rogers PCB due to its better frequency properties over FR4 material. The printing of the PCB and all the electrical connections are done at the workshop.

The linear dimensions of the flared sections of the secondary traces are provided in Figure 4.8 (a). A minimum bend angle of 45° (off the longitudinal edges of the middle trace) is used to modify the bent sections at the opposite ends of the adjacent lines. The slight modifications are made so that there is enough spacing between the female SMA (Sub-Miniature version A) connectors for proper connections during test measurements. In order to validate the model we execute both simulation and experimental set-ups and result analysis.

Table 4.1: Parameters used in the design of the prototype of the trifilar edge-coupled balun.

Parameter	Value (mm)	Parameter	Value (mm)
l_{sub}	175	T	0.035
w_{sub}	50	s	1
h	1.524	w	3.4

4.3.3 Simulation Set-up

The balun structure in Figure 4.7 (a) is a model created in CST which is simulated using a transient solver, Finite Integration Technique (FIT), for faster computation runs. The excitation port 1 is defined as 50 ohm with a unit voltage source shown in Figure 4.11 (a). The primary conductor is accurately matched by terminating port 4 with a 50 ohm load. All the ports including the shorted end of the secondary line 3 are grounded to the bottom plate of the model. In addition to the CST results, we carry out another computational simulation using a different simulation tool called microwave office (AWR). The use of more than one simulation tool is a great alternative to a faster and better validation process especially when the fabrication of the prototype is based on the outcome of the simulation results. Just to clarify the procedure, we first validate the prototype model using CST and AWR and thereafter make the fabricated prototype and compare measurement with simulation results.

The microstrip structure in AWR is implemented through the EM quasi-static method reported in [78]. It considers losses in dielectric materials and metals and partially accounts for dispersion effects [78]. Figure 4.9 shows the simulation set-up used including parameters for electrical components. We set the default accuracy value of simulation as 1 because it provides a better trade-off between accuracy and simulation time. The input pulse is the

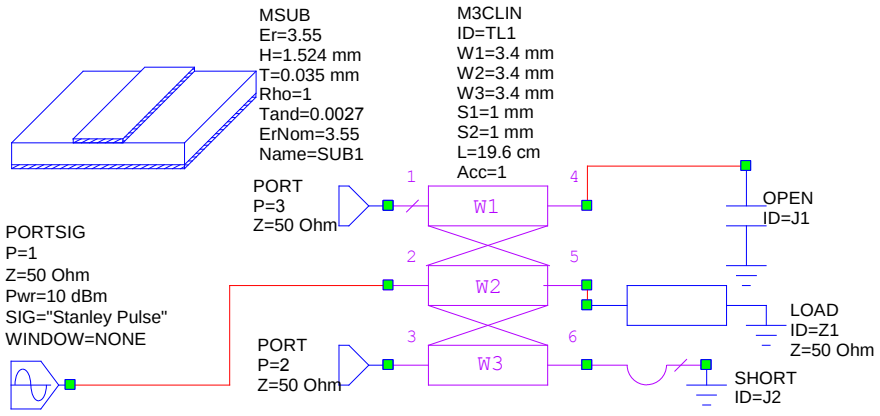

Figure 4.9: Simulation set-up of the trifilar coupled-line balun in microwave office (AWR).

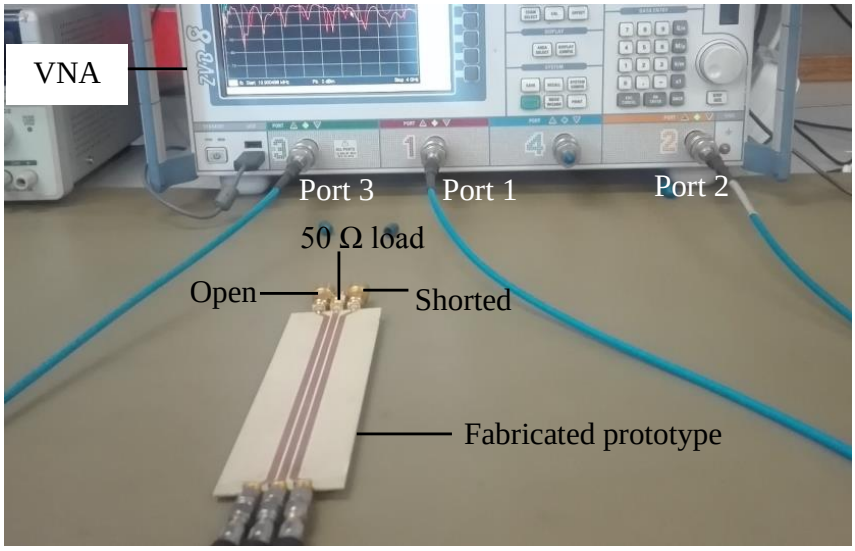

Figure 4.10: Measurement set-up of the coupled-line prototype balun connected to the VNA. The ports that feed the IRA are the output ports 2 and 3, port 1 is used as the input.

same as the one used in CST (Figure 4.11 (a)). However, it is very challenging to model the exact pulse in AWR. Therefore, we predefine it in CST and import it in AWR as a *.sig file, renamed as "Stanley Pulse".

4.3.4 Measurement Set-up

Figure 4.10 is a measurement set-up where the prototype balun is connected to a four-port Rohde & Schwarz Vector Network Analyzer (VNA) for FD measurement. Only three ports of the VNA required for the set-up are calibrated using a typical Short-Open-Load-Thru (SOLT) procedure. Since the VNA takes full FD measurement, it uses the Fourier Transform to convert to TD. This feature makes it possible to determine TD responses with the VNA. The first port 1 of the VNA is connected to the primary line and is the source of the unit pulse signal. The coupled fields on the secondary tracks are measured as output signals at ports 2 and 3 of the VNA. Care has been taken to ensure that the configuration and measurement set-up of the fabricated prototype is similar to those in the simulation environment of CST and AWR already discussed in this section.

However, there is a slight difference in the secondary traces of the fabricated structure and the CST model; and that is the bent sections seen in Figures 4.8 and 4.7. It is not possible to model the flared sections on AWR but their length (5.2/cos(45°) mm) including the connector length (8 mm) in the fabricated structure, have been accounted for in the simulation models.

4.3.5 Result Analysis

The plots in Figure 4.11 (b) and Figure 4.13 are used to compare simulation and measurement results for validation of our initial balun model. The TD comparison between CST and measured data in Figure 4.11 (b) show good agreement except for slight variations in magnitude and time difference. Due to the small structural differences in the fabricated prototype, the variation between simulation and measurement as seen in Figure 4.11 (b) is expected. For example, the transition between the transmission lines and the connectors in the fabricated trifilar balun is not perfect (or smooth). The soldering done at the connection point creates a blob and as a result, some energy is lost at the joints. This explains why the magnitude of the TD plot determined from the VNA is less compared to the simulation plot. According to the investigations in subsection 4.4.3.2, the sinusoidal-type double pulse is directly linked to the length of the balun structure. Therefore, the time-difference, $\Delta t = 0.045$ ns, between the two sinusoidal-type pulses in Figure 4.11 (b) can be attributed to minor differences in the secondary traces or the dielectric material of the fabricated structure.

In addition, the manifestation of the pre-pulse is different from the sinusoidal-type double pulse during the coupling process. The sinusoidal-type double pulse is formed as a result of forward coupling while the pre-pulse is due to the backward coupling. The time-derivative of the original pulse (Figure 4.11 (a)) in the primary line causes the forward coupling in the secondary line, i.e., the sinusoidal-type double pulse seen in Figure 4.11 (b). However, during the reverse coupling the pulse in the secondary line reintegrates itself to form the pre-pulse (single pulse) which looks like a copy of the original pulse. Additional evaluation of the balun structure is done in FD through Figures 4.12 and 4.13.

As depicted in Figure 4.12 (a) the reflection coefficient of the primary line port 1 is below -10 dB, an indication that the line is well matched. On the other hand, there is a substantial level of reflection on the secondary lines, and this is expected because of the open and shorted terminations. The graphs of transmission parameters in Figure 4.12 (b) indicate a strong coupling between the main port 1 and the secondary ports 2 and 3 as compared to the coupling between the secondary ports only. For the FD results in Figure 4.13, the CST, AWR and measurement plots show close agreement over the frequency band with magnitude difference being within 5 dB except at resonance points.

It should be noted that the objective of the prototype design is to use it as a proof of concept; whether the generation of two equal but opposite polarity signals for the excitation of the positive and negative plates of the IRA, is attainable with the couple-line structure. In this regard, it can be deduced that the coupled output signals within 2–3 ns in Figure

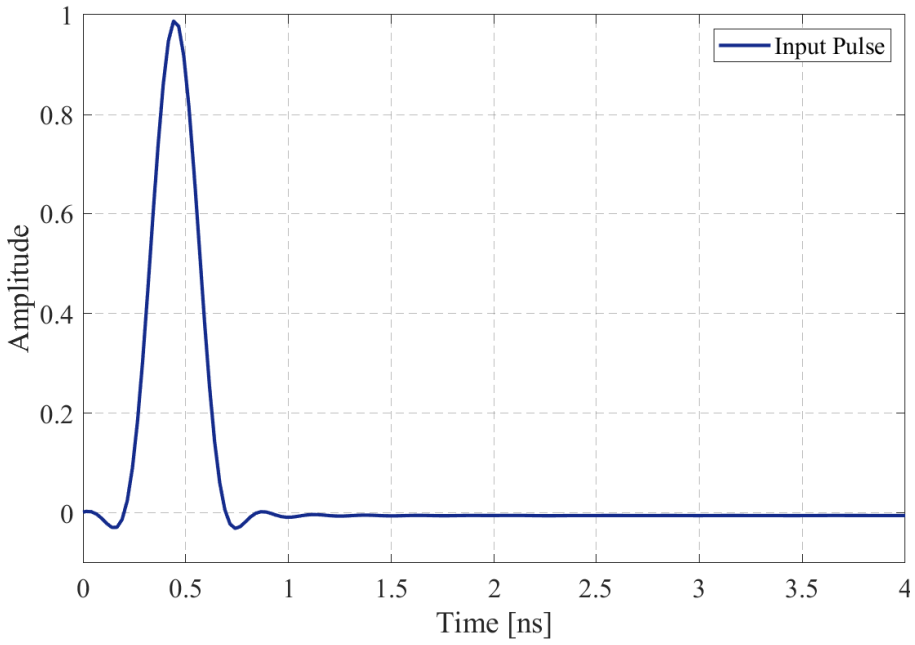

(a)

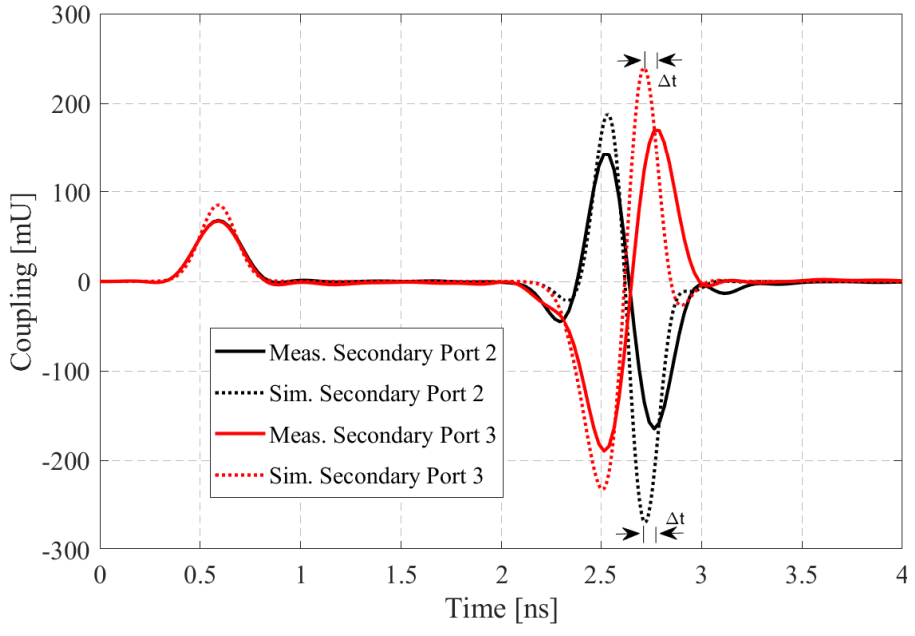

(b)

Figure 4.11: (a) Pulse signal of one unit amplitude used as excitation source in CST, AWR and VNA (b) Comparison of TD results of CST and measurement of coupled output signals at ports 2 and 3.

4.11 (b) have the main characteristics required as excitation signals for the IRA. While the coupled pre-pulse (appearing before 1 ns) is undesired for the proper functioning of the balun (balanced feeding) since they have the same polarity. Thus, the following need to be considered in the final model of the trifilar coupled-line balun:

(i) Changing the characteristic impedance of the secondary tracks so that they match the intended input impedance of the antenna (200 ohms), i.e., 100 ohm per track as demonstrated in section 4.4.

(ii) A configuration which would permit a good trade-off between adequate coupling for the wanted forward or far-end coupling (FEC) on the adjacent tracks and reduced

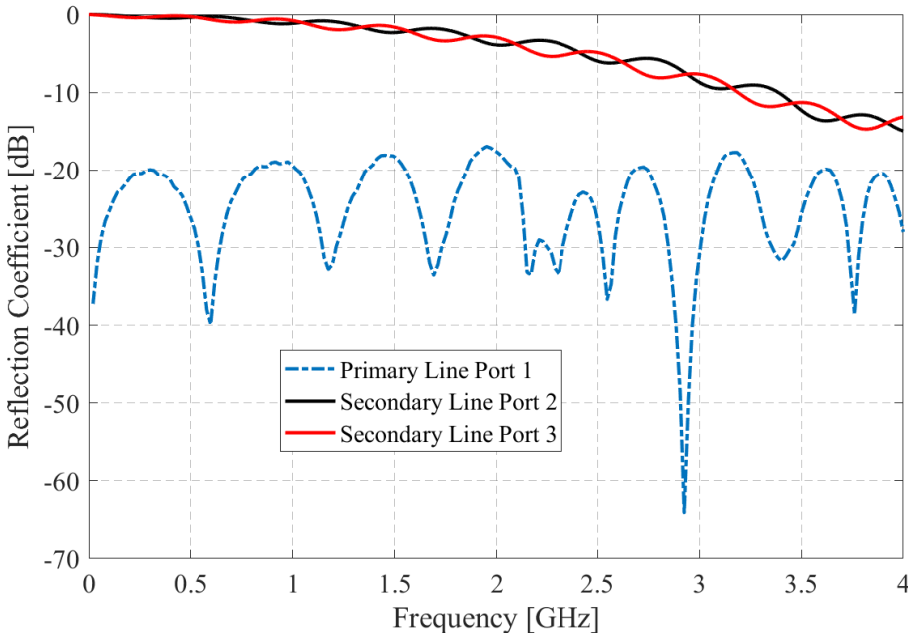

(a)

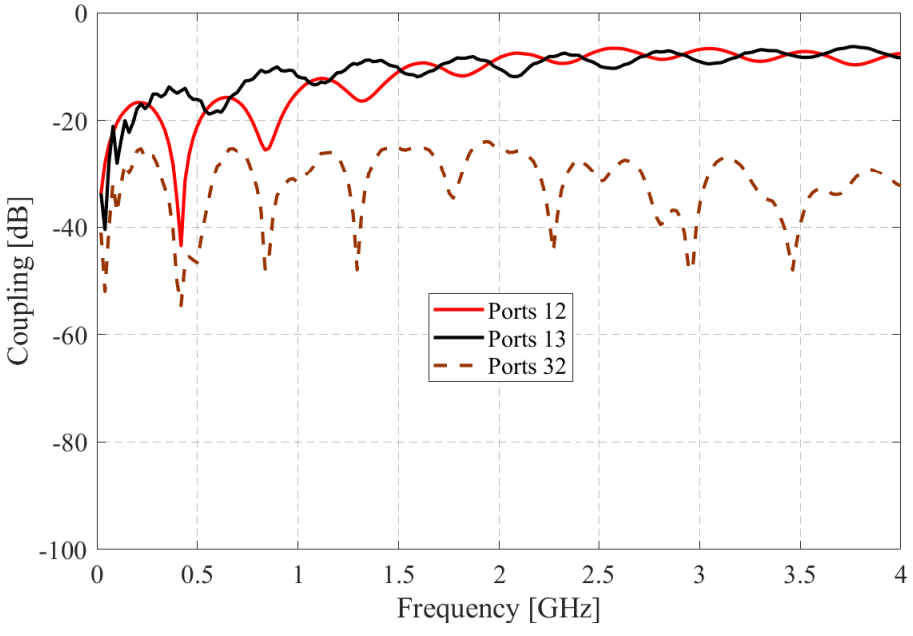

(b)

Figure 4.12: (a) Reflection coefficient measurement results for ports 1, 2 and 3 (b) Graphical representation of the measured data for coupling between ports 1, 2 and 3.

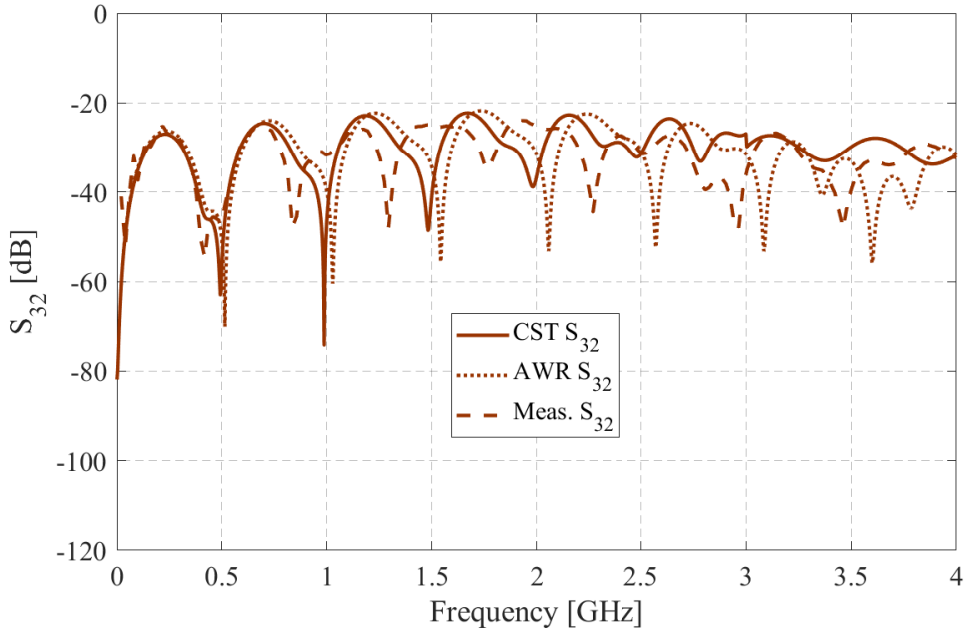

Figure 4.13: Comparison of S_{32} from CST, AWR and measurement.

reverse or near-end crosstalk (NEXT) which leads to unwanted pre-pulse.

(iii) Optimisation of the coupled-line structure for balanced excitation signals including the actual placement of the balun on the IRA antenna.

Further modelling and optimisation of the trifilar balun is executed in the following section so as to achieve the balun design requirements in chapter 3, subsection 3.2.3, as well as the highlighted items (i)–(iii) in the previous page.

4.4 Further Modelling of Trifilar Balun

The first part of this section presents the material requirement and calculation of the line impedances of the trifilar balun, followed by a brief description of the final balun and its design parameters. Finally, we discuss the modelling considerations which contribute to the final balun structure.

4.4.1 Material Requirement and Line Impedance

One of the key requirements for the final design of the balun is a suitable material with low loss, especially at high frequencies. The core for the Rogers PCB material has better high-frequency properties than the FR4 core used in the initial prototype balun. This makes the Rogers PCB a better choice for the required HB balun. The material available

from the fabrication company for our balun is Rogers RO4003C with $\varepsilon_r = 3.55$, $T = 0.035$ mm, and $h = 0.813$ mm.

The Z_0 required for each secondary line is 100 ohm, which is set to match the impedance of a parallel combination of two conical plates of the IRA. The primary line is 50 ohms matched to a coaxial line that is connected to a standard 50-ohm source. Since Z_0 is a function of the dimensions and dielectric constant of the material, it can be calculated once the values of the required parameters are known. A number of equations have been developed using remarkable and varied analytical and numerical methods for calculation of Z_0. However, the Wheeler equation (4.6) and Schneider's equations (4.7) and (4.8), which appear detailed and complex, are recommended because of the great accuracy obtained in calculating Z_0 [69, 79].

$$Z_0 = \frac{\eta_0}{2.0\sqrt{2.0}\pi\sqrt{\varepsilon_r + 1.0}} \ln\left\{1.0 + \frac{4.0h}{w'}\left[\frac{14.0 + \frac{8.0}{\varepsilon_r}}{11.0}\,\frac{4.0h}{w'} + \sqrt{\left(\frac{14.0 + \frac{8.0}{\varepsilon_r}}{11.0}\right)^2\left(\frac{4.0h}{w'}\right)^2 + \frac{1.0 + \frac{1.0}{\varepsilon_r}}{2}\,\pi^2}\,\right]\right\} \tag{4.6}$$

$$\varepsilon^1_{eff} = \frac{\varepsilon_r + 1.0}{2.0} + \frac{\varepsilon_r - 1.0}{2.0}\left[\frac{1.0}{\sqrt{1.0 + \frac{12.0h}{w}}} + 0.04\left(1.0 - \frac{w}{h}\right)^2\right] \quad \text{for} \quad \frac{w}{h} \leq 1.0 \tag{4.7}$$

$$\varepsilon^2_{eff} = \frac{\varepsilon_r + 1.0}{2.0} + \frac{\varepsilon_r - 1.0}{2.0}\left(\frac{1.0}{\sqrt{1.0 + \frac{12.0h}{w}}}\right) \quad \text{for} \quad \frac{w}{h} \geq 1.0 \tag{4.8}$$

where η_0 is the impedance of free space (120π), ε_r is the dielectric constant, h is the thickness of the substrate, ε_{eff} is the effective dielectric constant and w' is a correction parameter linked to the width, w, of the lines as given in appendix C, equation (C.1) [69]. Equations (4.7) and (4.8) are used to simplify equation (4.6) into the following equation:

$$Z_0 = \begin{cases} \frac{60.0}{\sqrt{\varepsilon_{eff}}} \ln\left(\frac{8.0h}{w} + \frac{w}{4.0h}\right), & \text{for} \quad \frac{w}{h} < 1.0 \\ \frac{\eta_0}{\sqrt{\varepsilon_{eff}}\left[\frac{w}{h} + 1.393 + 0.667 \ln\left(\frac{w}{h} + 1.444\right)\right]}, & \text{for} \quad \frac{w}{h} > 1.0 \end{cases} \tag{4.9}$$

The error margin is within 0.02 for the calculation of Z_0 for any value of ε_r and w, and it

Table 4.2: Computed values of Z_0 with equation (4.9) and the associated errors.

Width (mm)	Required Z_0	Equation (4.9)	Error
1.8	50	50.57	0.011
0.45	100	100.66	0.007

is within 0.01 for ε_{eff} in equations (4.7) and (4.8). Assuming that the lines are loosely coupled (s is significantly larger compared to h and w), equation (4.9) is used to determine the impedance of the transmission lines and the associated errors (Table 4.2). However, since the required line impedances, 100 ohm and 50 ohm, are already known, the Wheeler equation is implemented in approximating the values of w_1, w_2 and w_3 in Table 4.3 for the final model.

4.4.2 Final CST Model

The working principle of the final model of the balun is the same as that of the initial model. However, the configuration and other physical dimensions are very different and are carefully and judiciously chosen. It is a non-uniformly coupled asymmetric structure whose design parameters are given in Table 4.3, and the computational model from CST is provided in Figure 4.14.

The CST model uses the Rogers RO4003C (lossy) as the substrate for the PCB with $\varepsilon_r =$

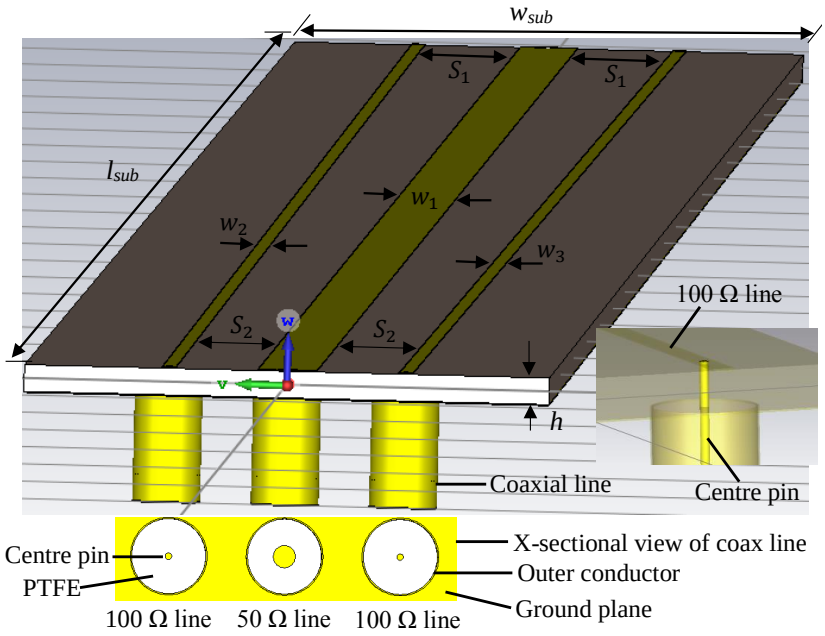

Figure 4.14: A CST computational model of the final design of the balun based on a non-uniformly coupled asymmetric configuration.

Table 4.3: Parameters used in the final design of the trifilar coupled-line balun.

Parameter	Value (mm)	Parameter	Value (mm)
l_{sub}	400	T	0.035
w_{sub}	20	w_1	1.8
s_1	3	$w_2 = w_3$	0.45
s_2	2.5	h	0.813

3.55. A coaxial cable feed for the primary line is modelled with the centre pin radius, r_i = 0.298 mm, outer conductor radius, r_0 = 1 mm, and a PTFE (lossy) material with electric tand = 0.0002 and ε_r = 2.1, as a 50-ohm impedance line (Figure 4.14).

The Rogers RO4003C is selected based on the reasons outlined in the previous subsection while the PTFE is mostly used in the RF coaxial cables. The dimensions of the inner and outer coaxial conductors are chosen such that they provide the required impedances and at the same time there is enough spacing between the cables (Figure 4.14). To create a 100-ohm coaxial port for the secondary lines, the centre pin radius is changed to 0.089 mm. Coaxial lines are commonly used in real antenna measurements and for purposes of consistency we use them in our simulations too.

Various input signals such as Gaussian pulse, square-wave and step pulse are applied to drive the primary conductor. The objective is to see how the type of input pulse affects the behaviour of the output pulse, more specifically on the FEC. Simulations are run through time domain solver and an inbuilt Genetic Algorithm is set for optimisation of s_1 and s_2 to achieve best balance with least NEXT. The goal function was set with the linear magnitude of the coupled output signal at port 2 = port 3, and the goal norm being the sum of squared difference. The minimum values for s_2 = 2 mm and s_1 = 2.5 mm and the maximum values s_2 = 4 mm and s_1 = 5 mm. The final design of the balun described in this subsection is as a result of various simulation set-ups which are considered in the next subsection.

4.4.3 Modelling Considerations in CST

A CST model of the trifilar balun is used for different simulation set-ups in order to investigate design configuration for the balun, how to increase FEC, effect of varying s on NEXT and FEC and how the type of input signal determines the output waveform of FEC.

4.4.3.1 Achieving Balance

Two different configurations are examined with an attempt to find solutions to issues addressed in sub-section 4.3.5, item (ii). The CST model in Figure 4.14 is remodelled separately as a uniform and non-uniform structure with the length, l_{sub}, for both models set to 120 mm (Figure 4.15). For the uniform configuration, $s = 2$ mm, while the non-uniform model is created by adjusting s by 0.5 mm at one end of the model so as to have $s_1 = 2.5$ mm and $s_2 = s = 2$ mm (Figure 4.15 (b)). The parameter s is any value greater than w_1 and w_2 for loosely coupled lines as mentioned in subsection 4.4.2. For the non-uniform structure s_1 must have any value different from s_2, hence we define 2.5 mm for s_1 (s_1 being greater than s_2). The length l_{sub} can be any value but we define a shorter length, 120 mm, to reduce computational time. A unit Gaussian pulse in Figure 4.21 (a) is defined as the source signal. The comparison of the coupled output energy in both structures is as plotted in Figure 4.16.

The magnitude of the unwanted pre-pulse (NEXT) for the non-uniform configuration is less compared to that of the uniform structure due to small variations on s between both configurations. Due to the same reason, the peak to peak magnitude of the desired output (FEC) is less but more balanced in comparison to the uniform configuration. Thus, the non-uniform configuration tends to resolve part of the issue in (ii) which is the minimisation of NEXT but not the other aspect of improving the magnitude of FEC. Fortunately, according to the results in sub-subsections 4.4.3.2 and 4.4.3.3 the pre-pulse only depends on s while FEC depends on both s and l_{sub}. This means that one can design a non-uniform model with (fixed s_1 and s_2) less NEXT and balanced FEC and vary l_{sub} for increased FEC.

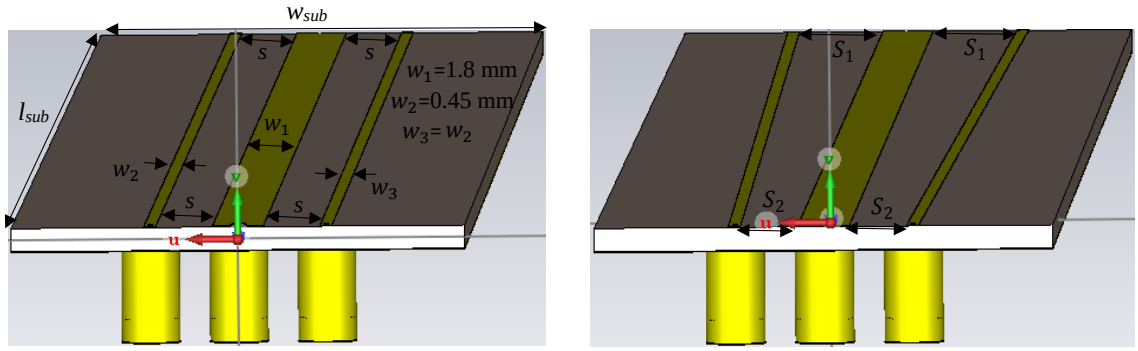

(a) **(b)**

Figure 4.15: (a) Uniformly coupled symmetric structure of the trifilar balun (b) Non-uniformly coupled symmetric structure of the trifilar balun.

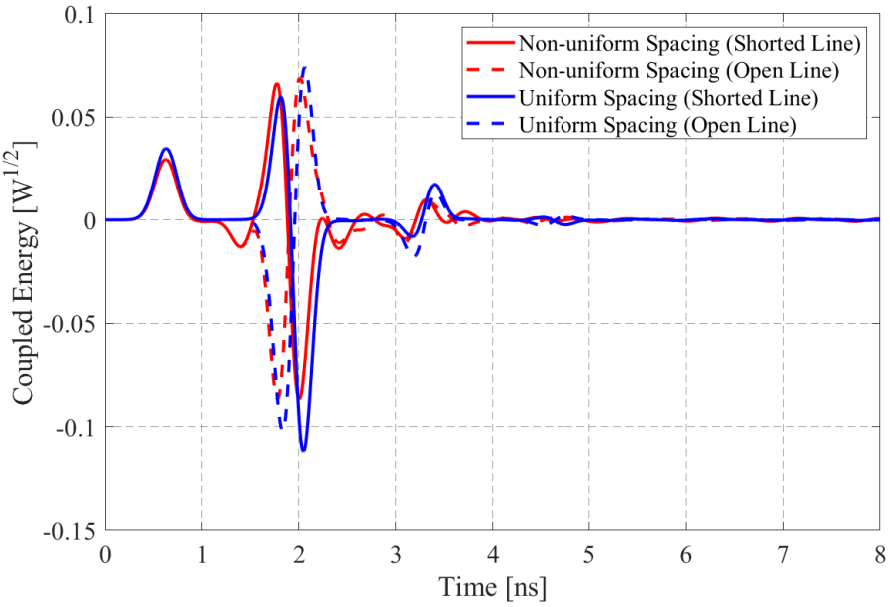

Figure 4.16: Comparison of coupled energy between a uniform and non-uniform CST coupled-line balun with $s = 2$ mm for the uniform model whereas for non-uniform, $s_1 = 2.5$ mm and $s_2 = 2$ mm.

4.4.3.2 Increasing Coupling

A duplicate version of the CST model (Figure 4.14) is used to investigate the effect of varying length on the coupled output signals. Two input signals are selected separately to excite the primary line: a unit square-wave pulse and a unit smooth-step function. The rise time, T-rise, and fall time, T-fall, of the square-wave pulse (Figure 4.17 (a)) is 0 ns and has a time hold, T-hold, of 1 ns between 0–1 ns. The step-function (Figure 4.18 (a)) has an amplitude rise of 80 % and T-rise of 0.133 ns.

From both Figures 4.17 (b) and 4.18 (b) the magnitude of the coupled energy (with respect to FEC) increases with increase in length (l_{sub}). However, there is no change in the magnitude of the pre-pulse (NEXT) as l_{sub} is increased. There are two main conclusions derived from these results:

- NEXT is not a function of l_{sub}, therefore, increase in l_{sub} only improves the desired FEC and this addresses the second issue in item (ii), sub-section 4.3.5.
- The linear dependence of FEC on the length of the structure implies that the balun can be connected directly to the conical plates of IRA at the feed apex and then extend its length through the axial symmetry to the back of the reflector. This eliminates the use of coaxial cables usually required to connect the antenna and the balun (details in Chapter 3). For our case, a 100-ohm coaxial cable (less than 2 m) would have been required, but only cables of 50, 70, 75, and 93 ohm impedances

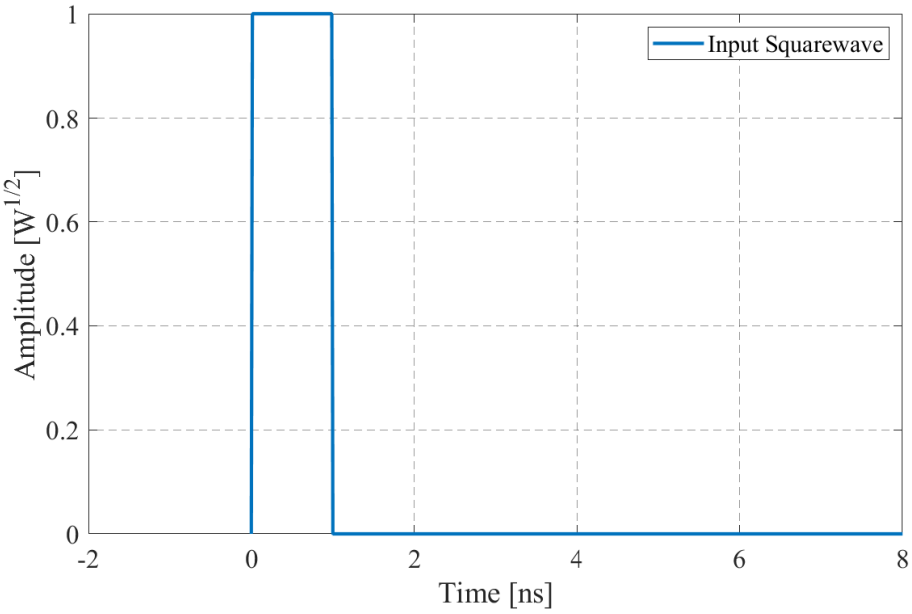

(a)

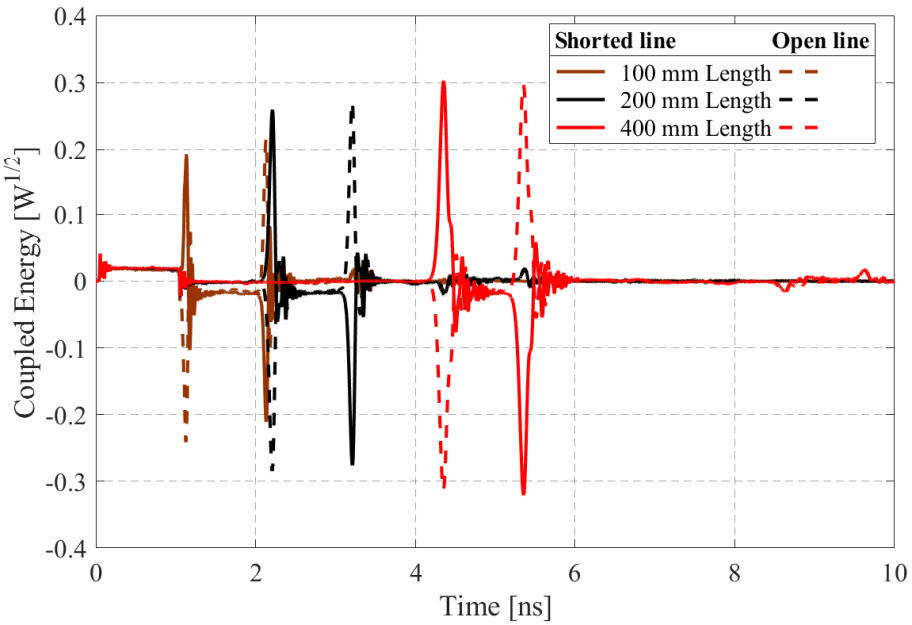

(b)

Figure 4.17: (a) A unit square-wave input pulse with T-hold of 1 ns (b) Coupled output signal as a function of length in mm (optimized CST model in Figure 4.14 applied).

are readily and commercially available in the market [14]. Besides, it is costly to manufacture a custom designed cable of such a short length. The elimination of the outer cables further reduces the chances of common-mode currents influencing balance.

For the final design of the balun, a minimum length of 400 mm is selected. The choice of l_{sub} is dictated by the distance from the feed apex towards the back of the reflector (along

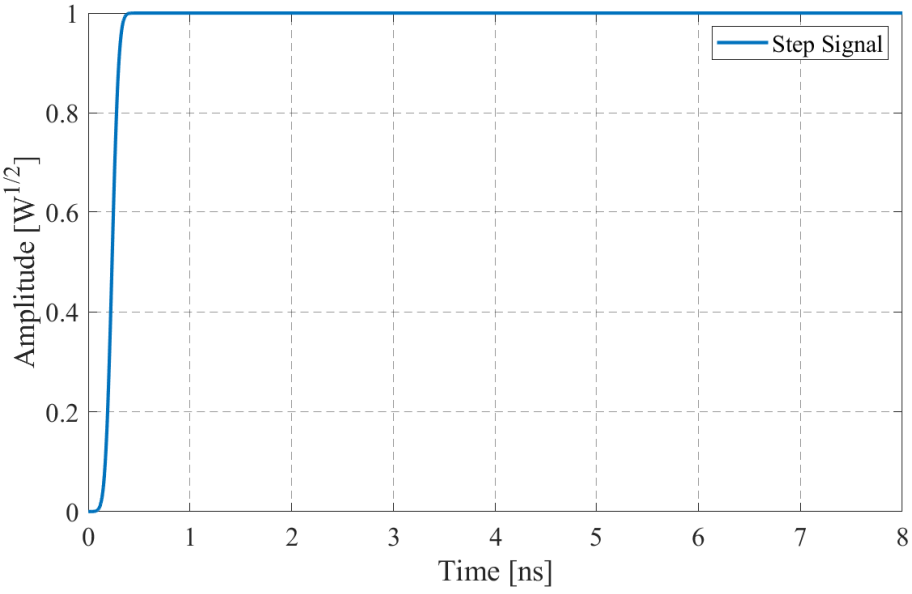

(a)

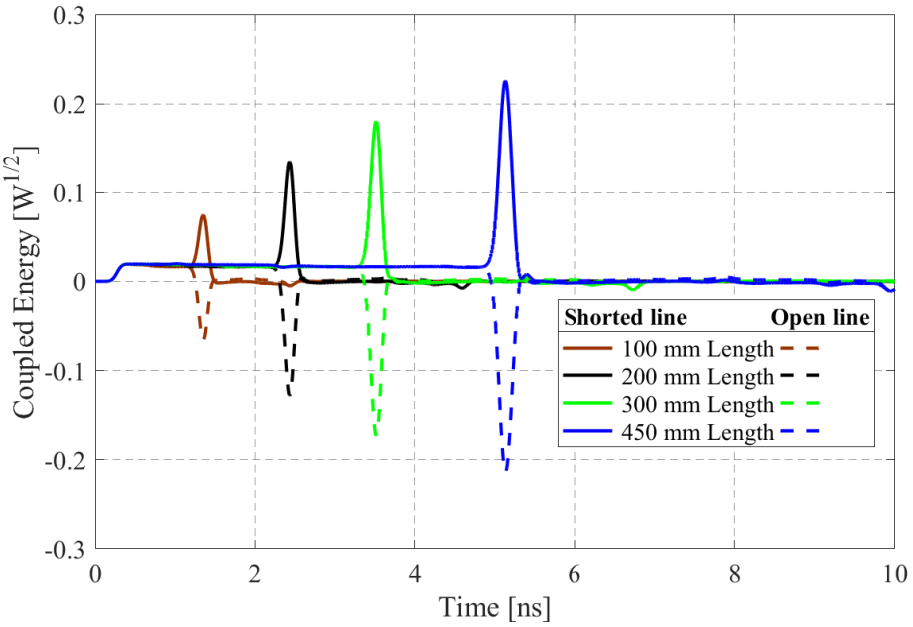

(b)

Figure 4.18: (a) A unit step input function with 80 % rise amplitude (b) Coupled output signal as a function of length in mm (optimized CST model in Figure 4.14 applied).

the symmetry axis) such that there is enough space to make connections to the primary conductor at the back of the dish (refer to chapter 5, section 5.1, subsection 5.1.4).

4.4.3.3 Varying Trace Spacing

The computational model described in sub-subsection 4.4.3.2 is replicated in CST and converted to uniform configuration for linear variation of s. The length of the structure is set as 400 mm and a step pulse in Figure 4.18 (a) is selected as an excitation signal. The graphs in Figure 4.19 show that the magnitude of coupled EM energy on the adjacent traces is inversely proportional to the spacing parameter, s. The further the adjacent lines are from the central conductor the less the fringe fields couple into the lines. The results confirm that s is a critical parameter to be considered in minimising the undesired pre-pulse that can cause potential problems to the balun and the antenna system. Ultimately, however, care must be taken in choosing the appropriate value for s because it reduces FEC as well.

Further analysis is done on the same CST model with the input signal defined as a unit square-wave presented in Figure 4.17 (a). The results are shown in Figure 4.20 where the magnitude of NEXT is less when $s = 3$ mm (Figure 4.20 (b)) compared to $s = 1$ mm (Figure 4.20 (a)). We obtain a smooth and balanced output FEC signals with $s = 3$ mm (Figure 4.20 (b)) in comparison to $s = 1$ mm (Figure 4.20 (a)) where the pre-pulse distorts the shape and balance of the FEC signals.

A point of note is that the secondary lines which form the differential signal are already further apart, hence there is less effect of NEXT between them as demonstrated in Figure 4.12 (b). Also, the dielectric thickness, h, is smaller (0.813 mm) than the initial value of

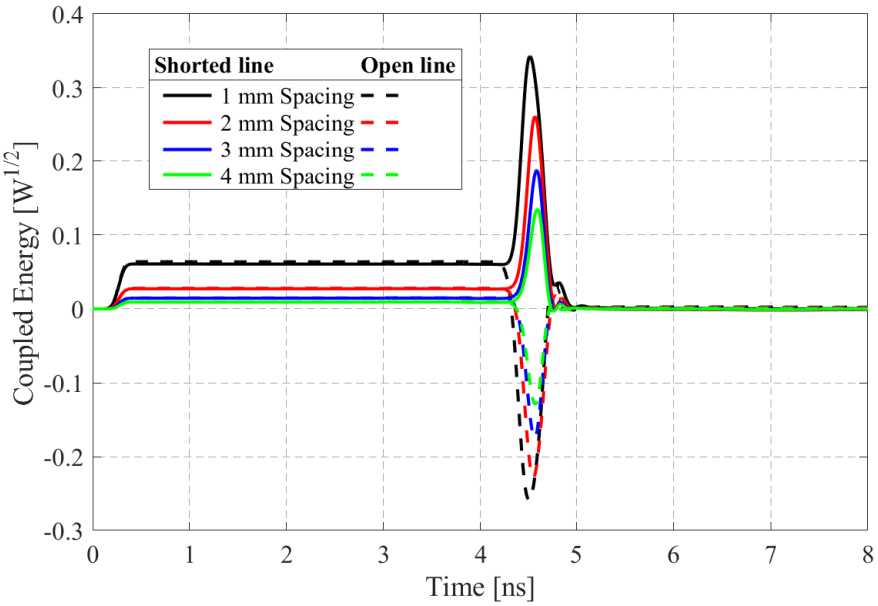

Figure 4.19: Coupled output signals as a function of trace spacing, s, in mm (final CST model in Figure 4.14 is used but with uniform configuration).

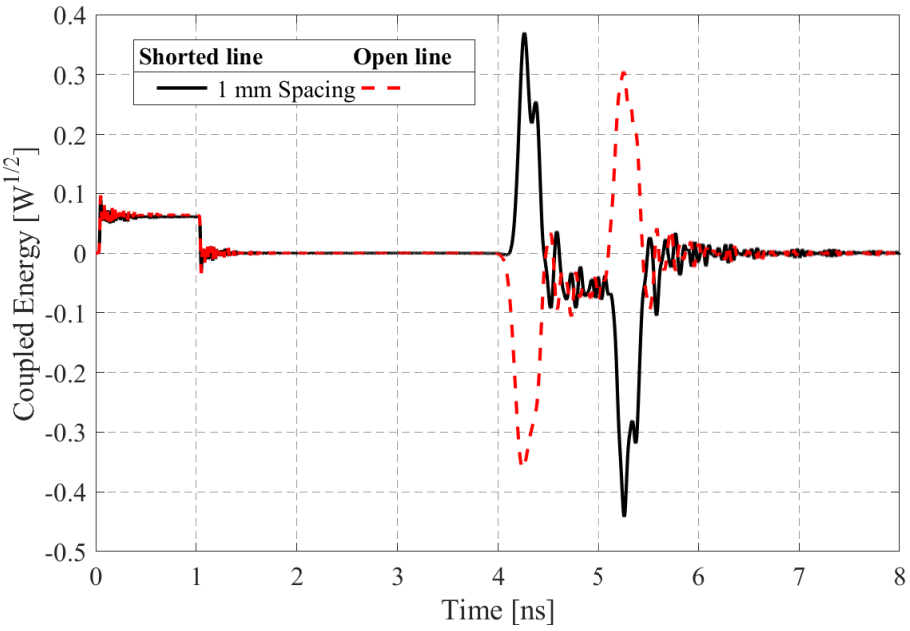

(a)

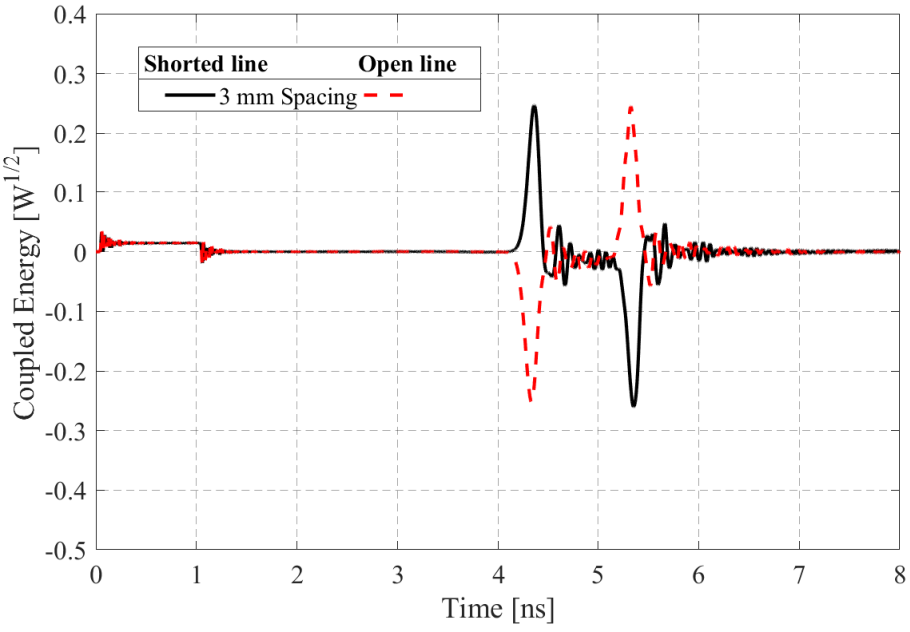

(b)

Figure 4.20: (a) Coupled output signals when $s = 1$ mm and (b) When $s = 3$ mm. In both simulations we use a uniform structure of the computational model (Figure 4.14) and a unit square-wave source signal.

1.524 mm; this allows tight coupling of the differential signal to the return path (ground) and less fringe fields couple between the adjacent lines. Finally, we consider the field distribution on the final balun structure as well as the balance on the output signals when each type of the input signal is applied.

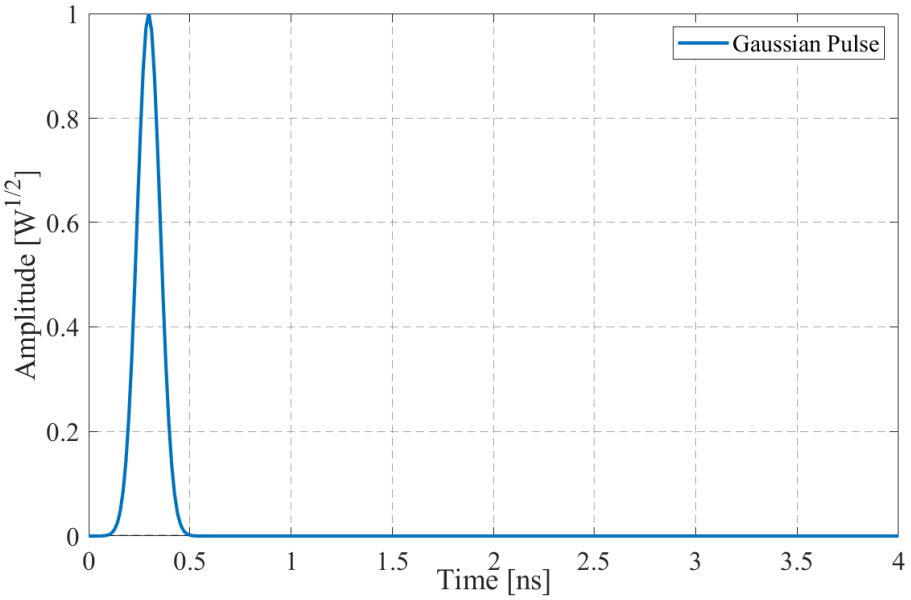

(a)

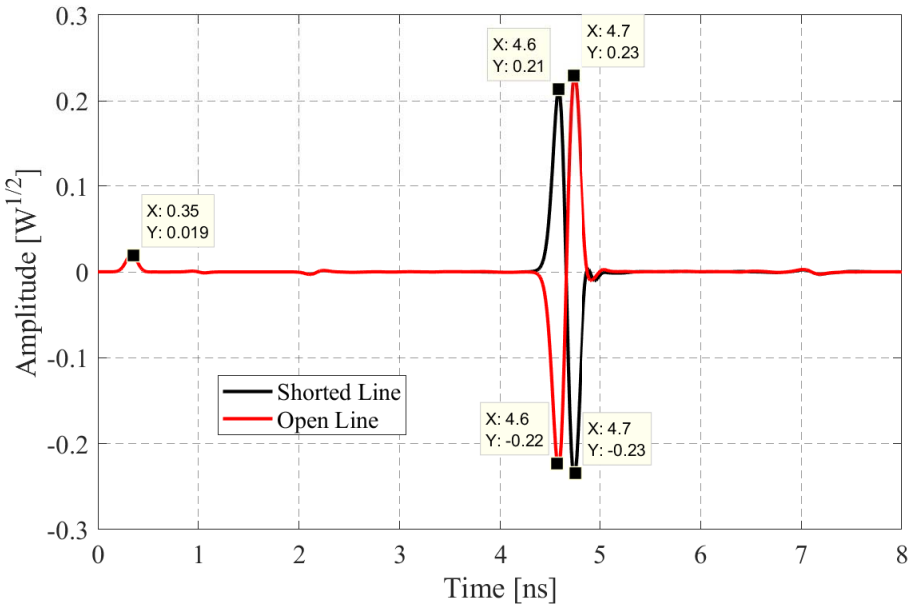

(b)

Figure 4.21: (a) A unit Gaussian input signal (b) Balanced output signals when the final and optimized model in Figure 4.14 is simulated at 6 GHz.

4.4.3.4 Type of Signal and Field Distribution

It is already seen from the previous sub-subsections that the type of input signal selected determines the shape of the output signals. Further analysis is done on the shape and balance of the FEC coupled signals using the final model of the trifilar balun and the three types of input signals used in this chapter.

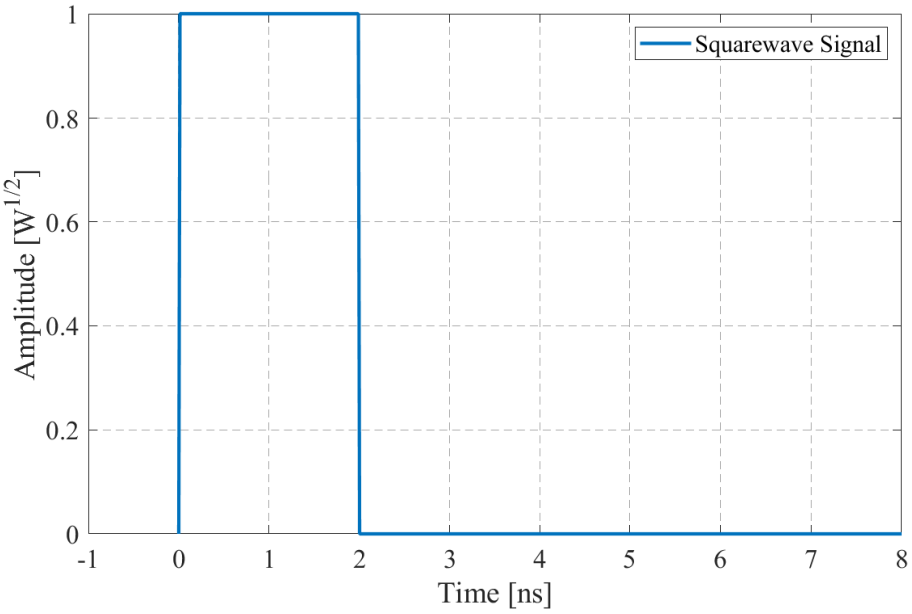

(a)

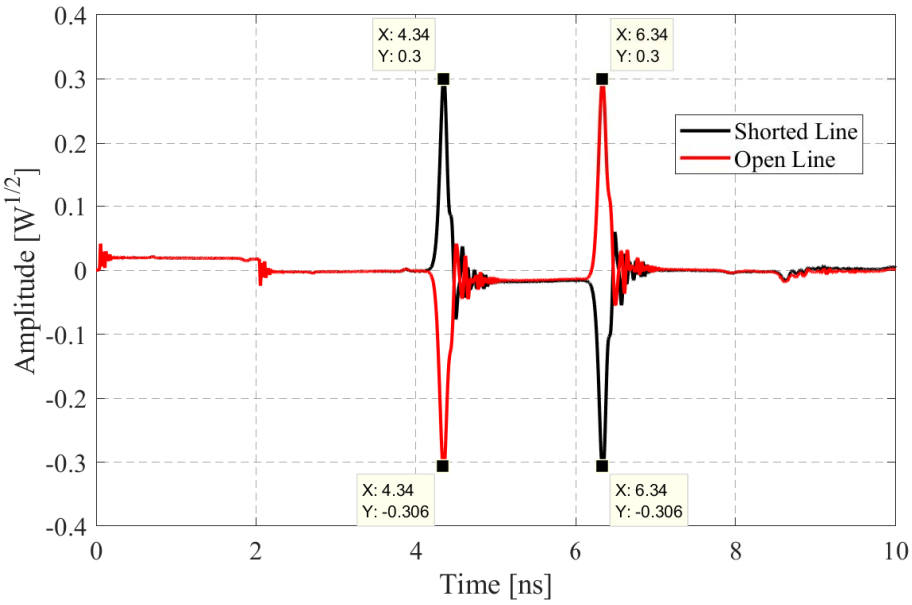

(b)

Figure 4.22: (a) A unit square-wave input pulse with T-hold of 2 ns (b) Balanced output signals when the final and optimized model in Figure 4.14 is simulated at 6 GHz.

Figures 4.21 (b), 4.22 (b), and 4.23 are the coupled output signals when a unit Gaussian, square-wave and step input pulses are defined on the final CST model, respectively. The derivative of the Gaussian pulse (Figure 4.21 (a)) on the primary line is what is seen as sinusoidal-type double pulse on the secondary lines (Figure 4.21 (b)). In order to separate the sinusoidal-type waveform, an input square-wave pulse becomes the natural option because it allows one to assign the value of T-hold. It is a timing definition of how further

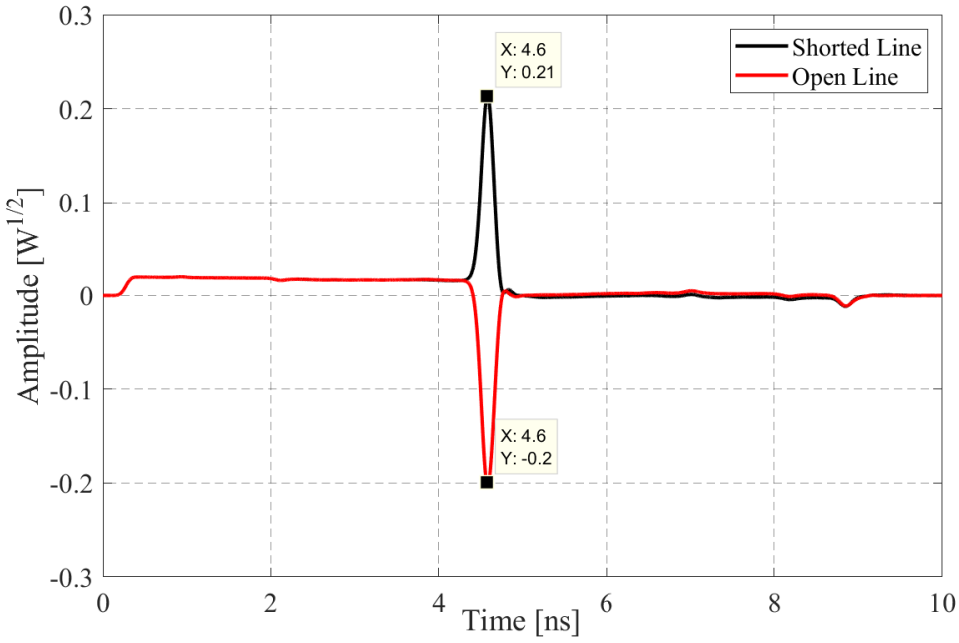

Figure 4.23: Balanced output pulses with opposite amplitudes obtained with the optimized CST model in Figure 4.14 at 6 GHz.

apart the immediate corresponding output pulses are separated (refer to Figures 4.17 and 4.22 for comparison). In addition, if the desired output is a single pair of pulses with opposite amplitudes as in Figure 4.23, then a step input pulse in Figure 4.18 (a) is defined. With all the three types of input pulses tested with the final model, the results indicate minimum NEXT and well balanced output pulses (FEC) as shown in Figures 4.21 (b), 4.22 (b) and 4.23.

An additional important factor to consider is the effect of rise time on the magnitude of the coupled output pulses with regard to FEC. As an example, the T-rise for the square-wave pulse used in the simulation is 0 ns while that of the step-pulse is 0.133 ns. The comparison of their corresponding output pulses (FEC) show that there is more coupling for shorter T-rise (Figure 4.22 (b)) than for a longer T-rise (Figure 4.23).

In Figures 4.24 and 4.25 we show the cross-section of the balun structure of Figure 4.14 and the field distribution around it. A closer view of Figure 4.24 shows visible E-field lines into port 2 and out of port 3; a clear implication that the two output ports have opposite polarity potentials. The fields outside (in free space) weaken as they move away from the structure but can still cause some problems to the antenna. Therefore, they must reside within an enclosure as described in the subsequent chapter. As expected the primary conductor which is excited through port 1 shows high field intensity as compared to the two coupled secondary conductors.

Considering the requirements for the final trifilar balun we achieve the following: a low

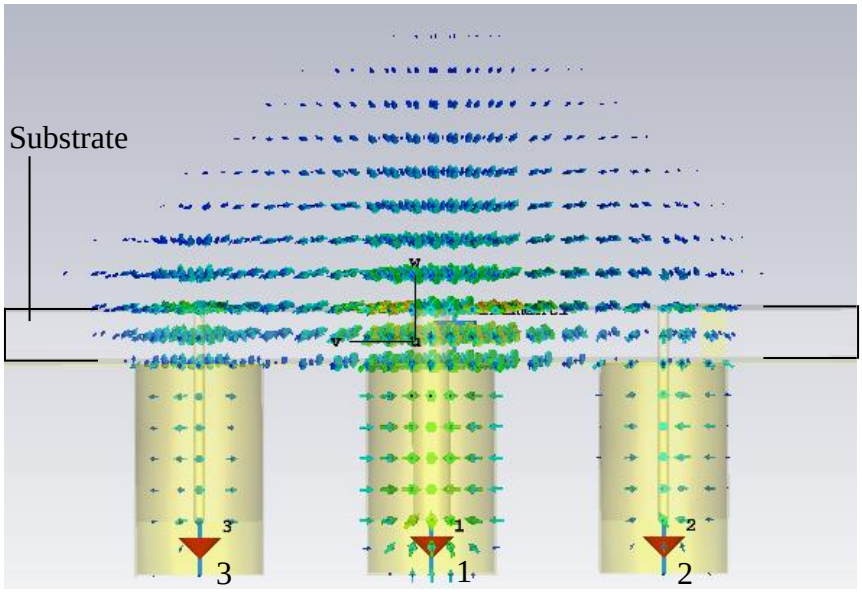

Figure 4.24: Cross-sectional view of the CST computational model of the final balun with E-field pattern.

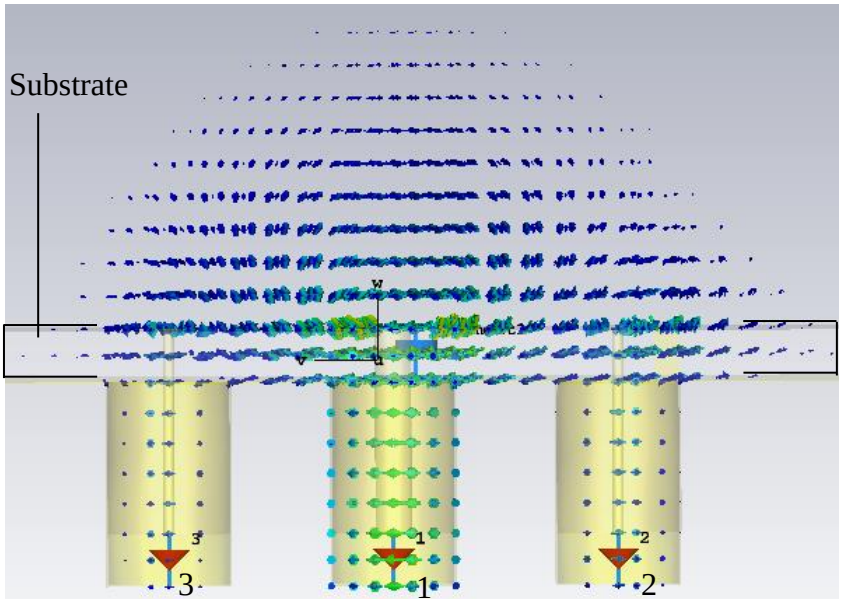

Figure 4.25: Cross-sectional view of the CST computational model of the final balun with H-field pattern.

loss material (Rogers RO4003C) and the required line impedances (100 ohms) (subsection 4.4.1), in sub-subsections 4.4.3.1 and 4.4.3.4 we obtain balanced output signals with less NEXT, the requirement of low cost balun through the elimination of expensive chokes and RF cables is described in sub-subsection 4.4.3.2. However, the HB characteristics of the fabricated balun is discussed in the subsequent chapter which concludes the final phase of the design process in the flowchart in Figure 4.6.

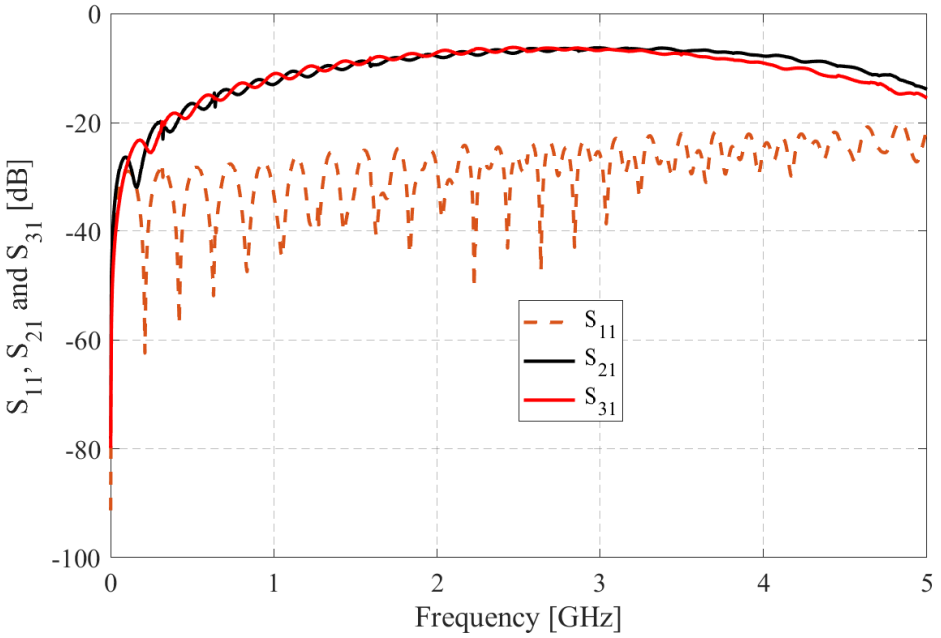

(a)

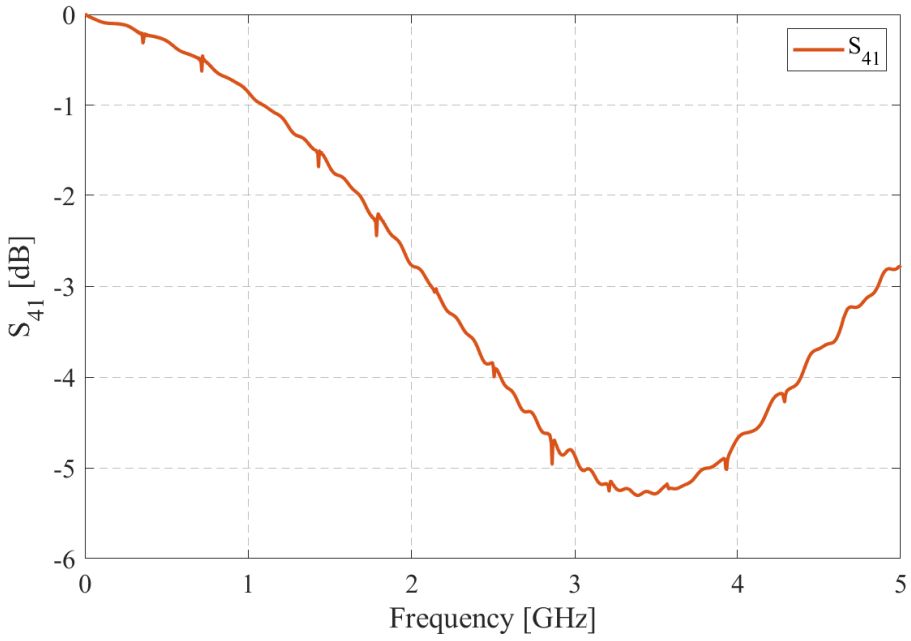

(b)

Figure 4.26: (a) Simulated results of the differential transmission (S_{21} and S_{31}) and the reflection coefficient (S_{11}) of the trifilar coupled-line balun (b) Transmission parameter, S_{41}, indicating the energy transmission between the input port 1 and the termination load (port 4) in the primary conductor.

4.4.4 Frequency Domain Response of the Trifilar Balun

Figures 4.26 and 4.27 are used to analyse the frequency domain response of the final trifilar coupled-line balun. The results are obtained from the same CST model already discussed

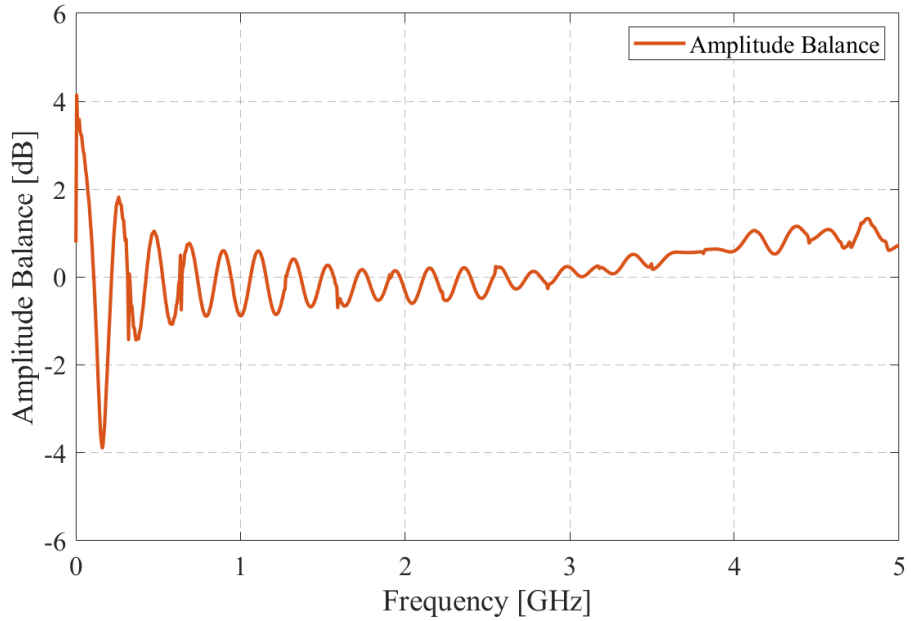

(a)

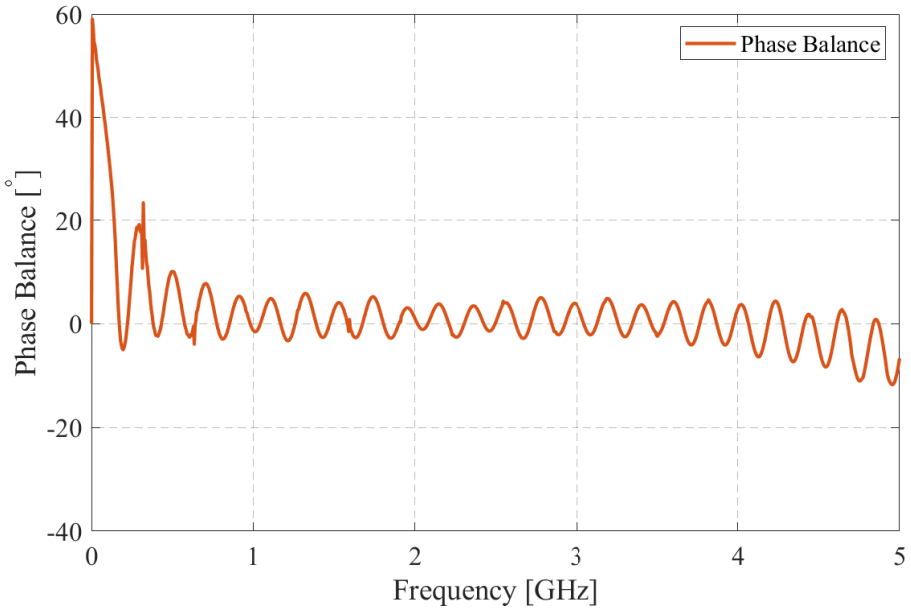

(b)

Figure 4.27: (a) Amplitude balance of the simulated trifilar coupled-line balun (b) Phase balance of the simulated trifilar coupled-line balun.

in the previous subsections of this section. From Figures 4.26 (a) it can be seen that the unbalanced input port of the primary conductor is well-matched under -10 dB over the entire frequency band. This implies that most of the power is transmitted within the primary line and less of that power is reflected back into the input port. In addition, the differential transmissions, S_{21} and S_{31}, show that the input power is split almost equally (by the structure) between the two output ports. At the lower end of the frequency spectrum

(below 1 GHz), most of the energy is absorbed by the termination load (Figure 4.26 (b)), and less of the energy is coupled into the secondary lines (see S_{21} and S_{31} of Figure 4.26 (a)). The structure attains maximum coupling between 2 GHz to 3.75 GHz and it is the region with very close balanced output energy (refer to transmission parameters in Figure 4.26 (a)). With the default stimulated power being 0.5 W or -3 dB (Figure A.6, appendix A.1), the plot in Figure 4.26 (b) can be used to determine the maximum power loss in the load as -3 dB and the minimum as $\approx$ -8.3 dB. In general, a higher differential transmission and lower reflection coefficient means more energy available for coupling and possibly an improved dynamic range and less signal distortion in the coupled structure.

The amplitude and phase balance are given in Figure 4.27 (a) and Figure 4.27 (b), respectively. The phase balance refers to how closely the coupled output signals in the secondary traces are to 180° out of phase with each other, and the units are given in degrees. The amplitude balance is a measure of how the magnitude of the coupled output energy are closely matched and is expressed in decibel (dB). The graph in Figure 4.27 (a) shows that the amplitude balance of the trifilar balun is within $\pm$1.7 dB for frequencies above 165 MHz. Also, from 300 MHz towards the higher frequency band, the phase balance is within $\pm$10° (Figure 4.27 (b)). The large ripples in the lower end of the spectrum (Figure 4.27), can be linked to in-band common-mode resonance which causes the high imbalance (phase and amplitude) in the structure. Both phase and amplitude balance are determined by the quality of coupled-line structure as well as the construction and line matching. The trifilar coupled-line balun qualifies in this regard, hence has better frequency response from as low as 300 MHz.

4.4.5 Final Design of the Fabricated Trifilar Balun

A fabricated final balun of the exact computational model in Figure 4.14 is shown in Figure 4.28. The fabrication of the balun structure is done on a double-sided Rogers 4003C PCB board which has copper conductors. Altium designer tool is used to design the PCB and to generate the necessary Gerber files for etching. The implementation and testing of the fabricated balun is carried out together with the IRA as a unit (see chapter 5) because the spacing between the traces is not sufficient to connect SMA connectors as initially illustrated with the first prototype in Figure 4.8 (b). Moreover, without the connectors, it is not possible to experimentally test the prototype balun exclusively. Nonetheless, having successfully validated the initial model of the trifilar balun, and done the rigorous computational analysis of the final design, we have confidence in our fabricated balun to improve the performance of the IRA as intended.

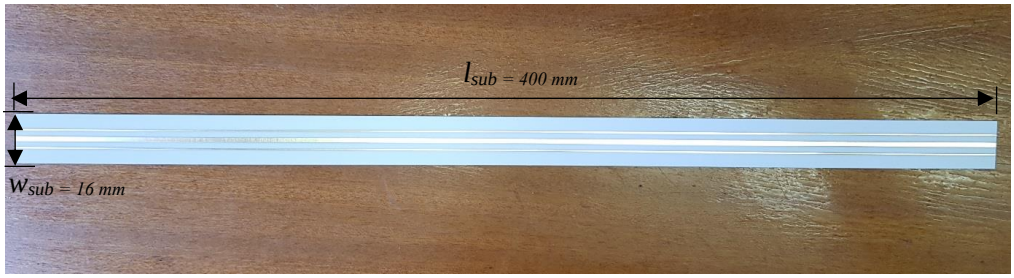

Figure 4.28: A photo of the exact fabricated balun of the final CST model in Figure 4.14.

4.5 Summary

A coupled transmission line concept is used to develop an HB trifilar balun for an IRA antenna. The initial prototype is successfully verified using the CST computational model and AWR design tool. The final model is thoroughly tested in CST to minimise undesired NEXT for balanced FEC output signals. The FEC is improved through a non-uniform configuration of an edge-coupled structure, shorter rise time and increased coupling length. In the latter case it allows the balun to be used as a transmission line, hence no need for expensive RF coaxial cables that are usually required for matching and electrical connections between an IRA and a balun. This further eliminates the need for expensive chokes normally used to reduce common-mode currents on the RF cables. The frequency domain analysis using simulation results indicate a good response of the trifilar balun with low reflections on the unbalanced input port, high differential transmission on the output ports, phase balance within $\pm 10^{\circ}$ and amplitude balance within ± 1.7 dB in most part of the frequency spectrum.

The final coupled-line balun with the required line impedances is fabricated on a thin Rogers 4003C material. The following task is to add the necessary electrical components to the balun and to assemble it together with the IRA. This is carefully described in the next chapter including testing of the optimised IRA and other related simulation work.

—As often happens in the history of science, the simple ideas are the hardest to achieve: simplicity does not come of itself but must be created —

—Clifford Truesdell, 1960 —

CHAPTER 5

Optimisation of the Final IRA Design

The final design of the impulse radiating antenna (IRA) is described in this chapter with the required conical plates for a 200-ohm differential input impedance. First-off, a computational electromagnetic (CEM) model of the IRA is created in FEKO and tested without the new trifilar coupled-line balun in chapter 4. However, the characteristics of the input signals used in the simulation is similar to the output-excitation signals of the trifilar balun. The advantage of excluding the balun is to have a simplified test-model for making predictions on the performance of the IRA within shorter simulation runs. Our simulation results are compared to the ones from the initial IRA design in [13].

Secondly, the trifilar coupled-line balun in CST is imported into FEKO and assembled together with the designed IRA for further testing and optimization. Finally, the optimised-IRA is constructed and used to verify the exact optimised-CEM model which can be used to do further simulation work.

5.1 Computational Modelling

The modelling of IRA in FEKO starts with the reflector whose diameter, D, and depth, d, are known parameters. Their values are measured directly from the existing reflector in Figure 2.9 (b) while the focal length, F, is approximated through equation (2.23). The

next step involves the creation of the conical plates and other components such as the termination loads and excitation ports. The following are some of the considerations for creating the final IRA model.

- Characteristics of the material: Parts of the structure which are metallic are considered perfect electric conductor (PEC). The application of PEC is very common in CEM techniques, especially with pilot models. The improved fidelity obtained with a lossy metal is offset by faster simulation runs with a PEC material where the terms which account for finite conductivity are ignored. Also, we assume that within the frequency band of interest for characterising the IRA and for better performance, the effect of excluding lossy properties is negligible.
- Metal plate thickness: The default thickness (infinitely thin) is applied for the PEC sheets including the conical plates and the reflector. This is an additional way of simplifying the model (by reducing mesh size) to speed up the simulation.
- Termination loads: Edge ports with matching loads are used to terminate the feed arms on the parabolic dish (Figure 5.4 (a)). An edge port gives a better representation of a matching circuit constituting multiple resistors that are connected in parallel for even distribution of charges. Secondly, the errors associated with wire segments for wire ports are avoided during the discretization of the model. Finally, the edge port geometry is closer to the actual configuration of the termination loads.

5.1.1 Designing the Launcher Plates

Table 5.1 gives a summary of the parameters used to design a test-model for the final IRA. Most of the parameters are linked to the feed arms and we briefly describe how they are determined. The modelling of the conical plates is guided by mathematical equations (2.24)–(2.27) in chapter 2, section 2.5, sub-section 2.5.2. The equations are implemented in FEKO by parameterising the values for the independent variables on the right-hand side of the equal sign. The advantage of parameterisation is that it is easy to modify the structure without unforeseeable complications with the model. The structure parameters $(\beta_0, \beta_1, \beta_2,\ a, b_1, b_2, D, F)$ define a particular conical TEM line that gives the desired feed impedance, in this case, 200 ohms. Starting with a known characteristic impedance of the line, $\eta_0 f_g$ (refer to section 2.5), the ratio of b_1/b_2 in equation (2.25) is determined through the following mathematical relations:

$$f_g = \frac{K(m)}{K(m-1)} = \frac{K(m)}{K'(m)} \tag{5.1}$$

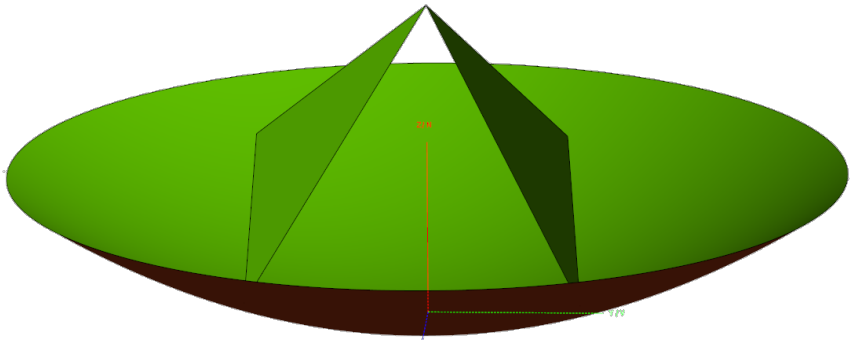

Figure 5.1: Parabolic reflector of the IRA and the first pair of conical TEM feed arms.

$$m^{1/2} = \frac{b_1}{b_2} \tag{5.2}$$

where f_g is the geometric factor described in sub-section 2.5.2, $K(m)$ is the complete elliptic integral of the first kind, and the parameter m can be found through equation (5.1) and Table 17.3 in [80], which presents the argument $K'(m)/K(m)$ as a function of m. Having established the relevant variables in FEKO, the first pair of conical plates are created as shown in Figure 5.1. The second pair of the plates is constructed through *copy and mirror* function available in the simulation tool. Since all the four arms converge at the focal point of the dish, a feed gap must be created in order to have space for the excitation ports.

Table 5.1: Design parameters for the test model of IRA. The F/D ratio applied is 0.38 and Z_{line} is 200 ohms.

Parameter	Value (mm)	Parameter	Value (°)
Diameter, D	850	β_0	47.29
a	451.09	β_1	45.31
b_1	415	β_2	49.19
b_2	490.31	φ_0	60

5.1.2 Modelling the Feed Gap

It can be tempting to define the feed gap by translating the geometry of the plates as shown in Figure 5.2 (a). However, this changes the orientation of the feed arms from the principal focus and can lead to infinitesimally small changes in the model that compromise the fidelity of the meshed structure. The gap is formed by truncating the plates at the feed gap as illustrated in Figure 5.2 (b). It is the most realistic method of creating the gap while maintaining the original orientation of the radial lines towards the focal point of the

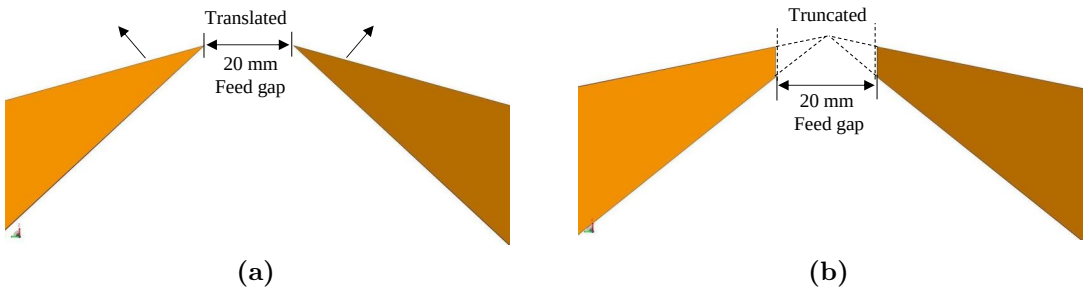

Figure 5.2: (a) Creating the feed gap by translating the feed arms apart ot (b) truncation of the feed arms at the principal focus of the reflector in order to form the feed gap.

dish. The size of the gap is chosen based on the minimum diameter of the metallic tube used in enclosing the trifilar balun. It is obvious that the position of the feed will shift irrespective of the procedure applied in defining the feed gap. But how does this affect the performance of the IRA?

An antenna design tool known as Antenna Magus is very useful during the antenna design process before the actual modelling, analysis and optimisation of an antenna in FEKO, CST or AWR microwave office. We utilize its functionalities to project the antenna gain pattern of the IRA for various feed positions, F, F', F'' and F'''. The database for the Antenna Magus has over 350 antennas to be explored, however, IRA antenna is not one of them. As an alternative, a horn-fed parabolic reflector antenna from the database is used to make the projections. The antenna is designed for a constant dish diameter, 850 mm, and F of 320 mm. The default dimensions for the horn antenna are applied and we run the simulation at 4 GHz.

Figure 5.3 shows the radiation pattern in a Cartesian plot of a horn-fed parabolic reflector antenna for different feed positions relative to F. The negative sign is taken as the direction towards the dish with F being the point of reference while the positive is the direction away from the dish relative to F. The predictions indicate that the peak gain at angle 0° is approximately 29 dBi at 4 GHz. Also, the relative position of the feed does not lead to a major change in the bore-sight gain of the antenna (refer to Table 5.2 which has the gain

Table 5.2: The gain results of a horn-fed parabolic reflector antenna with reference to Figure 5.3.

Feed position (mm)	Position relative to F (mm)	Gain (dBi)
F = 320	0	29.62
F' = 300	-20	29.33
F'' = 340	+20	29.82
F''' = 371	+51	29.87

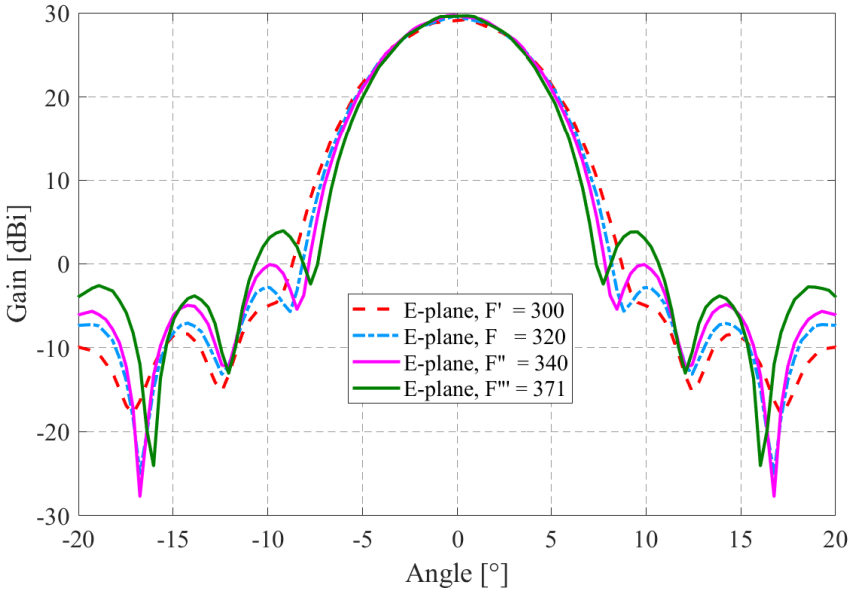

Figure 5.3: Radiation pattern of a horn-fed parabolic reflector antenna for various feed distances, at 4 GHz frequency.

values as extracted from Figure 5.3). However, it can lead to the growth of the side-lobe levels which can introduce additional artefacts to the experimental data. The relative position of the feed (negative direction) means most part of the energy is focused on the central region of the dish, hence less spillover and more illumination loss. Whereas in the positive direction most part of the dish is illuminated and there is also increase in the spillover loss which can be the source of the sensitive side-lobes. In general, creating the feed-gap will lead to shifting the position of the feed relative to the F of the IRA but does not drastically change its gain. The actual F of the IRA is 320.26 mm, thus a truncation of the feed arms that shifts the feed position by ± 25 mm will ensure that the side-lobes are contained (Figure 5.3). Finally, the first CEM model of the IRA is implemented in FEKO and characterised in FD as presented in the next subsection.

5.1.3 CEM Model of the Final IRA Without the Trifilar Balun

In order to simply test the concept of the balanced feed, the trifilar balun is not required at this stage, hence the procedure of importing the balun from CST and re-meshing the structure is avoided. From early design considerations in this section and the test results from Antenna Magus, we confidently design and discretise the CEM model in Figure 5.4 (a) in the method of moments (MoM) code FEKO. Each of the four edge ports terminating the conical plates on the reflector are defined as 200 ohms. A metallic rod passing through the axial symmetry is used to connect the input ports and the ground plane (reflector).

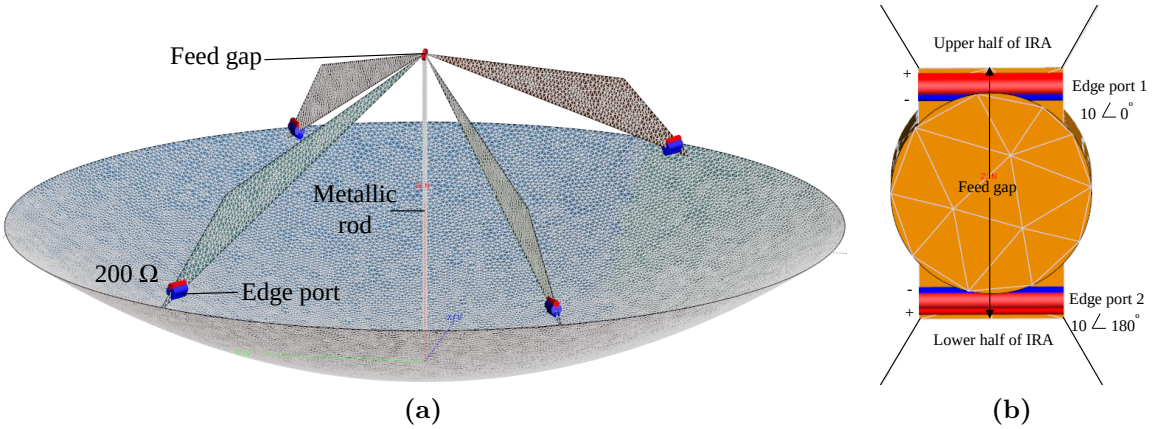

Figure 5.4: (a) Four arm discretised CEM model of the final IRA without a balun (b) Front view of the feed gap showing the two excitation edge ports 1 and 2 connected to the metallic rod and the upper and lower conical plates.

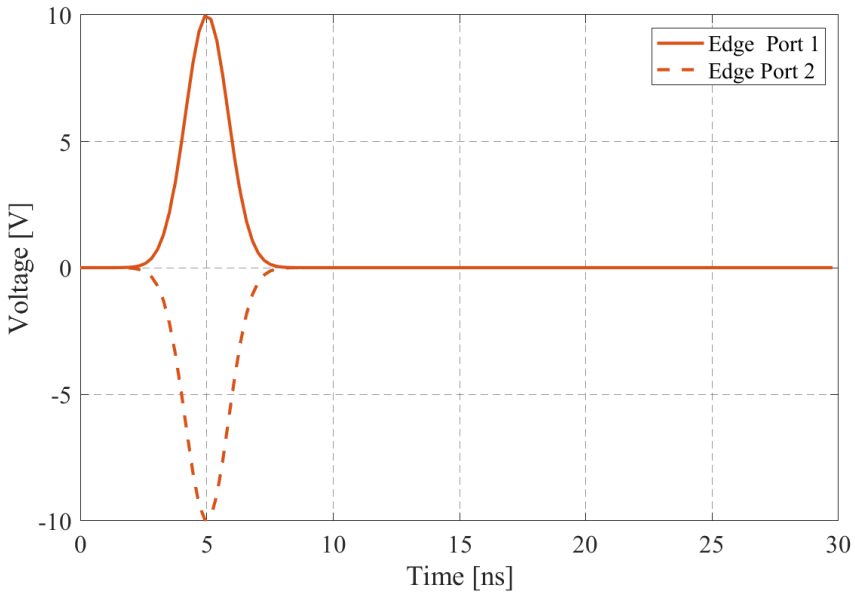

Figure 5.5: TD pulse representation of edge ports 1 and 2 with equal magnitude but opposite sign.

There are two edge ports 1 and 2 at the feed gap as given in Figure 5.4 (b) with 100 ohm impedance assigned to each port for a differential input impedance of 200 ohms. The magnitude of each voltage source is 10 V while the sign for the voltage source 2 (from edge port 2) is negative so that the two pulses are of equal amplitude but opposite polarity as given in Figure 5.5. The pulses from edge port 1 and 2 excite the upper and lower plates of the IRA, respectively.

The discretised model in Figure 5.4 (a) has 48,309 discrete triangles and it takes approximately 2.35 hours for a complete single frequency simulation run at the South African Centre for High Performance Computing (CHPC) in Cape Town. The CHPC consists

of the Lengau cluster which has a CPU clock of 2.6 GHz, 1368 compute nodes with 24 cores (32832 CPU cores) and a total of 148.5 TB of random access memory (RAM) [81]. Due to the large electrical size of the model, a RAM of 125 GB and a maximum of 12 cores are allocated for our job. Thus, only 51 frequency points are simulated within a frequency range of 10 MHz–4 GHz. We request for the far-field and compare with the results from the original CEM model in [13] (Figure 3.11 (a)). The highest frequency (4 GHz) is limited by the computational power available (allowable) at the CHPC for a single job submitted. For the original CEM model, an upper frequency limit of 4 GHz is chosen as the model is simulated on a high performance computer (HPC). The HPC has less computational power than the CHPC. The HPC has a total RAM of 512 GB and two CPUs each capable of handling 24 parallel processes. A single simulation run using 6 parallel processes on one CPU takes approximately 7 GB of memory for an hour runtime. When the CHPC and HPC are not available, a local machine, an Intel(R) Core (TM) i7-3770 CPU with 16 GB of RAM is utilised. Therefore, most of the CEM models are discretised up to an upper frequency of 4 GHz.

The comparison of the bore-sight far-field gain and the reflection coefficient between the CEM model of the original IRA and the final IRA without the trifilar balun (test model) are given in Figures 5.6 and 5.7, respectively. At 4 GHz, the gain of both models is 25 dBi (Figure 5.6) with the difference being within 5 dB compared to the estimations from the horn-fed parabolic reflector antenna in Figure 5.3. The test model of the new IRA has a slightly better gain than the original IRA design and the difference is within 3 dB above 1 GHz frequency. Also, from Figure 5.7 the test model has S_{11} being below -10 dB across the frequency band whereas the S_{11} for the original model is worse on the lower end of the frequency band (below 2 GHz). The improved performance of the test model of the new IRA is attributed to the well balanced feed and thinner arms which are properly terminated on the reflector.

Further analysis on the test model and the original IRA model is performed by plotting their normalised far-field radiation pattern at frequencies (a) 1 GHz, (b) 2 GHz and (c) 4 GHz as shown in Figure 5.8. The main lobes project in the positive z-axis while the back lobes in the negative z-axis. It can be seen from the plots that the back lobes of the original IRA design are much more pronounced at the back of the reflector in comparison to the ones from the test model. Such excessive back lobe radiation can cause interference to nearby equipment (for example, a source generator or spectrum analyser) which is usually placed behind the antenna during measurements.

In general, there is improved performance with the test model of the new IRA over the original IRA design. Considering the practical implementation of the new IRA design, it

is not practical to feed the IRA as illustrated in Figure 5.4 (b). Therefore, the use of the trifilar balun discussed in the previous chapter is required to deliver balanced input pulses such as in Figure 5.5.

5.1.4 CEM Model of the Final IRA With the Trifilar Balun

The CEM model of the final IRA without a balun (Figure 5.4 (a)) is implemented in FEKO together with the final model of the trifilar coupled-line balun in chapter 4. Since the trifilar balun is designed in CST, it is imported into FEKO and placed inside a metallic enclosure of equal length (400 mm) as shown in Figures 5.9 and 5.10. The enclosure provides mechanical support for the balun as well as shielding of the undesired EM fields in free space as described in the previous chapter, sub-subsection 4.4.3.4. The combined structure of the balun and the enclosure replaces both the metallic rod and the edge ports at the feed gap given in Figure 5.4. The central placement of the balun as in Figure 5.10 maintains the symmetry when the connections are made between the secondary lines and the feed arms, which in turn leads to a balanced feed.

The shielding enclosure has an inner diameter of approximately 20.1 mm and a thickness of 1 mm. It is the minimum diameter such that the enclosure does not affect the required coupled output signals which are initially calculated without the presence of a shielding material. The diameter of the metallic tube also determines the size of the feed gap that must be created as discussed in subsection 5.1.2. It should be noted that other component

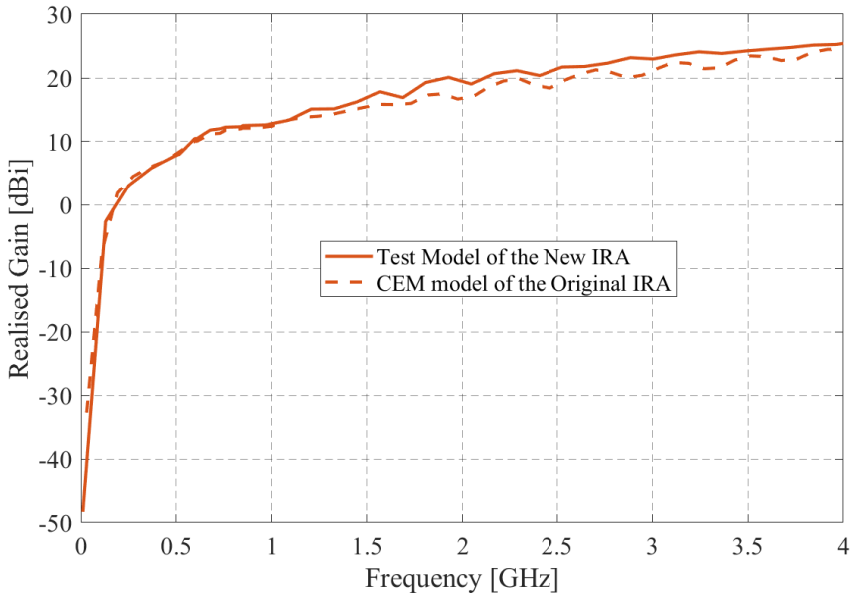

Figure 5.6: Comparison of the bore-sight far-field gain between the CEM model of the original IRA and the test model of the new IRA.

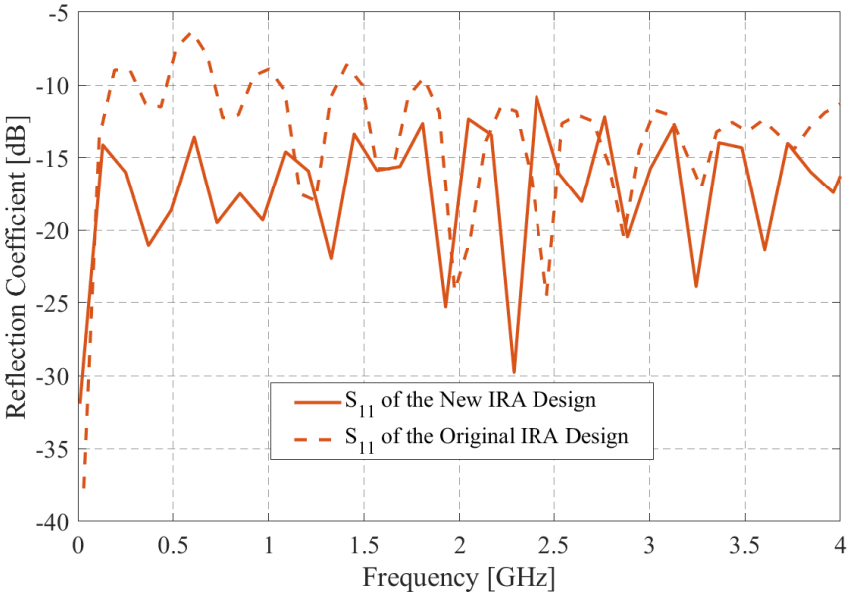

Figure 5.7: Comparison of the reflection coefficient between the CEM model of the original IRA and the test model of the new IRA.

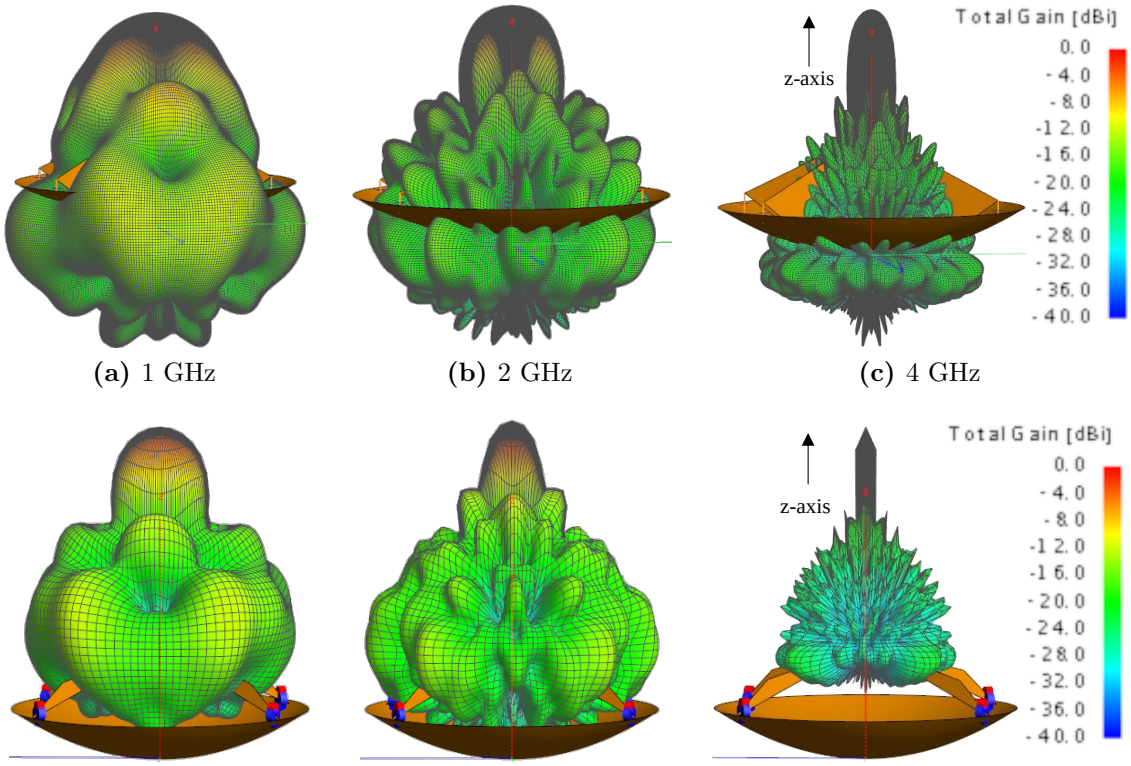

(a) 1 GHz **(b)** 2 GHz **(c)** 4 GHz

Figure 5.8: Comparison of the normalised far-field radiation pattern of the original CEM model of the IRA (top plots of (a)–(c)) and the test model of the new IRA (bottom plots of (a)–(c)) at frequencies (a) 1 GHz, (b) 2 GHz and (c) 4 GHz.

parts used to connect the dish (IRA) to the rotating tripod stand are permanently attached to the tripod. Therefore, the length of the balun, 400 mm, is the maximum length chosen to the extent that there is sufficient spacing, e (see Figure 5.9), to make the cable connection to the balun.

A Styrofoam material is added to the structure (Figure 5.10) to hold the balun in position. Its dielectric constant (1.03) is sufficiently close to that of air (1), hence it does not interfere with the coupling mechanism within the balun structure and the enclosure. In addition, care has to be taken to ensure that the short wire connections between the secondary lines and the plates are slightly below the upper side of the balun. The upper side (space) in Figure 5.10 is where more of the fields reside (refer to Figures 4.24 and 4.25) and can couple directly into the wires and cause imbalance. The ground plane of the balun and the cable feed are on the lower space of the enclosure where less or no fields reside. Thus, all the electrical connections and ground terminations are done on the lower side of the balun structure.

After unioning all the parts of the the model, a coarse mesh and MoM code are applied in FEKO with the highest frequency limited to 4 GHz for faster simulation runs. The voltage source at the cable feed is set as 10 V with a port impedance of 50 ohm so that the entire primary line is perfectly matched (refer to sections 4.3 and 4.4 of the previous chapter). Finally, optimisation parameters are defined before running the FEKO solver.

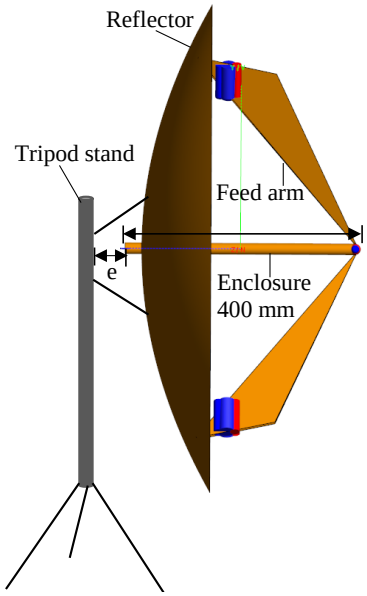

Figure 5.9: A diagram of the final IRA attached to a tripod stand. The trifilar balun is placed inside the metallic enclosure for shielding and mechanical support.

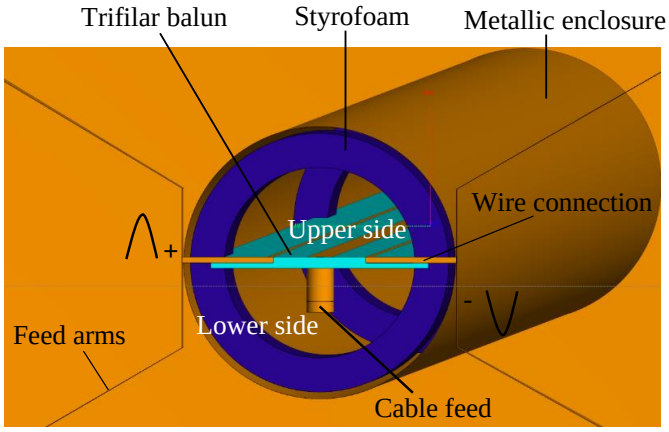

Figure 5.10: Zoomed view of the front section at the feed gap of Figure 5.9 showing the trifilar balun inside an enclosure.

5.1.4.1 Setting Optimisation Goals

The various optimisation methods in FEKO are summarised in appendix A.1, Table A.1. The Genetic algorithm (GA) method is chosen for its robust and high accuracy capabilities as well as handling multiple optimisation goals simultaneously [82]. We set the optimisation parameters linked to the size (or impedance) of the plates, a and b_1, impedance at the termination ports, Z_{line}, and the S_{11} parameter.

The estimated time for a single optimisation run is 1.93 hours and it takes 81 runs in an Intel(R) Core (TM) i7-3770 CPU, RAM of 16 GB, for the solver to reach the optimisation goal. The plots in Figures A.1–A.4, appendix A.1, show the optimised values for the variables as a = 440.6 mm, b_1 = 381.8 mm, Z_{line} = 195 Ω and S_{11} = -11.46 dB. After the optimisation process, the optimised parameters and the associated parameterised variables are automatically implemented including changes in the dimensions of the CEM model. The optimised FEKO model (Figure 5.11) is re-discretised in the MoM code for current and far-field requests. The simulation results are analysed in sub-subsection 5.1.4.2 as follows.

5.1.4.2 Analysis of Simulation Results

The normalised far-field pattern of the optimised model of the final IRA at frequencies (a) 1 GHz, (b) 2 GHz and (c) 4 GHz are presented in Figure 5.12. Of particular note is the fact that the optimised IRA model has significantly reduced back lobes compared to the back lobes of the original model already given in Figure 5.8. The key contribution of the minimised back lobes in the optimised CEM model is the trifilar balun which improves the balanced feed structure of the IRA.

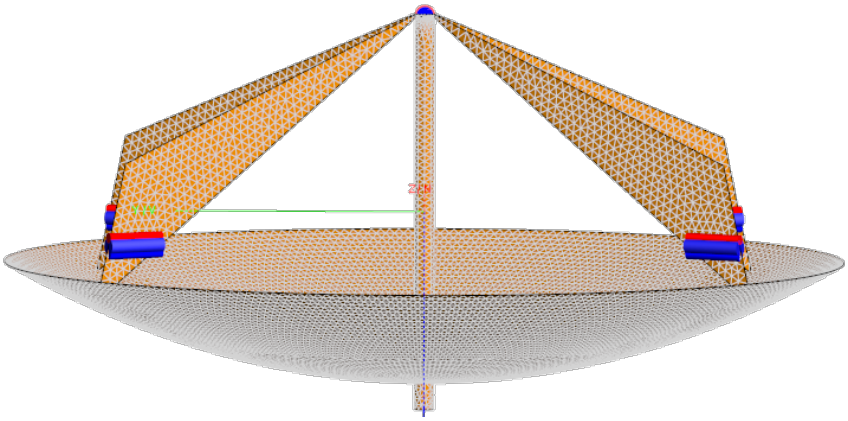

Figure 5.11: The optimised CEM model of the final IRA.

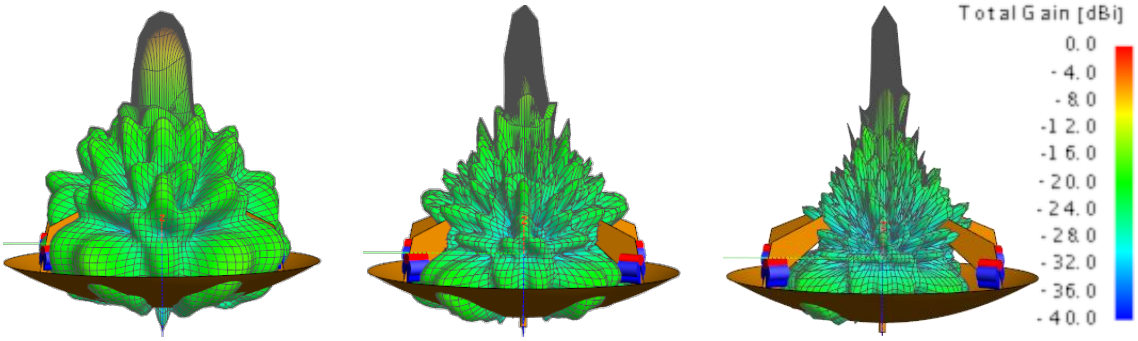

(a) 1 GHz **(b)** 2 GHz **(c)** 4 GHz

Figure 5.12: The normalised far-field radiation pattern of the optimised CEM model of IRA at frequencies (a) 1 GHz, (b) 2 GHz and (c) 4 GHz.

Figure 5.13 shows the simulated surface current distribution on the parabolic dish of both the original and the optimised IRAs at frequencies (a) 1 GHz, (b) 2 GHz and (c) 4 GHz. It can be observed from the top plots of (a) to (c) in Figure 5.13, that the current density in the original IRA is concentrated around the centre of the aperture and dominates along the x-axis, especially at 4 GHz. On the other hand, the optimised trifilar-balun fed model shows a more uniform current distribution (Figure 5.13 (bottom plots of (a) to (c))), than the original IRA design. Therefore, for the original IRA model, the H-plane beam-width (BW) is narrower than the E-plane BW (Figure 5.14 (a) and (b)). Whereas for the optimised CEM model, the E-plane and H-plane BWs are equal as illustrated in Figure 5.14 (c) and (d). A uniform aperture field radiates uniformly hence the far-field pattern is symmetrical, i.e., the BWs in the H- and E-planes are similar. The trifilar coupled-line balun ensures balanced currents in the structure of IRA resulting in a symmetrical aperture. The uneven distribution of currents (non-uniform aperture fields) in the traditional IRA designs has been reported in [41, 45], but the proposed feeding configuration (Vivaldi fed IRA) for uniform aperture fields is based on simulations and

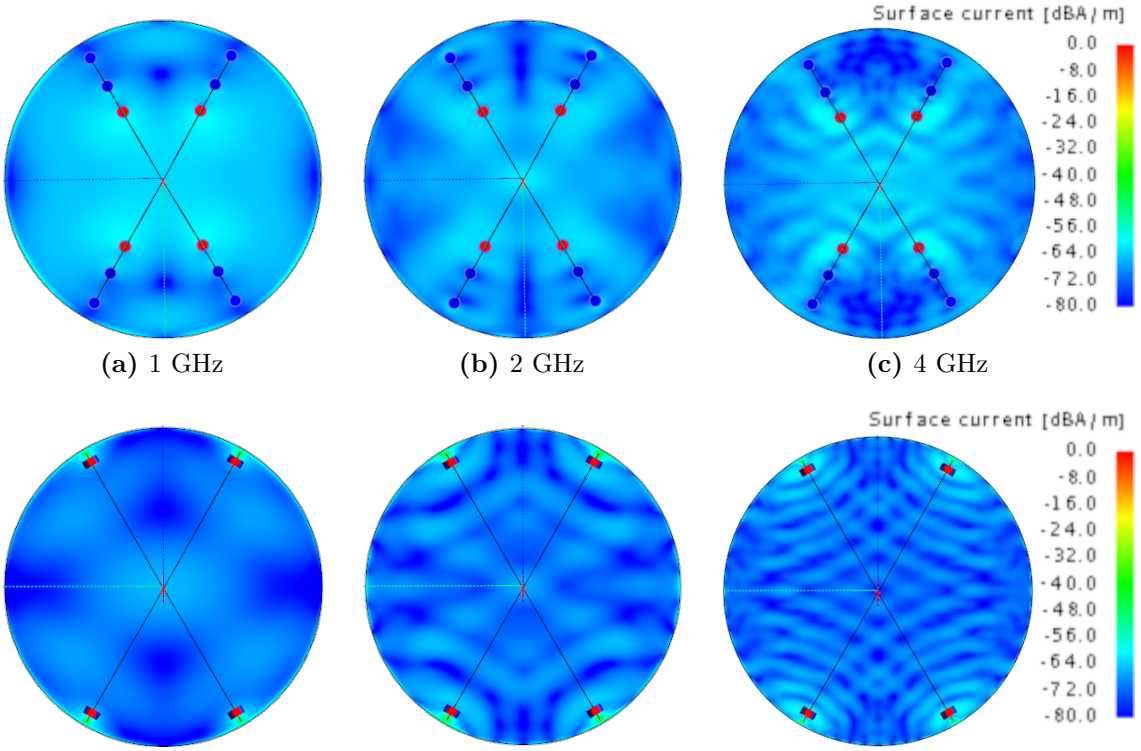

(a) 1 GHz **(b)** 2 GHz **(c)** 4 GHz

Figure 5.13: Comparison of the simulated current distribution of the original CEM model of the IRA (top plots of (a)–(c)) and the CEM model of the optimised IRA (bottom plots of (a)–(c)) at (a) 1 GHz, (b) 2 GHz and (c) 4 GHz.

require further investigation for optimum design [45].

In Figure 5.15 the side lobe level (SLL) in the H-plane of the optimised IRA model is 5.8 dB less than the SLL of the original IRA model at 4 GHz frequency. The SLL is defined as the measured beam strength of the first side-lobe with reference to the maximum beam strength. This definition only includes the first side lobe because it is the major source of electromagnetic interference (EMI) compared to other side lobes. The SLL of the optimised IRA in the E-plane is 3.8 dB less than that of the original IRA model at 4 GHz (Figure 5.16). The reduced SLL in the H- and E-planes of the optimised FEKO model is due to the uniformity of the aperture fields. It is not possible to eliminate the SLLs completely, thus their reduction is desirable in most antenna applications.

Figure 5.17 demonstrates the scattering of the co-polar component, E_θ, at E-plane for the optimised CEM model of IRA. For each frequency component the magnitude of E_θ is normalised to its own maximum. The E-plane component is similar to the one in the H-plane as already demonstrated in Figure 5.14 (c) and (d). It can be seen from Figure 5.17 that with increase in frequency the BW becomes narrower and the E-field (E_θ) strength increases at the bore-sight of the IRA. At 2 GHz the half power beam width (-3 dB) is

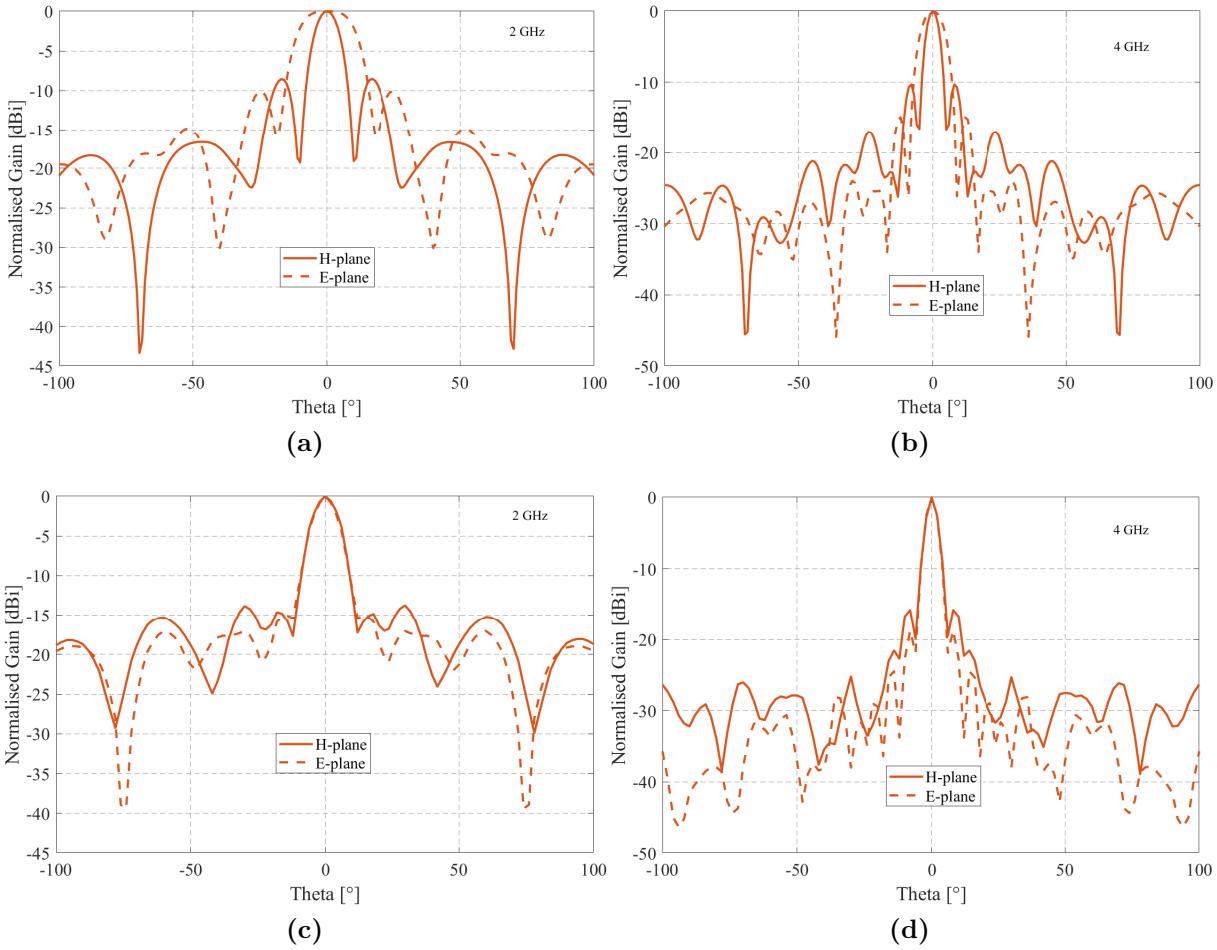

Figure 5.14: E-plane and H-plane far-field patterns of the original IRA model at (a) 2 GHz and (b) 4 GHz compared with the E-plane and H-plane far-field patterns of the optimised IRA model at (c) 2 GHz and (d) 4 GHz.

9.4° and at 4 GHz it is 4.5°.

The linear and inverse relationship of the far field (E_θ) strength and BW with frequency, respectively, are the characteristics of a symmetric aperture for an ideal IRA [41]. Hence, the balanced feed system used in our optimised IRA ensures proper feeding of the IRA. This leads to a uniform aperture field and a far-field zone E_θ-pattern whose direction at the bore-sight is unaltered across the frequency range and the strength is linearly related to frequency (Figure 5.17). Following the detailed discussion of the optimised FEKO model is the analysis of the gain and efficiency of the optimised IRA and the original IRA models (subsection 5.1.5). Lastly, we discuss the fabrication and characterisation of the optimised IRA in section 5.2 and thereafter give a summary of the main points of the chapter in section 5.3.

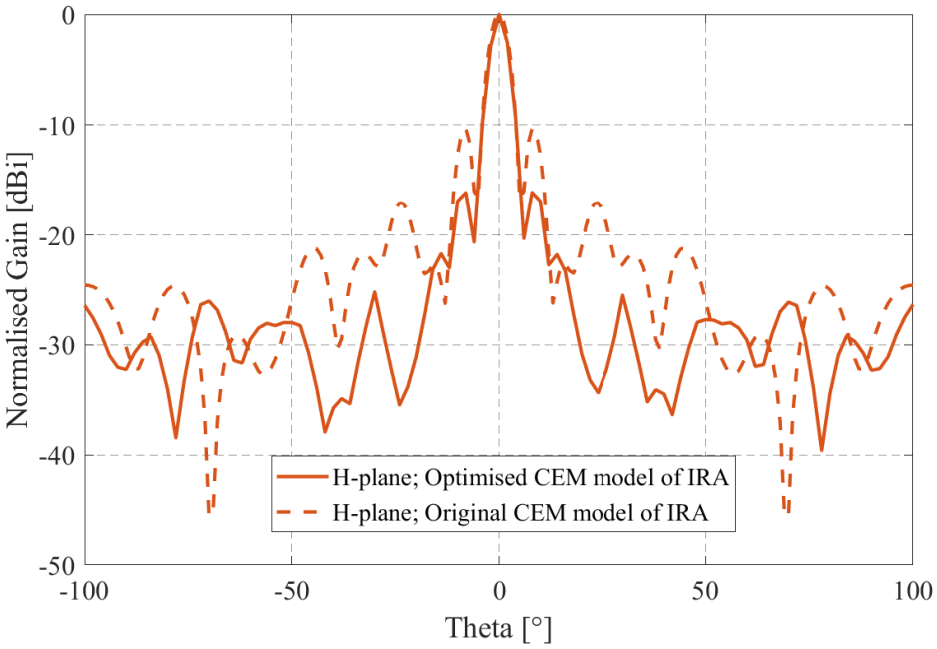

Figure 5.15: Comparison of the H-plane far-field pattern between the optimised CEM model of IRA and the original CEM model of IRA at 4 GHz.

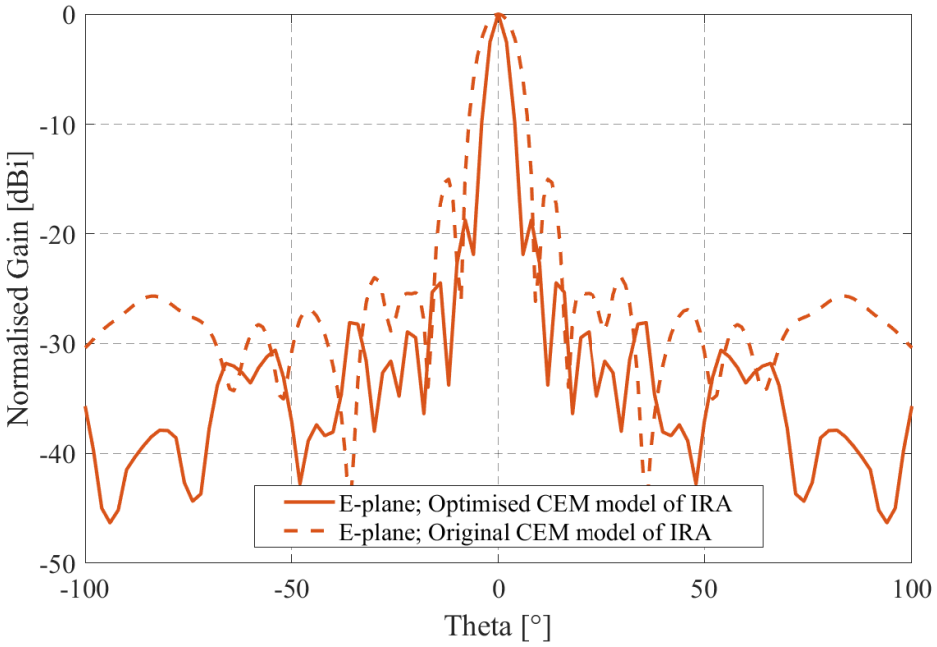

Figure 5.16: Comparison of the E-plane far-field pattern between the optimised CEM model of IRA and the original CEM model of IRA at 4 GHz.

5.1.5 Gain and Efficiency of the Optimised IRA

Simulation result showing the realised gain of the optimised IRA is presented in Figure 5.18. This is compared with the simulated gain of the original IRA. The plots indicate that the optimised IRA has a higher gain in most part of the frequency band with the difference

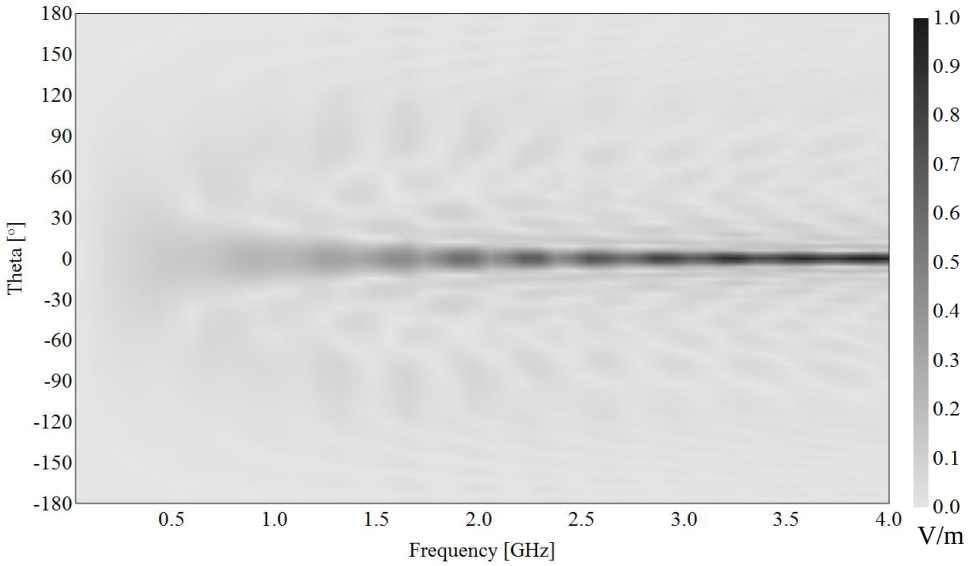

Figure 5.17: Simulated far-field pattern of the co-polar component, E_θ, for the optimised IRA.

being within 5 dB. And with the realised gain data, it is possible to do comparison of the radiation performance of the optimised IRA and the original IRA when the aperture efficiency, η, is determined from the realised gain as follows [45]:

$$\eta = \left(\frac{\lambda}{\pi D}\right)^2 G_r \text{ x } 100 \tag{5.3}$$

where λ is the wavelength, G_r is the realised gain and D is the diameter of the reflector.

The calculated aperture efficiencies of the optimised and the original IRA are plotted in Figure 5.19. It can be seen that in most part of the frequency spectrum, the original IRA has low variation of the efficiency with the average value being 22.28%. The trifilar coupled-line fed IRA has an improved aperture efficiency of 34.25% with high variation in most of the frequency band. A typical IRA with feed-arm angle $\varphi = 45°$ has aperture efficiency in the order of 25% [34]. An optimum efficiency of 35% with $\varphi = 70°$ has been determined in [43], and comparison for different feed configurations give calculated efficiencies between 20%–45% [45]. It is demonstrated in [83] that for antennas with focusing optics and self-reciprocal feed structures, $\eta \leq 50\%$. This is due to the fact that almost 50% of the power propagate in the fields that miss the focusing optics [84]. The other reason that lead to low aperture efficiencies in the IRAs is the field non-uniformity with regards to feeding the IRA. This explains why the aperture efficiencies of both the optimised and the original IRA are below 50%. In the following section the fabricated IRA is analysed.

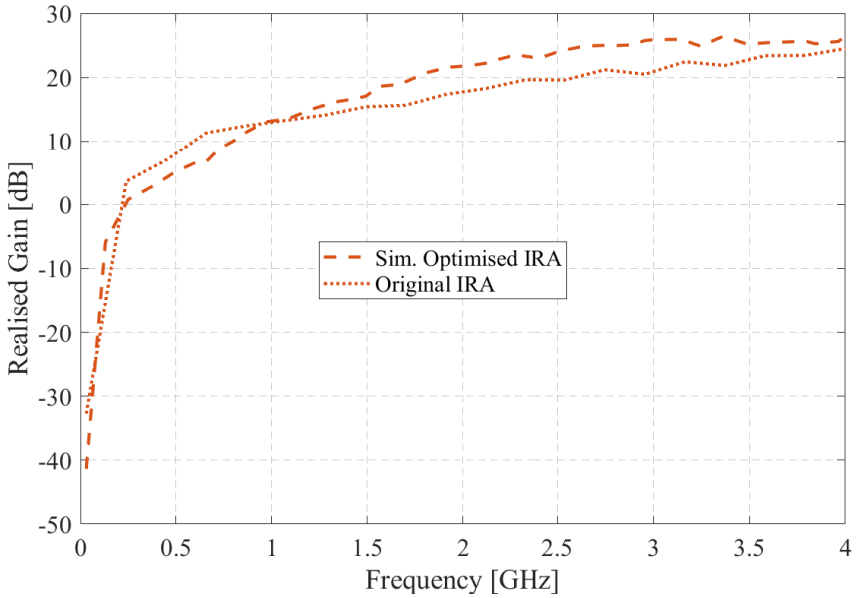

Figure 5.18: Comparison of the simulated realised gain of the optimised IRA and the original IRA.

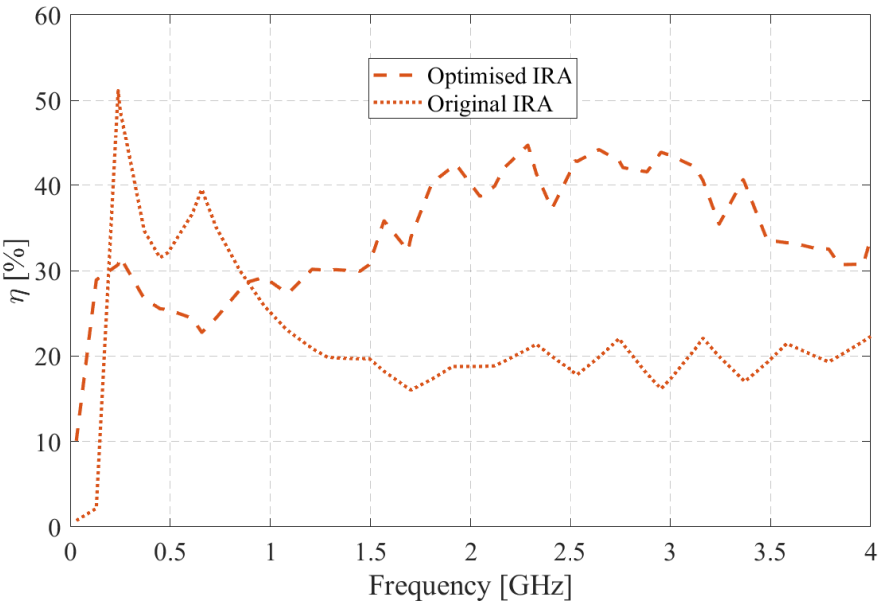

Figure 5.19: Comparison of the radiation efficiency calculated from the realised gain of the optimised IRA and the original IRA.

5.2 Characterization of the Fabricated Optimised IRA

In this section a fabricated IRA based on the optimised CEM model in Figure 5.11 is assembled and characterised in an anechoic chamber. Figure 5.20 shows some of the new components for the optimised IRA. The tapered conical plates are made from double-sided PCB board with copper conductors. The plates have smoothly filed edges to eliminate the

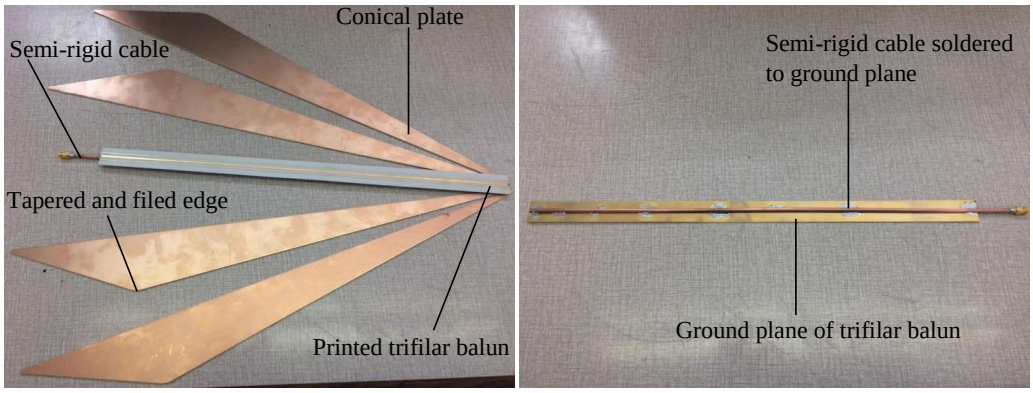

Figure 5.20: Components of the optimised IRA: the trifilar coupled-line balun and the tapered conical plates.

risk of accidental cuts when handling the antenna as well as charge build up associated with sharp edges. It has been observed that tapering of the plates is more effective in reducing the stored energy at the arm-reflector junction than the lumped termination loads [45].

The trifilar coupled-line balun has a fixed semi-rigid cable (electrically connected) at the bottom of the ground plane that is used to excite the primary conductor of the balun (Figure 5.20). The primary conductor is terminated to ground with two parallel 100 ohm RCS0402100RFKED (appendix B) surface mount (SMD) resistors. These are anti-surge and high-power rating (0.2 W) resistors suitable for the balun due to high tolerance to surge and the small size requirement. They are connected in parallel to obtain a 50-ohm impedance required to match the primary line (refer to chapter 4, section 4.4).

The reflector for the original IRA is reused because it is readily available, but due to movement and handling of the original IRA during measurement or storage, it is no longer perfectly symmetrical (or parabolic). However, the shape of the reflector has been adjusted to improve its symmetry. The construction of the optimised IRA is carried out at our engineering workshop and the completed IRA is shown in Figure 5.21.

A zoomed view of equally spaced five termination loads on a single side of the conical plate is shown in the inset photo of Figure 5.21. Each conical plate is terminated with ten 2 k-ohm ERA-8AEB202V (appendix B) SMD resistors in parallel, resulting into a 200-ohm matched circuit at the plate-reflector junction. The fabricated optimised IRA is then measured and the results compared to simulation results from the exact optimised CEM model described in sub-section 5.1.4.

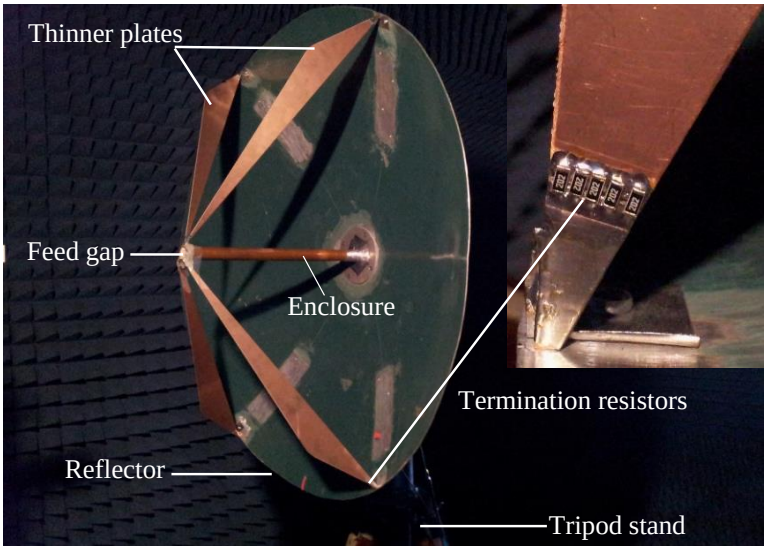

Figure 5.21: A photo of the fabricated optimised IRA; inset photo shows the termination resistors.

5.2.1 Verification by Measurement

The reflection co-efficient, S_{11}, for the optimised IRA is measured using a two-port modern PNA-X vector network analyser (VNA) with its port 1 connected to the IRA through a phase stable cable. The set-up for this measurement can be seen in Figure 5.22.

An electronic calibration is performed on port 1 of the VNA such that the calibration plane is set at the connection point (behind the reflector) between the phase stable cable and the trifilar balun. The frequency range used is 20 MHz to 12 GHz with 600 discrete points. However, owing to the fact that the CEM model is limited to the highest frequency of 4 GHz, the comparison between the measured and simulated S_{11} data is within 20 MHz to 4 GHz (Figure 5.23).

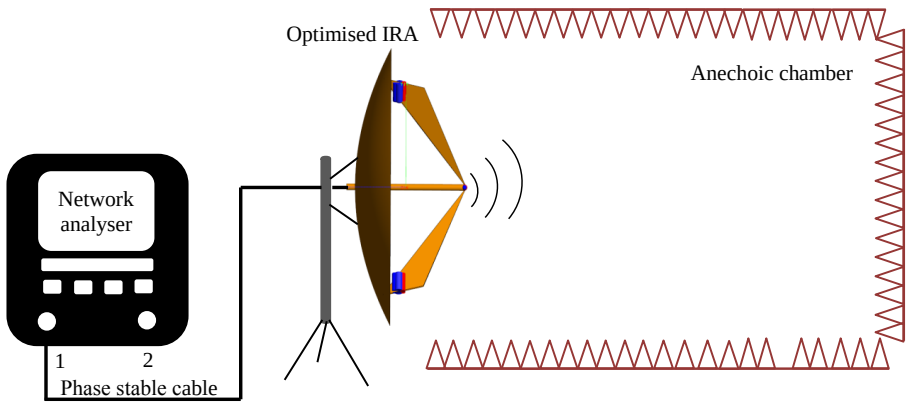

Figure 5.22: Diagram of the measurement set-up for S_{11}-parameter in the anechoic chamber.

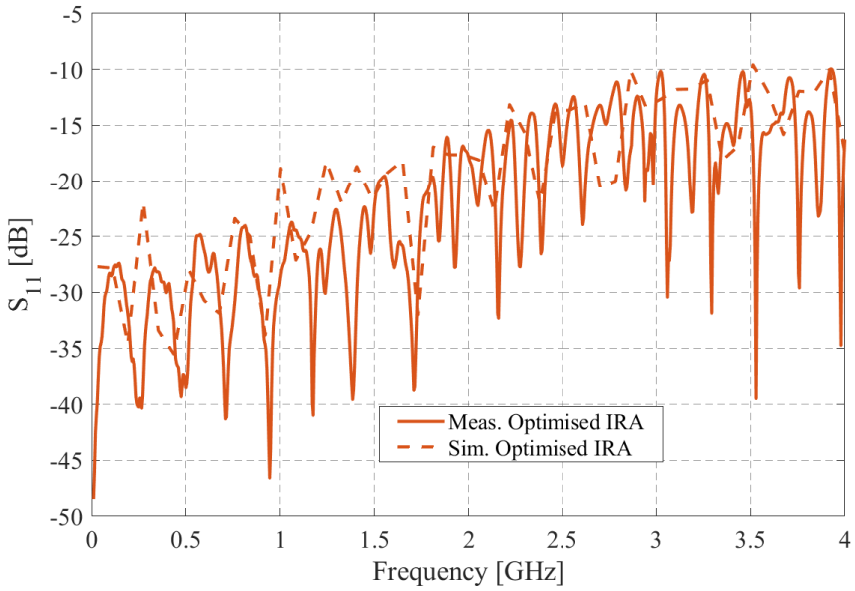

Figure 5.23: S_{11} comparison between measurement and simulation for the optimised IRA.

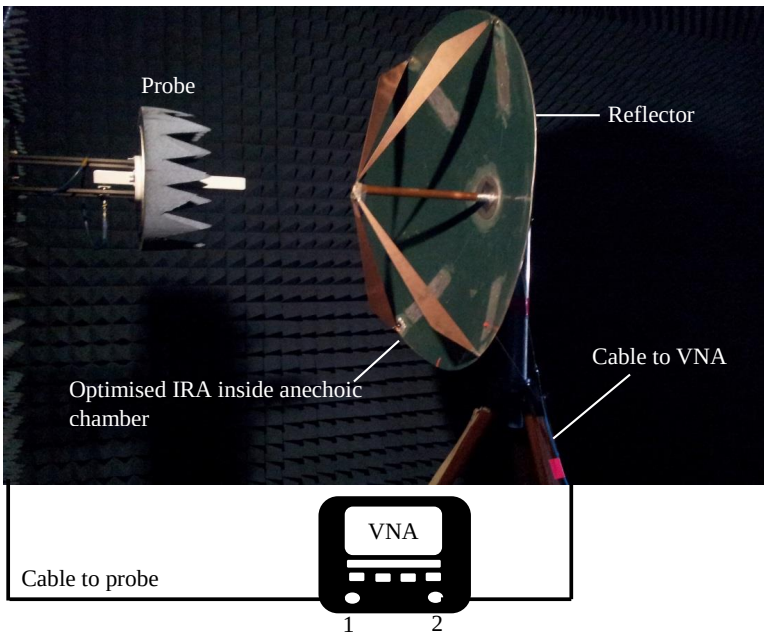

Figure 5.24: Optimised IRA inside the anechoic chamber for planar near-field measurements.

From Figure 5.23, the plots show that the simulated and measured S_{11} have close agreement over the frequency band except at few resonance points on the lower frequency end (below 1.5 GHz). Figures 5.23 and A.5 in appendix A.1 demonstrate that the optimised IRA has low reflection coefficient over a wider frequency band, up to 9 GHz. Thus, the calculated B_{frac} is 1.9911 which qualifies the IRA as a hyper-band (HB) antenna (see chapter 2, section 2.2). The HB low S_{11} is attributed to the characteristics of the trifilar coupled-line balun.

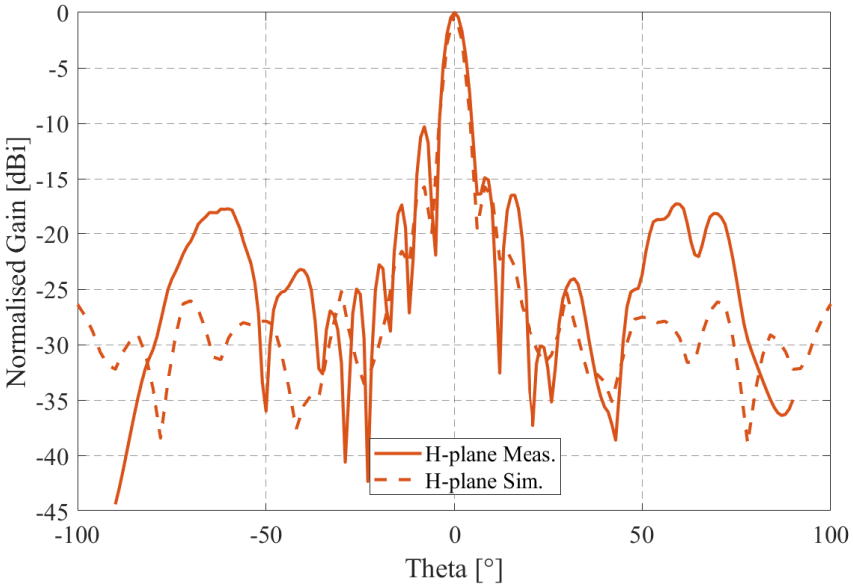

Figure 5.25: Comparison of the measured H-plane far-field pattern with the simulated one for the optimised IRA at 4 GHz.

For planar near-field scanning of the IRA, the set-up in Figure 5.24 is used. The frequency range of operation for the probe is 4 GHz to 6 GHz. The distance between the phase centre of IRA and that of the probe is 3λ, where λ is calculated using the relationship $c = \lambda f$, with c being the speed of light and f the lower frequency limit of the probe (4 GHz). We are interested in the far-field radiation characteristic of the IRA at 4 GHz for the same reason that the upper limit frequency in the simulation is 4 GHz. The planar near-field measured data is automatically converted to the far-field data using an installed scanner-software and compared with far-field simulation data.

Figure 5.25 gives the far-zone radiation pattern in the H-plane of the optimised FEKO model and the exact fabricated IRA. The results show that the measured and simulated BW have close agreement. However, the first side lobes of the measured IRA are relatively imbalanced. This is expected due to the fact that the reflector is not perfectly parabolic, leading to slight misalignment of the plates at the feed of the antenna. Furthermore, any small misalignment of the probe or the IRA can result in such variations of the side lobes because the structural response of IRA can be sensitive at high frequency (in this case 4 GHz). The difference in the high side lobe level at around $\pm 60^{\circ}$ can be attributed to the limitation of the linear scanner which accurately scans within $\pm 30^{\circ}$ or $\pm 45^{\circ}$, hence anything beyond this range would be considered measurement artefact. Table 5.3 shows a summary of the performance comparison between the original and the optimised IRA with respect to the SLL, S_{11}, BW and the back lobe. The results in the table indicate an enhanced performance of the optimised IRA over the original IRA.

Table 5.3: Summary of the performance of the original and optimised IRA with respect to the SLL (at 4 GHz), S_{11}, BW and the back lobe.

	SLL/H-plane	SLL/E-plane	S_{11}(Meas.)	BW(H/E-plane)	Back-lobe
Original IRA	-10.31 dB	-14.95 dB	> -10 dB	Unequal	Large
Optimised IRA	-16.11 dB	-18.75 dB	< -10 dB	Equal	Small

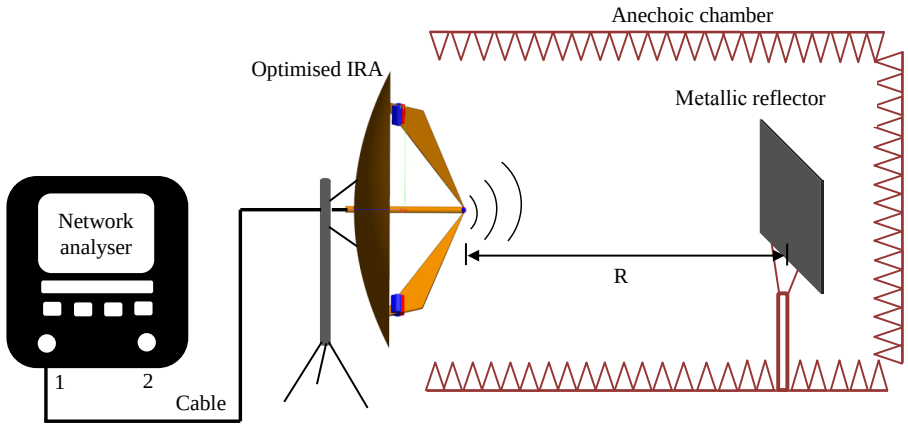

Figure 5.26: Illustration of the measurement set-up used for obtaining the data for gain calculation of the fabricated IRA.

5.2.2 Gain Measurement

The gain measurement set-up is shown in Figure 5.26 where the IRA is connected to a single port of the VNA and is placed with its front side facing the anechoic chamber. This approach is used because the far-field distance of the IRA is greater than the dimensional length of the chamber ($\approx$ 5 m), and this limits the effectiveness of the conventional methods used for far-field gain measurements. The anechoic chamber is designed to operate effectively from 2 GHz to 18 GHz. With the diameter of the dish being 850 mm, a typical far-field distance equation ($R_{far} \geq 2D^2/\lambda$) at 2 GHz gives approximately 10 m, where D is the diameter of the dish and λ is the wavelength. However, using the IRA's far-field equation ($R_{far} \geq D^2/2ct_{mr}$) gives a value of 12 m, where c is the speed of light and t_{mr} is the maximum rate of rise, usually in the order of hundreds of picoseconds [28]. The approximated far-field using both equations is greater than 5 m, therefore, we use a measurement procedure which relies on the physics of the radar range equation (RRE) to determine the measured gain of the IRA.

For a bi-static radar system (refer to Figure A.6, appendix A.1) the RRE is given as [17, 73]:

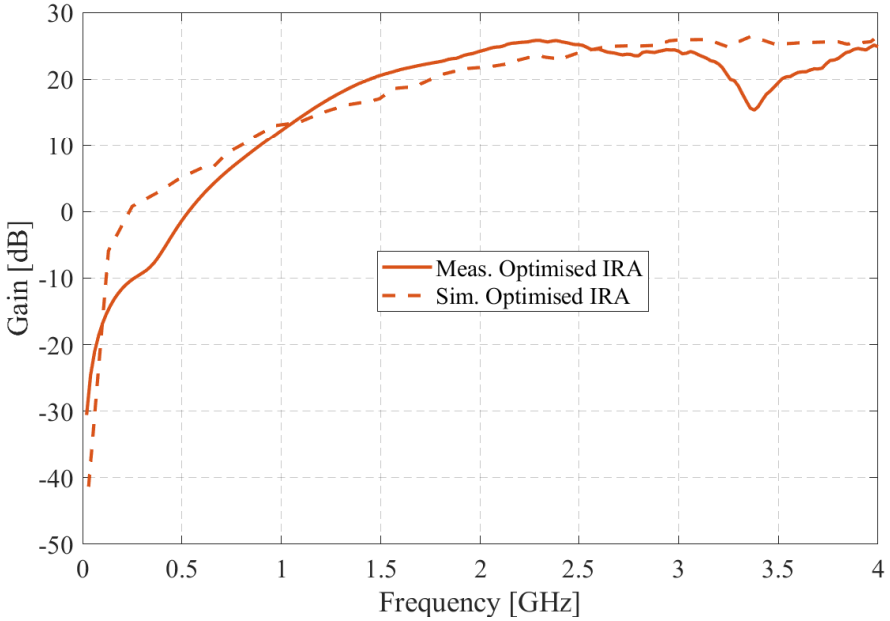

Figure 5.27: Gain comparison between the measured optimised IRA and the simulated optimised IRA.

$$\frac{P_r}{P_t} = (1 - |\Gamma_r|^2)(1 - |\Gamma_t|^2)\sigma \left(\frac{\lambda}{4\pi R_1 R_2}\right)^2 \frac{G_r(\theta_r, \phi_r)G_t(\theta_r, \phi_r)}{4\pi} |P_w.P_t|^2 \tag{5.4}$$

where P_t is the power transmitted, P_r is the power received, G_t is the gain of the transmitting antenna, G_r is the gain of the receiving antenna, λ is the wavelength of the signal, Γ_r is the reflection coefficient of the receiving antenna, Γ_t is the reflection coefficient of the transmitting antenna, R_1 and R_2 represent the observation distances from the target. The parameter σ is known as the radar cross-section (RCS) and is expressed as $4\pi a^2/\lambda^2$, where a is the area of the target. However, the set-up in Figure 5.26 represents a mono-static radar system where the transmitting antenna (IRA) is also the receiving antenna. Consequently, the polarization factor, $|P_w.P_t|^2$, becomes one (dot product, $cos(0) = 1$) and equation (5.4) can be simplified and rearranged to form the following equation:

$$G = \sqrt{\frac{|S'_{11}|^2(4\pi)(16\pi^2 R^4)}{\sigma\lambda^2(1 - |S_{11}|^2)^2}} \tag{5.5}$$

where S_{11} refers to the measured reflection coefficient of the IRA radiating into free-space, in the absence of the target (metallic plate) whereas $S'_{11} = \frac{P_r}{P_t}$ is the reflection coefficient measured in the presence of the plate as presented in Figure 5.26.

The general assumption of this approach is that the distance from the observation point

to the antenna can be within the near-field of the antenna and this sometimes lead to ambiguities in measurements [85]. As a result this method has its own uncertainties which are yet to be fully explored and developed for accurate measurement. For this particular set-up a metallic plate of size 622 mm by 622 mm is used and the distance, R, from the feed point to the plate is 2.3 m (Figure 5.26). The size of the reflector is chosen such that its largest dimension is closer to the D of the IRA, with the assumption that it backscatters most of the fields at the feed point of the IRA. The distance R is any value where the reflected signal can be visible or identified. With all the parameters known, equation (5.5) is used to determine the measured gain of the IRA. Figure 5.27 presents the measured gain plot of the fabricated IRA compared to the simulated optimised IRA. The difference between the measured and the simulated gain is within 2.5 dB from 660 MHz to 3.08 GHz. However, at 280 MHz and 3.4 GHz there is a big difference of 10 dB between the measured and simulated gain and this can be attributed to measurement uncertainties of the approach. Although, the method has been used for gain characterization of the IRA it has some inadequacies which require further investigation but that is not the focus of this dissertation.

5.3 Summary

A computational model of the IRA without the trifilar balun has been successfully studied using the MoM code in FEKO. It is used as a test model and the results indicate that it has better gain, reduced back lobe and S_{11} response than the original CEM model of the IRA. However, the feeding structure in the test model is not practical with a fabricated IRA hence the trifilar balun is introduced into the model for further investigation.

A CEM model of the IRA with the trifilar coupled-line balun is implemented in FEKO and optimised using the Genetic Algorithm method. The optimised CEM model has uniform aperture fields, reduced back lobe and SLL levels and uniform surface current distribution on the reflector. Furthermore, the results in subsection 5.1.5 show that in most of the frequency spectrum, the gain of the optimised IRA is higher compared to the gain of the original IRA; the difference being within 5 dB. It has been established that the optimised IRA has better radiation performance with the average aperture efficiency being 34.25% while that of the original IRA is 22.28%. The improved performance of the optimised IRA over the original model of the IRA is on account of the balanced feed which is a characteristic of the trifilar coupled-line balun.

The fabricated optimised IRA is assembled and measured in the anechoic chamber and the measured data used together with the results from simulation to successfully validate

the optimised IRA. From the analysis the simulated and measured BW and S_{11} of the optimised IRA indicate close agreement including the gain comparison which is within 2.5 dB from 660 MHz to 3.08 GHz.

—No research will answer all queries that the future may raise. It is wiser to praise the work for what it has accomplished and then to formulate the problems still to be solved —

—Theobald Smith —

CHAPTER 6

Conclusions and Recommendations

The MeerKAT and other SKA science facilities are based on regions which are some of the most remote locations on the planet, as part of the plan to manage RFI. But the terrestrial environment constitutes some form of EM waves whether from man-made or natural sources. Thus, the policy of constant monitoring of RFI can greatly contribute to the success of the SKA-SA project. The IRA as an HB directional antenna has the characteristics for the intended application of an RFI TD metrology system with the SKA RTA. With proper configuration of the feeding structure, the time domain reflections of the IRA which can cause ghost images in the measured data are minimised. Hence the reason for optimisation of the IRA with special attention given to the balanced feed structure; the trifilar coupled-line balun. Chapter 1 highlighted the scope of the research project and the methodology employed in attaining the research objectives. In chapter 2 the literature linked the EM theory with antenna engineering and focussed on the UWB technology with respect to the IRA. The four main components of the IRA were discussed and it was established that the key challenge is to match the IRA over the expected large-band-ratio. In chapter 3 various feeding configurations of the original IRAs were discussed and this was important in identifying the requirements for the trifilar balun. The details of the optimised trifilar balun and the fabricated IRA were described in chapters 4 and 5, respectively.

6.1 Research Summary

The original 150 ohm conical plate-fed reflector IRA design at our engineering department was characterised in TD and FD to determine areas that required optimisation. The launcher plates and the splitter-balun were the main areas that required optimisation but the splitter was more critical. It was shown that for a fixed impedance ($Z_{line} = 150\ \Omega$) and plate size ($b_1/a = 0.72$) the IRA had a better S_{11} when φ_0 was set as 45° than $\varphi_0 = 60°$. The original IRA had $\varphi_0 = 60°$ and since b_1/a is inversely proportional to φ_0 implied that thicker plates would have been used instead, and it was numerically predicted as $b_1/a = 0.59$ in [43]. However, thicker plates contribute to aperture blockage. Therefore, to design thinner plates for the IRA, Z_{line} had to be increased to match the impedance of the conical plates to the Z_{line}. But the requirement for high impedance RF coaxial cables to match the Z_{line} was a limiting factor. Also, the cable-fed IRAs are susceptible to common-mode currents on the feed-lines and this caused severe mismatch for the original IRA. Although the splitter was suitably matched it caused serious unbalance for the IRA as well, as it did not minimise the effect of the unwanted currents. Thus, the cable-fed IRAs have for a long time depended on the expensive RF chokes to isolate the unwanted currents. And the question arose whether it was possible to design a balun that had a dual function; both as an HB balun and as an extended transmission line to eliminate the use of RF cables and chokes.

The coupled transmission line concept was studied to design a novel HB trifilar coupled-line balun for the IRA. The initial prototype was a uniformly coupled symmetric microstrip line structure which was successfully verified through computational modelling (CST and AWR) and measurement. The analysis of the prototype provided two important results. First, it worked as envisioned by providing the TD FEC output signals with opposite amplitudes for the excitation of the IRA's negative and positive plates. Secondly, the prototype was perfectly matched across the entire frequency band. However, the existence of the NEXT and the imbalanced FEC pulses were major concerns, hence further investigation was carried out through to the final design of the trifilar balun.

We found out that the pre-pulse (NEXT) distorted the shape and balance of the FEC pulses. But the study showed that the non-uniformly coupled symmetric configuration was better suited for achieving more balance for the FEC signals and minimising the undesired NEXT. And the magnitude of the FEC output pulses improved with the increase in the coupling length, l_{sub}, and shorter rise time. The coupled-line structure provided the flexibility to design the required impedances for two secondary traces, 100 ohm/ per trace (effectively 200 ohm input impedance), and the l_{sub} as 400 mm, hence the balun

was treated as a twin–100 Ω 'feed cable' of 400 mm length. In general, this replaces the expensive RF coaxial cables which are problematic with common-mode currents and also eliminates the use of costly chokes in the cable-fed IRAs. We were successful in designing and optimising the final CST model of the trifilar coupled-line balun as well as the exact fabricated version of the balun.

A new 200 ohm conical plate-fed reflector IRA was investigated in FEKO using the MoM code. The CST model of the trifilar balun was imported into FEKO and implemented as part of the structure of the CEM model of the IRA. The full wave simulation results of the optimised CEM model at different frequencies showed uniform current distribution on the reflector of the IRA. In comparison, the results for the original IRA model showed that there was more current density around the centre of the aperture and dominated along the x-axis, particularly at 4 GHz. In that regard, the E-plane and H-plane BWs of the optimised IRA had to be similar whereas the H-plane BW of the original model had to have a narrower BW than that of its E-plane. Further analysis indicated reduced back lobes and SLLs in the optimised IRA. At 4 GHz the SLL in the H-plane and E-plane were 5.8 dB and 3.8 dB, respectively, less than those of the original IRA model. The symmetric aperture obtained with the optimised IRA was attributed to the balanced feed structure where the trifilar balun was used as the main optimisation factor.

Following a successful optimisation and analysis of the FEKO model of the IRA, an exact physical IRA was fabricated and characterised in the anechoic chamber. The fabricated IRA was verified using the simulated S_{11} and the far-field radiation pattern. It was demonstrated that the optimised IRA had low S_{11} over a large-band-ratio – with computed B_{frac} of 1.9911 – which qualified the IRA as a hyper-band (HB) antenna. Also, it was shown that the simulated and measured BW have close agreement. However, the first side lobes of the fabricated IRA were relatively imbalanced and this was for the reason that the dish was not perfectly parabolic, causing slight misalignment of the launcher plates at the feed gap. Based on the four main requirements for the trifilar balun the following were achieved:

- Developed an HB trifilar coupled-line balun, with the HB ($B_{frac} = 1.9911$) low S_{11} of the optimised IRA linked to the HB nature of the trifilar balun.
- The reflector was uniformly illuminated through the trifilar balun structure, hence an optimised aperture with balanced currents, symmetric far-zone patterns (similar BW at H- and E-planes), minimised back lobes and SLLs as well as improved response of S_{11} of the IRA across the HB frequency.
- Benefited from the new and simple 'cable topology' implemented as part of the

trifilar balun and showed to be very cost effective, e.g., it obviated the need for expensive and high impedance RF coaxial feed cables including the dummy cables and high-quality chokes which are normally required to 'choke-off' the common-mode currents.

- Low reflections with the optimised IRA even at higher frequencies (up to 9 GHz) illustrated the better frequency properties of the Rogers RO4003C material (low loss at the upper frequency band).

The HB trifilar balun can be applied to any conical-plate fed aperture IRA and other HB antennas if optimal performance is required over HB frequency. It can be easily modified to have specific trace impedances, coupling lengths and configuration to suit specific requirements.

6.2 Recommendations

The IRA was optimised for the low-power EMC studies related to the SKA SA project and the microstrip coupled-line structure provided sufficient coupled output pulses to drive the IRA. For the HPEM applications such as in radar, and other UWB applications, a broadside-coupled stripline structure, though difficult to fabricate, is recommended for tighter coupling within the balun structure. Further refinement at the feed gap involving the transition from the balun to the conical plates can be an area of interest, to improve the response of the IRA at frequencies beyond 9 GHz. Though, the launcher plates were reduced in size (high characteristic impedance), tapered and optimised to minimise the aperture blockage, further optimisation is recommended by changing the shape of the plates or using other optimisation methods. With regards to the lumped loads the focus can be on the exact placement and distribution/concentration of the loads to investigate the time domain reflections of the loads (flatter response would be better). Research on the integration of the IRA with the SKA RTA for a complete TD metrology system is essential for rigorous testing of the IRA and as an RFI auto-monitoring tool on-site.

—The greatest accomplishment is not in never falling, but in rising again after you fall —

—Vince Lombardi —

References

[1] J. Jonas, "The South African Array with Composite Dishes and Wide–band Single Pixel Feeds." IEEE, Aug 2009.

[2] "The history of the SKA project," https://www.skatelescope.org/project/ history-of-the-skaproject.

[3] R. Ambrosini, "RFI Selection Criteria for Radio Telescopes." 17^{th} International Wroclaw Symposium and Exhibition on Electromagnetic Compatibility, 29 June – 1 July 2004.

[4] "Proposal to site the SKA – Analysis of the Radio Frequency Environment." National Research Foundation, March 2006.

[5] R. Oliva, E. Daganzo, Y. H. Kerr, S. Mecklenburg, S. Nieto, P. Richaume, and C. Gruhier, "SMOS Radio Frequency Interference Scenario: Status and Actions Taken to Improve the Environment in the 1400–1427–MHz passive band." Geoscience and Remote Sensing, IEEE Transactions, 2012.

[6] C. E. Baum, "Radiation of impulse-like transient fields," in *Sensor and Simulation Notes #321*, Nov. 1989.

[7] D. V. Giri and F. M. Tesche, "Classification of intentional electromagnetic environments (IEME)," *IEEE Transactions on Electromagnetic Compatibility*, vol. 46, no. 3, pp. 322–328, Aug 2004.

[8] C. A. Balanis, "Antenna theory: a review," *Proceedings of the IEEE*, vol. 80, no. 1, pp. 7–23, Jan 1992.

[9] C. E. Baum, "EMP Simulators for Various Types of Nuclear EMP Environments: An Interim Categorization," *IEEE Transactions on Electromagnetic Compatibility*, vol. EMC-20, no. 1, pp. 35–53, Feb 1978.

[10] W. R. Stone, *Review of ImpulseRadiating Antennas*. IEEE, 1999. [Online]. Available: https://ieeexplore.ieee.org/document/5264625

[11] L. H. Bowen and E. G. Farr, "A High-Voltage Cable-Fed Impulse Radiating Antenna," in *sensor and Simulation Notes #507*. Farr Research, Inc., Dec. 2005.

[12] I. Oppermann, M. Hämäläinen, and J. Iinatti, *UWB Theory and Applications*. John Wiley & Sons, Ltd, 2004.

[13] N. Matthysen, "Time Domain Metrology for MeerKAT Systems," Master's thesis, Stellenbosch Univ., 2014.

[14] R. A. Mack and J. Sevick, *Sevick's Transmission Line Transformers Theory and practice*, 5th ed. SciTech Publishing, 2014.

[15] D. J. Griffiths, *Introduction to Electrodynamics*, 3rd ed. Prentice Hall, 1999.

[16] P. S. Kildal, *Foundations of Antenna Engineering: A Unified Approach for Line-of-Sight and Multipath*. Kildal Antenn AB, 2015.

[17] C. A. Balanis, *Antenna theory, analysis and design*, 3rd ed. Wiley, 2005.

[18] X. Chen, P.-S. Kildal, and M. Gustafsson, "Characterization of implemented algorithm for MIMO spatial multiplexing in reverberation chamber," *IEEE Transactions on Antennas and Propagation*, vol. 61, no. 8, pp. 4400–4404, August 2013.

[19] D. M. Pozar, *Microwave Engineering*, 4th ed. John Wiley & Sons, Inc., 2012.

[20] H. G. Schantz, *The Art and Science of Ultrawideband Antennas*, 2nd ed. Artech House Inc., 2015.

[21] F. Sabath, E. L. Mokole, and S. N. Samaddar, "Definition and classification of ultra-wideband signals and devices," *URSI Radio Science Bulletin*, vol. 2005, no. 313, pp. 12–26, June 2005.

[22] "Blind men and an elephant." https://en.wikipedia.org/wiki/Blind_men_and_an_elephant.

[23] C. E. Baum, E. G. Farr, and D. V. Giri, "Review of impulse-radiating antennas," in *Review of Radio Science*. W. R. Stone, Ed. Oxford, U.K.: Oxford Univ. Press, 1999, pp. 403–439. [Online]. Available: http://ieeexplore.ieee.org/xpl/articleDetails.jsp?arnumber=5264625

[24] R. DuHamel, M. Armstrong, J. Campbell, W. Jones, and W. Pedler, "Frequency independent conical feeds for lens and reflectors," in *Antennas and Propagation Society International Symposium*, vol. 6, Sept 1968, pp. 414–418.

[25] C. E. Baum and E. G. Farr, "Impulse radiating antennas," in *Ultra-Wideband/Short-Pulse Electromagnetics*. H. L. Bertoni, L. Carin, and L. B. Felson, Eds. New York: Plenum, 1993, pp. 131–134.

[26] E. G. Farr, C. E. Baum, and C. J. Buchenauer, "Impulse radiating antennas, part II," in *Ultra Wideband/Short-Pulse Electromagnetics 2*. New York: Press, 1995, pp. 159–170.

[27] C. E. Baum, "Impulse radiating antennas, part III," in *Ultra Wideband/Short-Pulse Electromagnetics 3*. C. E. Baum, L. Carin, and A. P. Stone, Eds. New York: Plenum Press, 1997, pp. 43–56.

[28] D. V. Giri, *High Power Electromagnetic Radiators: Nonlethal Weapons and other Application*. Harvard University Press, 2004.

[29] L. Bowmen, E. Farr, G. Salo, J. Gwynne, C. Baum, W. Prather, and T. Tran, "Studies of an impulse radiating antenna and a pulse radiating antenna element for SAR and target identification applications," in *Sensor and Simulation Notes 442*, March 2000.

[30] D. V. Giri, H. Lackner, I. D. Smith, D. W. Morton, C. E. Baum, J. R. Marek, W. D. Prather, and D. W. Scholfield, "Design, fabrication, and testing of a paraboloidal reflector antenna and pulser system for impulse-like waveforms," *IEEE Transactions on Plasma Science*, vol. 25, no. 2, pp. 318–326, Apr 1997.

[31] C. E. Baum, "Aperture Efficiencies of IRAs," in *sensor and Simulation Notes #328*. C. E. Baum Ed. Albuquerque, NM: USAF Philips Lab., June 1991.

[32] D. V. Giri and F. M. Tesche, "Energy patterns of the prototype impulse-radiating antenna," in *2011 XXXth URSI General Assembly and Scientific Symposium*, Aug 2011, pp. 1–1.

[33] C. E. Baum, "The physical optics approximation and early time scattering," in *Interaction Notes #563*. C. E. Baum Ed. Albuquerque, NM: Air Force Research Lab., 2000.

[34] J. S. Tyo, M. Dogan, J. H. Boddeker, and C. J. Buchenauer, "Increasing the focused response of impulse radiating antennas through polarization control of aperture fields," *IEEE Transactions on Antennas and Propagation*, vol. 54, no. 2, pp. 586–594, Feb 2006.

[35] P. Wade, "Parabolic Dish Feeds-Performance Analysis," 1998. [Online]. Available: https://www.qsl.net/n1bwt/chap11.pdf

[36] E. G. Farr, "Analysis of the impulse radiating antenna," in *IEEE Antennas and Propagation Society International Symposium 1992 Digest*, June 1992, pp. 1232–1235 vol.3.

[37] J. Qiu, B. Sun, C. Zhang, and N. Wang, "Improved design of the reflector impulse radiating antenna (IRA)," in *2008 4th International Conference on Ultrawideband and Ultrashort Impulse Signals*, Sept 2008, pp. 63–65.

[38] D. V. Giri, "Radiation of impulse-like waveforms with illustrative applications," in *2004 Second International Workshop Ultrawideband and Ultrashort Impulse Signals (IEEE Cat. No.04EX925)*, Sept 2004, pp. 16–20.

[39] M. Valibeiglou and A. Khaleghi, "A reflector impulse radiating antenna (IRA) with a new feeding structure," in *The 8th European Conference on Antennas and Propagation (EuCAP 2014)*, April 2014, pp. 894–898.

[40] D. V. Giri, "Peak power gain in time domain of impulse radiating antennas (IRAs)," in *2011 International Conference on Electromagnetics in Advanced Applications*, Sept 2011, pp. 12–14.

[41] M. Manteghi and Y. Rahmat-Samii, "On the characterization of a reflector impulse radiating antenna (IRA): full-wave analysis and measured results," *IEEE Transactions on Antennas and Propagation*, vol. 54, no. 3, pp. 812–822, March 2006.

[42] E. G. Farr and C. E. Baum, "Prepulse associated with the TEM feed of an impulse radiating antenna," in *Sensor and Simulation Notes #337*. E. Baum, Ed. Albuquerque, NM: Phillips Laboratory, Mar 1992.

[43] J. S. Tyo, "Optimization of the TEM Feed Structure for Four-Arm Reflector Impulse Radiating Antennas," *IEEE Trans. Antennas Propag.*, vol. 49, no. 4, pp. 607–614, Apr. 2001.

[44] L. H. Bowen, E. G. Farr, C. E. Baum, T. C. Tran, and W. D. Prather, "Experimental results of optimizing the location of feed arms in a collapsible IRA and a solid IRA," in *Sensor and Simulation Note 450*, Nov 2000.

[45] M. Manteghi and Y. Rahmat-Samii, "Improved feeding structures to enhance the performance of the reflector impulse radiating antenna (IRA)," *IEEE Transactions on Antennas and Propagation*, vol. 54, no. 3, pp. 823–834, March 2006.

[46] M. Manteghi and Y. Rahmat-Samii, "A novel UWB feeding mechanism for the TEM horn antenna, reflector IRA, and the Vivaldi antenna," *IEEE Antennas and Propagation Magazine*, vol. 46, no. 5, pp. 81–87, Oct 2004.

[47] J. H. Craven, "A Novel Broad-Band Balun (Correspondence)," *IRE Transactions on Microwave Theory and Techniques*, vol. 8, no. 6, pp. 672–673, November 1960.

[48] G. Oltman, "The Compensated Balun," *IEEE Transactions on Microwave Theory and Techniques*, vol. 14, no. 3, pp. 112–119, Mar 1966.

[49] P. R. Foster and S. M. Tun, "A wideband balun from coaxial line to TEM line," in *Antennas and Propagation, 1995., Ninth International Conference on (Conf. Publ. No. 407)*, Apr 1995, pp. 286–290 vol.1.

[50] F. M. Tesche, D. V. Giri, and W. D. Prather, "Scattered EM Field Responses of Canonical Scatterers Illuminated by an Impulse-Radiating Antenna (IRA)," *IEEE Antennas and Propagation Magazine*, vol. 51, no. 3, pp. 53–69, June 2009.

[51] S. Xiao, S. Altunc, P. Kumar, C. E. Baum, and K. H. Schoenbach, "A Reflector Antenna for Focusing Subnanosecond Pulses in the Near Field," *IEEE Antennas and Wireless Propagation Letters*, vol. 9, pp. 12–15, 2010.

[52] J. McLean and R. Sutton, "Rigorous Analysis of an Impulse Radiating Antenna with a Non-ideal Feed Structure," in *Sensor and Simulation Notes, Note 530*. TDK R & D Corp., 2007.

[53] E. Bogatin, *Signal and Power Integrity – Simplified*, 2nd ed. Pearson Education, Inc., 2004.

[54] M. Bocher, "Introduction to the Theory of Fourier's Series," *Annals of Mathematics*, vol. 7, no. 3, 1906.

[55] W. Henry, "On a certain periodic function," *The cambridge and Dublin mathematical Journal*, vol. 3, 1848.

[56] G. J. Willard, "Fourier's series," *Nature*, vol. 59, no. 1539, April 1899.

[57] H. Edwin and R. E. Hewitt, "The Gibbs-Wilbraham phenomenon: An episode in fourier analysis," *Archive for History of Exact Sciences*, vol. 21, no. 2, 1979.

[58] H. Henning, *Sequence Theory*. New York: Academic Press, 1977.

[59] A. M. Nicolson, C. L. Bennett, D. Lamesdorf, and L. Susman, "Applications of Time-Domain Metrology to the Automation of Broad-Band Microwave Measurements,"

IEEE Transactions on Microwave Theory and Techniques, vol. 20, no. 1, pp. 3–9, Jan 1972.

[60] J. Badenhorst, "Metrology and Modelling of High Frequency Probes," Master's thesis, Stellenbosch Univ., 2008.

[61] D. J. Angelakos and T. E. Everhert, *Microwave Communications*. McGraw-Hill, New York, 1968.

[62] C. Wang and T. Keech, "Antenna Models for Electromagnetic Compatibility Analyses," U.S. department of commerce NTIA, Tech. Rep., Oct. 2012.

[63] C. E. Baum and H. N. Kritikos, *Electromagnetic Symmetry*. CRC Press, 1995.

[64] C. E. Baum, "Configurations of TEM Feed for an IRA," in *sensor and Simulation Notes #327*, 1991.

[65] ——, "A Conical-Transmission-Line Gap for a Cylindrical Loop," in *Sensor and Simulation Note 42*, 1967.

[66] E. G. Farr, "Optimizing the Feed Impedance of Impulse Radiating Antennas Part I: Reflector IRAs," in *Sensor and Simulation Notes # 354*, 1993.

[67] K. S. Dhiraj, D. C. Pande, and A. Bhattacharya, "A New Feed for Reflector Based 100 Ω Impulse Radiating Antenna," in *PIERS, KL, Malaysia*, 2012.

[68] F. Vega, F. Rachidi, N. Mora, N. Pena, and F. Roman, "Design, Realization, and Experimental Test of a Coaxial Exponential Transmission Line Adaptor for a Half-Impulse Radiating Antenna," *IEEE Transactions on Plasma Science*, vol. 41, no. 1, pp. 173–181, Jan 2013.

[69] B. C. Wadell, *Transmission Line Design Handbook*. Artech House Inc., 1991.

[70] M. W. Maxwell, *REFLECTIONS III Transmission Lines and Antennas*. CQ Communications, Inc., 2010.

[71] C. E. Baum, "A Transmission-Line Transformer for Matching the Switched Oscillator to a Higher-Impedance Resistive Load," in *Circuit and Electromagnetic System Design Notes, Note 46*. Air Force Research Lab., Aug. 2001.

[72] Z. Zhang and G. Boeck, "Ultra broadband planar transmission line transformers with ferrite based bandwidth extension," in *2016 46th European Microwave Conference (EuMC)*, Oct 2016, pp. 987–990.

[73] B. Guru and H. Hiziroğlu, *Electromagnetic Field Theory and Fundamentals*, 2nd ed. Cambridge University Press, 2004.

[74] C. E. Baum, "Coupled Transmission Lines as a Time-Domain Directional Coupler," in *Sensor and Simulation Notes, Note 451*. Air Force Research Lab., Oct. 2000.

[75] R. Mongia, I. J. Bahl, and P. Bhartia, *RF and Microwave Coupled-Line Circuits*. Artech House, Inc., 1999.

[76] R. P. Clayton, *TRANSMISSION LINES IN DIGITAL SYSTEMS FOR EMC PRACTITIONERS*. John Wiley & Sons, Inc., 2012.

[77] D. A. Hill, K. H. Cavcey, and R. T. Johnk, "Crosstalk between microstrip transmission lines," *IEEE Transactions on Electromagnetic Compatibility*, vol. 36, no. 4, pp. 314–321, Nov 1994.

[78] M. B. Bazdar, A. R. Djordjevic, R. F. Harrington, and T. K. Sarkar, "Evaluation of quasi-static matrix parameters for multiconductor transmission lines using Galerkin's method," *IEEE Transactions on Microwave Theory and Techniques*, vol. 42, no. 7, pp. 1223–1228, July 1994.

[79] E. Bogatin, "Design rules for microstrip capacitance," *IEEE Transactions on Components, Hybrids, and Manufacturing Technology*, vol. 11, no. 3, pp. 253–259, Sep. 1988.

[80] M. Abramowitz and I. A. Stegun, *Handbook of Mathematical Functions with Formulas, Graphs, and Mathematical Tables*. Dover Publications, Inc., 1970.

[81] "South African CHPC." https://www.chpc.ac.za/index.php/resources/lengau-cluster.

[82] A. Hyperworks, *FEKO Comprehensive Electromagnetic Solutions: User Manual 2017.2*, Altair Engineering, Inc., 2017.

[83] C. J. Buchenauer, J. S. Tyo, and J. S. H. Schoenberg, "Aperture efficiencies of impulse radiating antennas," in *Ultra- Wideband Short-Pulse Electromagnetics 4 (IEEE Cat. No.98EX112)*, June 1998, pp. 91–108.

[84] E. G. Farr. and C. E. Baum, "Radiation from Self-reciprocal aaperture," in *Electromagnetic Symmetry*. C. E. Baum and H. N. Kritikos, Eds. New York: Plenum, 1995.

[85] B. Scheers, M. Acheroy, and A. Vander Vorst, "Time-domain simulation and characterisation of tem horns using a normalised impulse response," *IEE Proceedings - Microwaves, Antennas and Propagation*, vol. 147, no. 6, pp. 463–468, Dec 2000.

APPENDIX A

Tables and Graphs

A.1 Optimisation Methods and Graphs

Table A.1 presents an overview of optimisation methods in FEKO which include: (a) Simplex (Nelder-Mead) – a gradient-based or 'hill-climbing' technique, (b) Particle swarm optimisation (PSO) – a swarm-based global search technique, (c) Genetic algorithm (GA) – a robust and evolutionary global search technique, (d) Adaptive response surface method (ARSM) – creates internal response surface which updates with increase in sample points and (e) Global response surface method (GRSM) – creates internal response surface which updates with increase in sample points and continues to test different areas of the design space [82]. There are two more optimisation methods also available in FEKO: the automatic method which automatically chose the optimiser and the Grid search which searches over a predefined grid of parameter sets [82].

Figures A.1–A.4 show optimisation graphs for the CEM model of IRA in Figure 5.11. The reflection coefficient of the optimised IRA is presented in Figure A.5 and it shows the hyper-band nature of the trifilar balun.

Table A.1: An overview of optimisation methods in FEKO [82].

Method	Description	No. of variables	Convergence	Accuracy	Farming
Simplex	local search, optimum relies strongly on starting point	low	fast	locally high, globally low	initial re-creating simplex
PSO	population-based stochastic global search	high	slow	medium/ high	yes
GA	robust, stochastic global search	high	slow/ medium	medium/ high	yes
ASRM	response surface based approach	medium	fast	low/ medium	no
GSRM	response surface based approach, good balance btw local and global	high	medium	high	yes

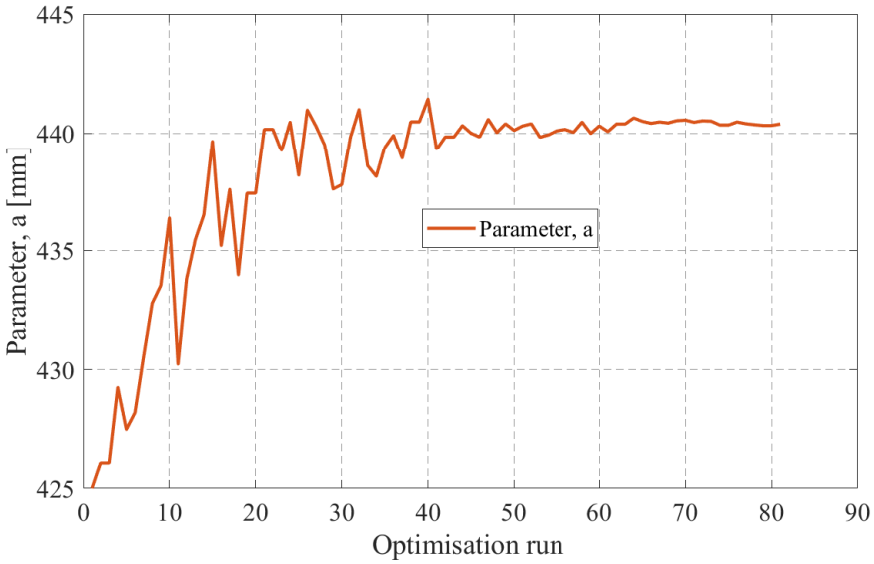

Figure A.1: Optimisation of the parameter, a, whose optimised value is attained between the optimisation numbers 63–81, where $a = 440.6$. mm.

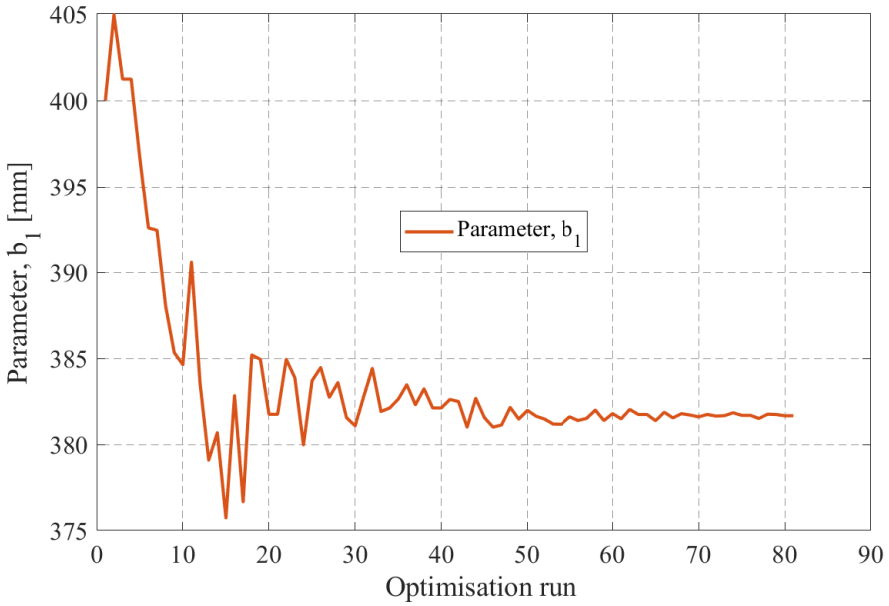

Figure A.2: Optimisation of the parameter, b_1, whose optimised value is attained between the optimisation numbers 57–81, where $b_1 = 381.8.$ mm.

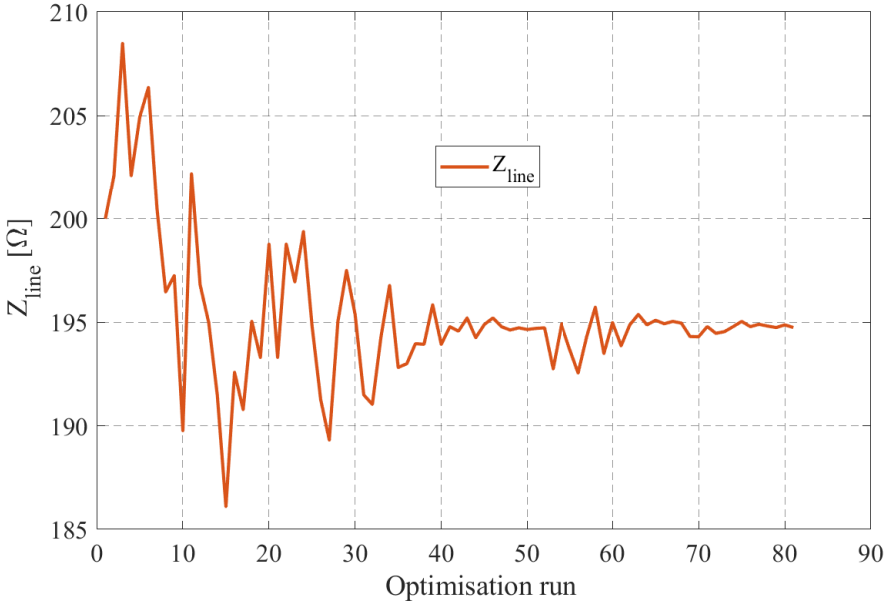

Figure A.3: Optimisation of the parameter, Z_{line}, whose optimised value is attained between the optimisation numbers 63–81, where $Z_{line} = 195\ \Omega$.

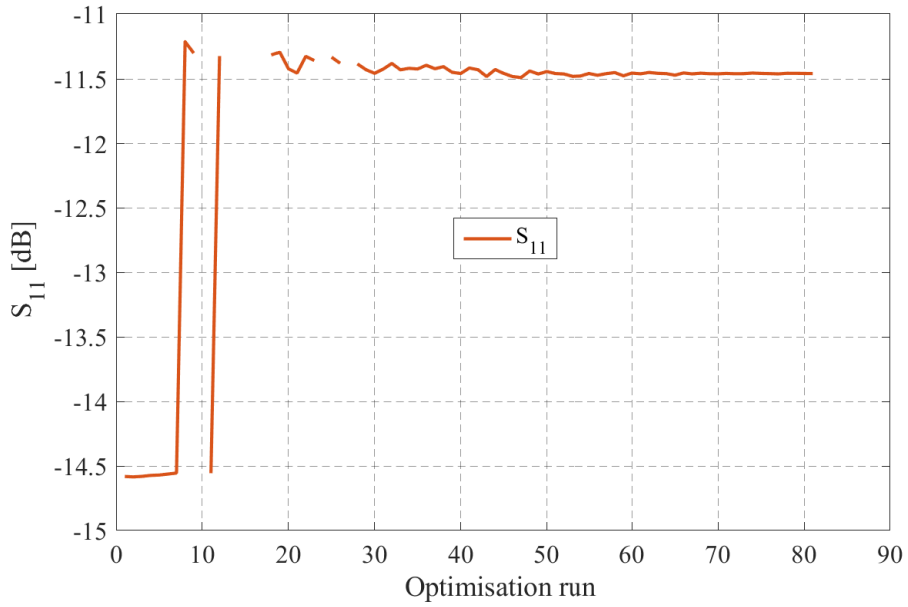

Figure A.4: Optimisation of the parameter, S_{11}, whose optimised value is attained between the optimisation numbers 47–81, where S_{11} = -11.46 dB.

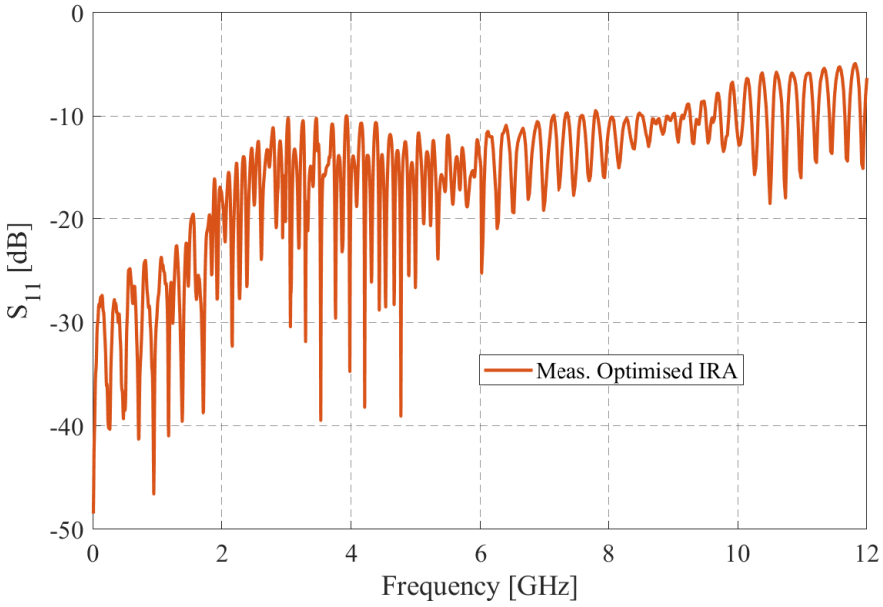

Figure A.5: Measured reflection coefficient of the optimised IRA.

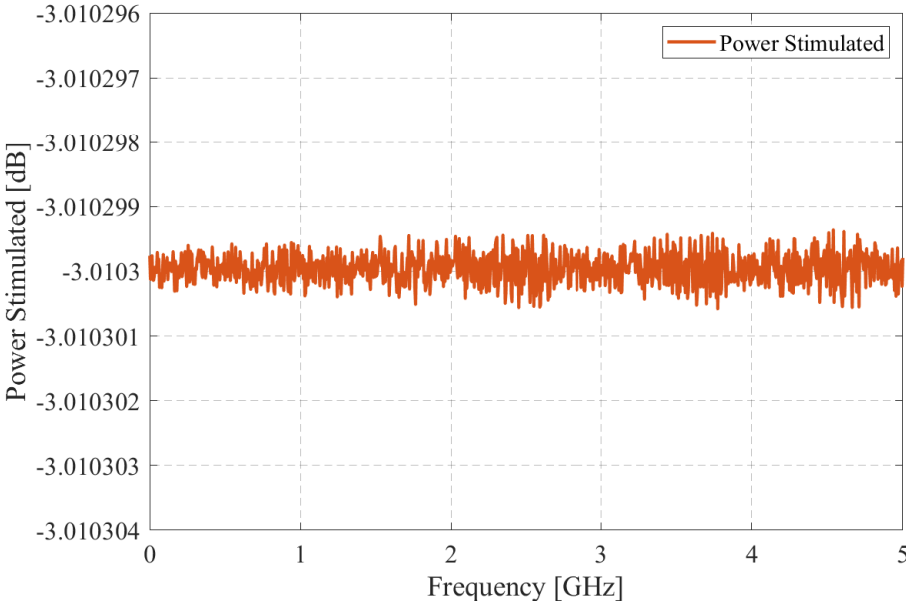

Figure A.6: The default value of the stimulated power used in the CST trifilar balun.

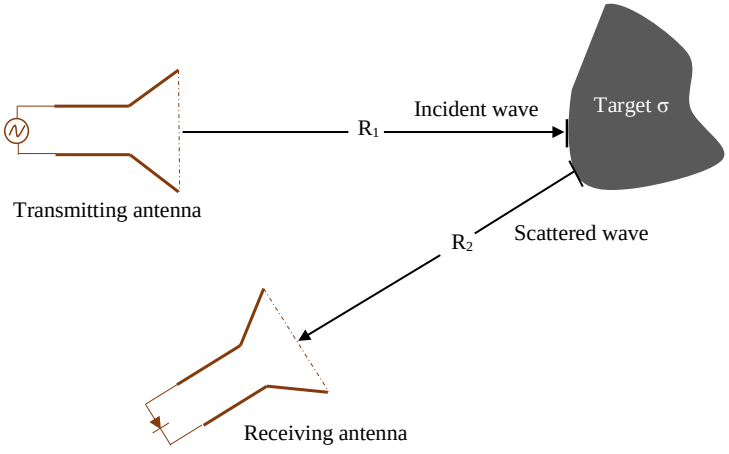

Figure A.7: Illustration of the bi-static radar system.

APPENDIX B

Specification Sheets for SMD Resistors and LMR Cable

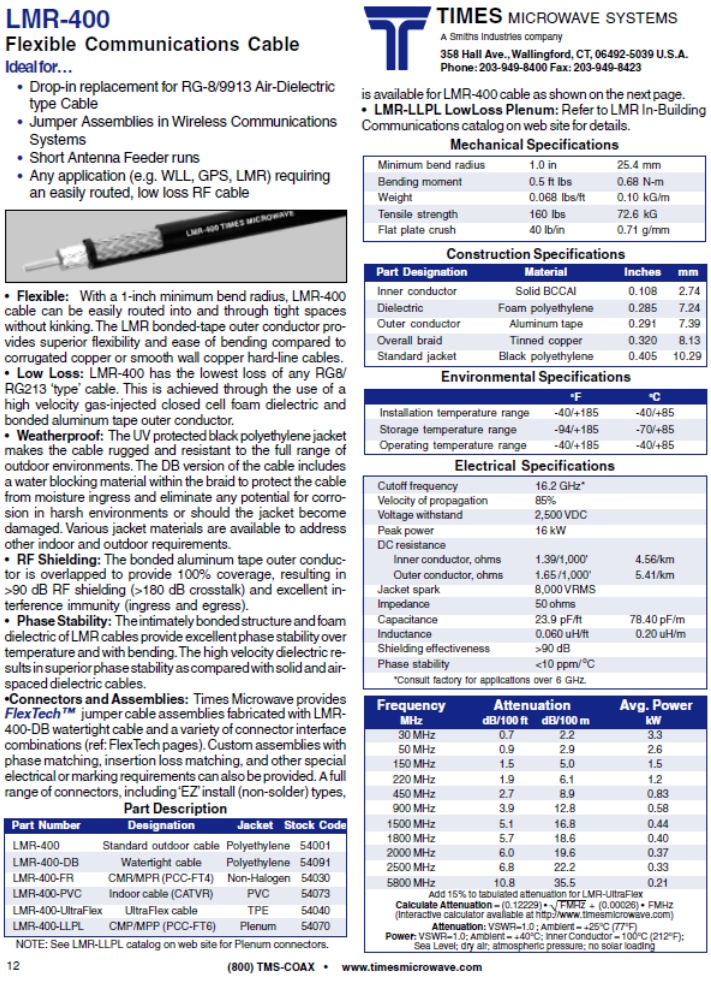

LMR-400
Flexible Communications Cable
Ideal for...

- Drop-in replacement for RG-8/9913 Air-Dielectric type Cable
- Jumper Assemblies in Wireless Communications Systems
- Short Antenna Feeder runs
- Any application (e.g. WLL, GPS, LMR) requiring an easily routed, low loss RF cable

• **Flexible:** With a 1-inch minimum bend radius, LMR-400 cable can be easily routed into and through tight spaces without kinking. The LMR bonded-tape outer conductor provides superior flexibility and ease of bending compared to corrugated copper or smooth wall copper hard-line cables.
• **Low Loss:** LMR-400 has the lowest loss of any RG8/RG213 'type' cable. This is achieved through the use of a high velocity gas-injected closed cell foam dielectric and bonded aluminum tape outer conductor.
• **Weatherproof:** The UV protected black polyethylene jacket makes the cable rugged and resistant to the full range of outdoor environments. The DB version of the cable includes a water blocking material within the braid to protect the cable from moisture ingress and eliminate any potential for corrosion in harsh environments or should the jacket become damaged. Various jacket materials are available to address other indoor and outdoor requirements.
• **RF Shielding:** The bonded aluminum tape outer conductor is overlapped to provide 100% coverage, resulting in >90 dB RF shielding (>180 dB crosstalk) and excellent interference immunity (ingress and egress).
• **Phase Stability:** The intimately bonded structure and foam dielectric of LMR cables provide excellent phase stability over temperature and with bending. The high velocity dielectric results in superior phase stability as compared with solid and air-spaced dielectric cables.
•**Connectors and Assemblies:** Times Microwave provides *FlexTech™* jumper cable assemblies fabricated with LMR-400-DB watertight cable and a variety of connector interface combinations (ref: FlexTech pages). Custom assemblies with phase matching, insertion loss matching, and other special electrical or marking requirements can also be provided. A full range of connectors, including 'EZ' install (non-solder) types,

Part Description

Part Number	Designation	Jacket	Stock Code
LMR-400	Standard outdoor cable	Polyethylene	54001
LMR-400-DB	Watertight cable	Polyethylene	54091
LMR-400-FR	CMR/MPR (PCC-FT4)	Non-Halogen	54030
LMR-400-PVC	Indoor cable (CATVR)	PVC	54073
LMR-400-UltraFlex	UltraFlex cable	TPE	54040
LMR-400-LLPL	CMP/MPP (PCC-FT6)	Plenum	54070

NOTE: See LMR-LLPL catalog on web site for Plenum connectors.

TIMES MICROWAVE SYSTEMS
A Smiths Industries company
358 Hall Ave., Wallingford, CT, 06492-5039 U.S.A.
Phone: 203-949-8400 Fax: 203-949-8423

is available for LMR-400 cable as shown on the next page.
• **LMR-LLPL LowLoss Plenum:** Refer to LMR In-Building Communications catalog on web site for details.

Mechanical Specifications

Minimum bend radius	1.0 in	25.4 mm
Bending moment	0.5 ft lbs	0.68 N-m
Weight	0.068 lbs/ft	0.10 kG/m
Tensile strength	160 lbs	72.6 kG
Flat plate crush	40 lb/in	0.71 g/mm

Construction Specifications

Part Designation	Material	Inches	mm
Inner conductor	Solid BCCAl	0.108	2.74
Dielectric	Foam polyethylene	0.285	7.24
Outer conductor	Aluminum tape	0.291	7.39
Overall braid	Tinned copper	0.320	8.13
Standard jacket	Black polyethylene	0.405	10.29

Environmental Specifications

	°F	°C
Installation temperature range	-40/+185	-40/+85
Storage temperature range	-94/+185	-70/+85
Operating temperature range	-40/+185	-40/+85

Electrical Specifications

Cutoff frequency	16.2 GHz*	
Velocity of propagation	85%	
Voltage withstand	2,500 VDC	
Peak power	16 kW	
DC resistance		
Inner conductor, ohms	1.39/1,000'	4.56/km
Outer conductor, ohms	1.65 /1,000'	5.41/km
Jacket spark	8,000 VRMS	
Impedance	50 ohms	
Capacitance	23.9 pF/ft	78.40 pF/m
Inductance	0.060 uH/ft	0.20 uH/m
Shielding effectiveness	>90 dB	
Phase stability	<10 ppm/°C	

*Consult factory for applications over 6 GHz.

Frequency MHz	Attenuation dB/100 ft	Attenuation dB/100 m	Avg. Power kW
30 MHz	0.7	2.2	3.3
50 MHz	0.9	2.9	2.6
150 MHz	1.5	5.0	1.5
220 MHz	1.9	6.1	1.2
450 MHz	2.7	8.9	0.83
900 MHz	3.9	12.8	0.58
1500 MHz	5.1	16.8	0.44
1800 MHz	5.7	18.6	0.40
2000 MHz	6.0	19.6	0.37
2500 MHz	6.8	22.2	0.33
5800 MHz	10.8	35.5	0.21

Add 15% to tabulated attenuation for LMR-UltraFlex
Calculate Attenuation = (0.12229) • $\sqrt{FMHz}$ + (0.00026) • FMHz (interactive calculator available at http://www.timesmicrowave.com)
Attenuation: VSWR=1.0; Ambient = +25°C (77°F)
Power: VSWR=1.0; Ambient = +40°C; Inner Conductor = 100°C (212°F); Sea Level; dry air; atmospheric pressure; no solar loading

12 (800) TMS-COAX • www.timesmicrowave.com

Figure B.1: Specification sheet for LMR–400 cable.

VISHAY
www.vishay.com

RCS e3
Vishay

Anti-Surge, High Power Thick Film Chip Resistors

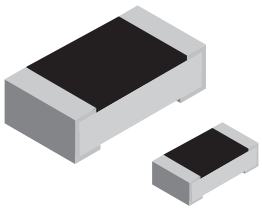

The anti-surge thick film chip resistor series combines a significantly higher power rating and pulse load performance as compared to standard chip resistors.

FEATURES

- Excellent surge pulse capability
- Superior ESD surge characteristics
- High power rating
- AEC-Q200 qualified
- Material categorization: for definitions of compliance please see www.vishay.com/doc?99912

RoHS COMPLIANT
HALOGEN FREE

APPLICATIONS

- Automotive
- Industrial
- Telecommunications
- Medical

TECHNICAL SPECIFICATIONS				
DESCRIPTION	**RCS0402 e3**	**RCS0603 e3**	**RCS0805 e3**	**RCS1206 e3**
Imperial size	0402	0603	0805	1206
Metric size code	RR1005M	RR1608M	RR2012M	RR3126M
Resistance range	1 Ω to 10 MΩ; jumper (0 Ω)			
Resistance tolerance	± 5 %; ± 1 %; ± 0.5 %			
Temperature coefficient	± 200 ppm/K; ± 100 ppm/K			
Rated dissipation, P_{70} (1)	0.2 W	0.25 W	0.4 W	0.5 W
Operating voltage, $U_{max.}$ AC_{RMS}/DC	50 V	75 V	150 V	200 V
Permissible film temperature, $\vartheta_{F\ max.}$ (1)	155 °C			
Operating temperature range	-55 °C to +155 °C			
Max. resistance change at P_{70} for resistance range, $\lvert\Delta R/R\rvert$ after:				
1000 h	≤ 1.0 %			
8000 h	≤ 2.0 %			
Permissible voltage against ambient (insulation):				
1 min, U_{ins}	75 V	100 V	200 V	300 V

Note
(1) Please refer to APPLICATION INFORMATION below.

APPLICATION INFORMATION

When the resistor dissipates power, a temperature rise above the ambient temperature occurs, dependent on the thermal resistance of the assembled resistor together with the printed circuit board. The rated dissipation applies only if the permitted film temperature is not exceeded.

These resistors do not feature a limited lifetime when operated within the permissible limits. However, resistance value drift increasing over operating time may result in exceeding a limit acceptable to the specific application, thereby establishing a functional lifetime.

Figure B.2: Specification sheet for 100 ohm RCS0402100RFKED surface mount (SMD) resistor.

Panasonic **Metal Film (Thin Film) Chip Resistors, High Reliability Type**

Metal Film (Thin Film) Chip Resistors, High Reliability Type

Type: **ERA 1A, 2A, 3A, 6A, 8A**

Features

- High reliability ····· Stable at high temperature and humidity (85 °C 85 %RH rated load, Category temperature range : –55 °C to +155 °C)
- High accuracy ····· Small resistance tolerance and Temperature Coefficient of Resistance
- High performance ····· Low current noise, excellent linearity
- Reference Standard ····· IEC 60115-8, JIS C 5201-8, EIAJ RC-2133B
- AEC-Q200 qualified
- RoHS compliant

■ **As for Packaging Methods, Land Pattern, Soldering Conditions and Safety Precautions,** Please see Data Files

Explanation of Part Numbers

- E24 Series

1	2	3	4	5	6	7	8	9	10	11
E	R	A	3	A	E	B	1	0	2	V

Product Code

Metal Film Chip Resistors

Size, Power Rating

Code	Inch	Power Rating
1A	0201	0.05 W
2A	0402	0.063 W
3A	0603	0.1 W
6A	0805	0.125 W
8A	1206	0.25 W

Temperature Coefficient

Code	T.C.R.
R	±10×10^{-6}/°C
P	±15×10^{-6}/°C
E	±25×10^{-6}/°C
H	±50×10^{-6}/°C
K	±100×10^{-6}/°C

Resistance Tolerance

Code	Tolerance
W	±0.05 %
B	±0.1 %
C	±0.25 %
D	±0.5 %

Packaging Methods

Code	Packaging	Part No.
C	Pressed Carrier Taping 2 mm pitch, 15000 pcs.	ERA1A
X	Punched Carrier Taping 2 mm pitch, 10000 pcs.	ERA2A
V	Punched CarrierTaping 4 mm pitch, 5000 pcs.	ERA3A ERA6A ERA8A

Resistance Value

Consist of three figures for E24 series resistance value. The first two digits are significant figures of resistance and the third one denotes number of zeros following.
(example) 102 : 1k Ω

- E96 Series and other Resistance values

1	2	3	4	5	6	7	8	9	10	11	12
E	R	A	3	A	E	B	1	0	5	1	V

Product Code

Metal Film Chip Resistors

Size, Power Rating

Code	Inch	Power Rating
1A	0201	0.05 W
2A	0402	0.063 W
3A	0603	0.1 W
6A	0805	0.125 W
8A	1206	0.25 W

Temperature Coefficient

Code	T.C.R.
R	±10×10^{-6}/°C
P	±15×10^{-6}/°C
E	±25×10^{-6}/°C
H	±50×10^{-6}/°C
K	±100×10^{-6}/°C

Resistance Tolerance

Code	Tolerance
W	±0.05 %
B	±0.1 %
C	±0.25 %
D	±0.5 %

Packaging Methods

Code	Packaging	Part No.
C	Pressed Carrier Taping 2 mm pitch, 15000 pcs.	ERA1A
X	Punched Carrier Taping 2 mm pitch, 10000 pcs.	ERA2A
V	Punched CarrierTaping 4 mm pitch, 5000 pcs.	ERA3A ERA6A ERA8A

Resistance Value

Consist of four figures for E96 series resistance value. The first three digits are significant figures of resistance and the fourth one denotes number of zeros following.
(example) 1051 : 1.05k Ω

note : Duplicated resistance values as E24 series part numbers shall follow E24 part numbers. (apply three digit resistance value)

Design and specifications are each subject to change without notice. Ask factory for the current technical specifications before purchase and/or use.
Should a safety concern arise regarding this product, please be sure to contact us immediately.

10 Feb. 2016

Figure B.3: Specification sheet for 2 k-ohm ERA-8AEB202V surface mount (SMD) resistor.

ROGERS CORPORATION

Data Sheet

RO4000® Series
High Frequency Circuit Materials

RO4000® hydrocarbon ceramic laminates are designed to offer superior high frequency performance and low cost circuit fabrication. The result is a low loss material which can be fabricated using standard epoxy/glass (FR-4) processes offered at competitive prices.

The selection of laminates typically available to designers is significantly reduced once operational frequencies increase to 500 MHz and above. RO4000 material possesses the properties needed by designers of RF microwave circuits and matching networks and controlled impedance transmission lines. Low dielectric loss allows RO4000 series material to be used in many applications where higher operating frequencies limit the use of conventional circuit board laminates. The temperature coefficient of dielectric constant is among the lowest of any circuit board material (Chart 1), and the dielectric constant is stable over a broad frequency range (Chart 2). For reduced insertion loss, LoPro® foil is available (Chart 3). This makes it an ideal substrate for broadband applications.

RO4000 material's thermal coefficient of expansion (CTE) provides several key benefits to the circuit designer. The expansion coefficient of RO4000 material is similar to that of copper which allows the material to exhibit excellent dimensional stability, a property needed for mixed dielectric multi-layer boards constructions. The low Z-axis CTE of RO4000 laminates provides reliable plated through-hole quality, even in severe thermal shock applications. RO4000 series material has a Tg of >280ºC (536ºF) so its expansion characteristics remain stable over the entire range of circuit processing temperatures.

RO4000 series laminates can easily be fabricated into printed circuit boards using standard FR-4 circuit board processing techniques. Unlike PTFE based high performance materials, RO4000 series laminates do not require specialized via preparation processes such as sodium etch. This material is a rigid, thermoset laminate that is capable of being processed by automated handling systems and scrubbing equipment used for copper surface preparation.

RO4003C™ laminates are currently offered in various configurations utilizing both 1080 and 1674 glass fabric styles, with all configurations meeting the same laminate electrical performance specification. Specifically designed as a drop-in replacement for the RO4003C™ material, RO4350B™ laminates utilize RoHS compliant flame-retardant technology for applications requiring UL 94V-0 certification. These materials conform to the requirements of IPC-4103, slash sheet /10 for RO4003C, see note #1 for RO4350B slash sheet determination.

Features and Benefits:

RO4000 materials are reinforced hydrocarbon/ceramic laminates - not PTFE
- Designed for performance sensitive, high volume applications

Low dielectric tolerance and low loss
- Excellent electrical performance
- Allows applications with higher operating frequencies
- Ideal for broadband applications

Stable electrical properties vs. frequency
- Controlled impedance transmission lines
- Repeatable design of filters

Low thermal coefficient of dielectric constant
- Excellent dimensional stability

Low Z-axis expansion
- Reliable plated through holes

Low in-plane expansion coefficient
- Remains stable over an entire range of circuit processing temperatures

Volume manufacturing process
- RO4000 laminates can be fabricated using standard glass epoxy processes
- Competitively priced

CAF resistant

Some Typical Applications:

- Cellular Base Station Antennas and Power Amplifiers
- RF Identification Tags
- Automotive Radar and Sensors
- LNB's for Direct Broadcast Satellites

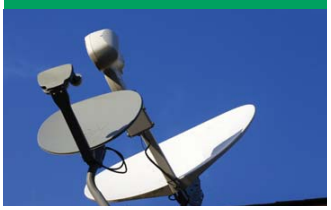

Advanced Connectivity Solutions
100 S. Roosevelt Avenue, Chandler, AZ 85226
Tel: 480-961-1382 Fax: 480-961-4533 www.rogerscorp.com

Figure B.4: Specification sheet for Rogers RO4003C PCB material.

APPENDIX C

Equations

The correction parameter equation is given as:

$$w^{'} = w + \Delta w^{'} \tag{C.1}$$

where $\Delta w^{'}$ and Δw are determined as follows.

$$\Delta w^{'} = \Delta w \left(\frac{1.0 + 1.0/\varepsilon_r}{2} \right) \tag{C.2}$$

$$\frac{\Delta w}{t} = \frac{1.0}{\pi} \ln \left[\frac{4.0}{\sqrt{\left(\left(\frac{t}{h}\right)^2 + \left(\frac{1/\pi}{w/t+1.1}\right)^2\right.}} \right] \tag{C.3}$$